Title
Evaluation of Spinal Reconstructive Surgeries Using Multi-Body System Dynamics

Author
Metzger, Melodie F.

Publication Date
2009

Peer reviewed|Thesis/dissertation

Evaluation of Spinal Reconstructive Surgeries
Using Multi-Body System Dynamics

by

Melodie F. Metzger

DISSERTATION

Submitted in partial satisfaction of the requirements for the degree of

DOCTOR OF PHILOSOPHY

in

Bioengineering

in the

GRADUATE DIVISION

of the

UNIVERSITY OF CALIFORNIA, SAN FRANCISCO

AND

UNIVERSITY OF CALIFORNIA, BERKELEY

[redacted]

Evaluation of Spinal Reconstructive Surgeries Using Multi-Body System Dynamics

The following Ph.D. Thesis is dedicated in loving memory to:

Carl Frederick Metzger, III

Acknowledgments

I would like to express my sincerest appreciation and gratitude to **Dr. Jeffrey C. Lotz**, my advisor, whose insight and experience in spine biomechanics and biologics is unmatched. I appreciate the opportunity to work in such a well respected laboratory, and can only hope to carry some of the outstanding qualities learned in this environment into subsequent stages of my career. I would also like to extend a huge thank you to **Dr. Oliver O'Reilly** whose dedication to students and enthusiasm for theoretical mechanics is honorable. His patience, tremendous knowledge of dynamics, and guidance were a true blessing throughout this process.

To my classmates, labmates, fellow BEASTs, and members of the Graduate Student Association at UCSF, thank you for your friendship and for helping me realize that I am not the only one to experience extreme frustration, emotional struggles, and bouts of insanity throughout the process of getting my graduate degree. In particular, I would like to thank the members of Jeff's Lab: **Azucena, Kevin, David Shultz, David Moody, Anne Kim, Zori, Aliza, Jeannie, Dezba, Jane, and Ellen** for five years of laughs and good times. A special thanks to **Azucena**, whose smile, spontaneous hug attacks, and contagious laugh I wish I could bottle up and take with me. To **Adila Papaya**, for her ability to make dynamics so much fun and for her humorous emails which have the potential to bring me to tears. To **Jenni Buckley** and **Carolyn Sparrey**, two amazing engineers and female mentors with endless advice, encouragement, and knowledge of spine biomechanics.

In addition, I am grateful to the **National Science Foundation** for awarding me a

Graduate Research Fellowship, an honor that I am very proud to have received and that provided financial support for the majority of my graduate education.

Last but not least, I would like to thank my family for their love and support. To my mother, **Bonnie Marie Mullee**, whose undying strength is an inspiration to all single mothers and women. Her ability to raise two children while juggling multiple jobs to provide the best possible upbringing for her children, I now recognize as an amazing personal sacrifice. Her support, unconditional love, and dedication to my education has made this dissertation possible. To my brother, **Jeffrey Allan Metzger**, whose intelligence goes beyond any degree, and whose devotion to family is something we should all aspire to. To **Stephanie Nicole Smith**, for bringing some of Ohio a little closer to home. While our blood may prove otherwise, you are a sister to me. And of course, to **Michael Thomas Telega**, my fianceé, for providing me the motivation to graduate and start a new chapter in my life.

Abstract

Evaluation of Spinal Reconstructive Surgeries Using Multi-Body System Dynamics

by

Melodie F. Metzger

Doctor of Philosophy in Bioengineering

University of California, San Francisco

Professor Jeffrey C. Lotz, Ph.D., Chair

Back pain is one of the most costly and pervasive medical problems in the United States. Unfortunately, despite investing billions of dollars over the past 40 years searching for a mechanical means of replacing degenerative intervertebral discs, no form of arthroplasty has proven to significantly improve patient care. This absence stems from complexities in intervertebral joint anatomy and motion. For instance, the disc itself is not a free-standing joint, but works in conjunction with the two adjacent facet joints. Current total disc replacements (TDRs) disregard this interaction, which possibly explains their suboptimal clinical performance but little research is available to support this theory. Therefore the aim of this dissertation is to first investigate the consequences of TDR on the adjacent facet joints. Afterwards, current measures of spinal motion are improved to quantifiably compare surgical instrumentation to the spine's natural motion patterns.

In vitro biomechanical experiments demonstrated that facet forces increase after

TDR implantation, most notably when the device is positioned anteriorly. During sagittal plane movement, TDRs displayed an increase in facet forces as specimens rotated into flexion, opposing the trend of the intact disc. These results indicate that over time TDRs may lead to increased facet arthritis and/or degeneration.

Two metrics capable of conveying the complex motion of the spine, the stiffness matrix and the helical axis of motion (HAM), were analyzed as possible tools for characterizing spinal motion before and after surgical alterations. By creating a method for determining the stiffness matrix which accommodates finite rotations, non-conservative forces, and energy loss, and by distilling this 36-component matrix into a single scalar, a measure of 6-D stiffness for comparative purposes was developed. This scalar proved useful in determining variations in stiffness post TDR implantation. This was followed by a thorough investigation of calculating the HAM which revealed that commonly used algorithms are too erroneous to detect changes after implanting a device. Thus, an alternate method was developed along with a set of best practices in minimizing HAM error. The combined result provides a general guideline for calculating sufficiently accurate HAM for characterizing the kinematics of motion preserving devices.

Professor Jeffrey C. Lotz, Ph.D.
Dissertation Committee Chair

Contents

List of Figures

List of Tables

Chapter 1

Introduction and Background

1.1 Introduction

Back pain is one of the most common medical problems in the United States. It affects 8 out of 10 people at some time in their lives and because it is a degenerative disease these numbers are likely to grow with our aging population. Medical advances for treating back pain have increased spending from $ 52.1 billion in 1997 to $ 85.9 billion in 2005; however there has been no significant improvement in patient outcomes over the past 10 years [85]. Patient demands for surgical intervention have resulted in spinal fusion becoming the standard response to intractable back pain in the United States. However, there is no clinical evidence showing spinal fusion is any more effective than physical therapy in managing pain.

Heightened awareness of the clinical drawbacks of fusion and the success of hip and knee replacements have fueled a new segment of the spine industry focused on motion preservation. Well over 100 start-ups have surfaced in the last couple of decades making new devices that address spinal joint reconstruction in the hopes of resolving back pain while maintaining segmental motion. These include artificial discs, disc nuclei, annulus repair, facet joint replacement, and dynamic stabilization of the spine. Paralleling this effort is a new biomaterials market aimed at improving fusion techniques with growth factors and other biologics.

Most of these products are in clinical-trials and the latest data is yet to suggest that any of these treatment modalities are a true success [44]. Currently, there are two FDA-approved lumbar total disc replacement devices and one posterior dynamic stabilization device approved for use in conjunction with fusion. All three have received mixed reviews clinically and their performance remains controversial. This leads to the conclusion that the result of all this effort is marginal improvements at best over fusion, the current long-standing surgical gold standard.

The absence of a successful new disc implant design stems from complexities in intervertebral joint anatomy and motion. Unlike the knee and hip, which have seen reliable and efficient replacements over the last 40 years, the intervertebral disc is not a simple cartilaginous interface. Instead it is a highly-organized heterogeneous structure with unique viscoelastic properties. In this regard, some disc prostheses have attempted to recreate the viscoelastic characteristics of the disc, while others focus on reproducing the motion of the disc mechanically, and there are even a few that aim to accomplish both of these principles. Unfortunately, of the hundreds of patents filed [137], none have surfaced as a close match to the innate disc.

In the wake of all this commotion a research industry focused on mechanical testing, wear analysis, and imaging of these devices has developed and is thriving on the continuous stream of prospective devices. It is hopeful that in this environment and with the right tools we will begin to decipher the natural motion of the spine and whether there is a prosthetic means to resolving back pain.

The following dissertation is focused on better understanding the complex motion of the spine and the implications of instrumentation. The first chapter discusses the anatomical and physiological complexities associated with low back pain, current surgical instrumentation to treat low back pain, established in vitro testing protocols, and the kinematic and kinetic evaluation of these devices. The second chapter is an in vitro investigation of an FDA-approved total disc replacement and its surgical placement within the disc space. This is followed by two chapters which apply advanced rigid body dynamics methodologies to investigate and improve upon tools that will allow for direct comparison before and after total disc replacement or any other spinal procedure. Lastly, a conclusion which suggests future research is presented.

1.2 Anatomy and Pathology of Lumbar Disc Degeneration

1.2.1 Functional Anatomy of the Lumbar Spine

Nature works in many ways to integrate form and function throughout the human body. The spine, with its complex structure whose functions include: protecting the spinal cord, providing muscle attachments, facilitating upright posture, and transferring loads from the head and trunk to the pelvis, perfectly illustrates this intricate relationship.

The lumbar region of the spine, synonymous with the low back, is comprised of the five distal-most vertebrae and the adjoining sacrum. This region interacts with many of the powerful muscles used to stabilize the trunk and generate forces for lifting tasks. Consequentially, it is designed to withstand and transfer greater loads than its superior neighbors, evident by its characteristic short, broad cross-sectional vertebral bodies and enhanced laminae. Each vertebral body is separated anteriorly by an intervertebral disc and posteriorly by cartilage-covered articular joints, called the zygapophyseal joints (or facet joints). Two adjacent vertebral bodies, in conjunction with their interconnecting disc, paired facets and surrounding ligaments define a functional spine unit (FSU, also called a 'motion segment', figure 1.1). Individual FSUs permits small motion about and along all three axes (6 degrees of freedom), which additively results in the trunk's extensive flexibility. The intervertebral disc and the facets are primarily responsible for the precisely proscribed motion of healthy lumbar FSUs, and therefore merit further investigation.

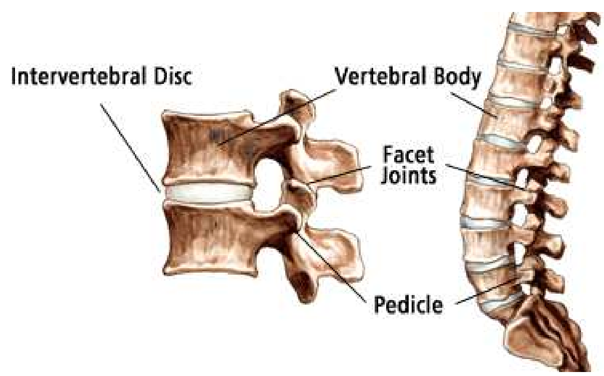

Figure 1.1: Sagittal view of a lumbar functional spine unit, on the left, and the lower portion (T10–S1) of the spine on the right.

The intervertebral disc is a multifaceted structure consisting of three distinct elements: the annulus fibrosus, the nucleus pulposus, and the cartilaginous endplates. The annulus fibrosus makes up the outermost portion of the disc, and consists of concentric rings of type-I collagen with alternating fiber orientation at $\pm 30°$–$35°$ to the endplate which provides resistance to bending and torsional loads. Moving interiorly, the nucleus pulposus is housed within and connected to the annulus fibrous. Made mostly of water (70–90%), type II collagen, and proteoglycan, this gel-like structure is intrinsically pressurized by the annulus and the tensile forces created by the surrounding ligamentous flava and longitudinal ligaments. The nucleus' hydrostatic state creates a load-bearing structure that distributes and stores loads throughout the disc [97]. The last components of the disc are the superior and inferior cartilagenous endplates which form a structural boundary between the disc and the vertebral core, allowing nutrients and water to transfer into the avascular disc space. In the lumbar spine healthy discs range from 10–12 mm in height and are the largest in the spine.

Figure 1.2: Cross-section of a porcine intervertebral disc showing the concentric rings of annulus fibrosus surrounding the gelatinous nucleus pulposus.

Assisting the disc from the posterior portion of the FSU are the paired left and right facets. These synovial joints are surrounded by a fibrous capsule and are comprised of the medially-facing superior articular process of the inferior vertebrae and the matching articular surface from the vertebral level above. Facet orientation varies along the length of the spine. In the lumbar region, the facets are approximately perpendicular to the transverse plane and have an increasing inclination in the sagittal plane from T1 to S1 (figure 1.3). Unlike the thoracic and cervical facets, the facets of the lumbar spine are significantly curved, with the anterior surface concave and the posterior surface convex. Biomechanically, these features allow the facets to work synergistically with the intervertebral disc to both guide motion and help transmit load across the FSU. In particular, it has been demonstrated that the facets play an important role in protecting the spine from over-extending, excessive-rotation, and large anteriorly-directed shears forces [1, 2, 36, 82, 147].

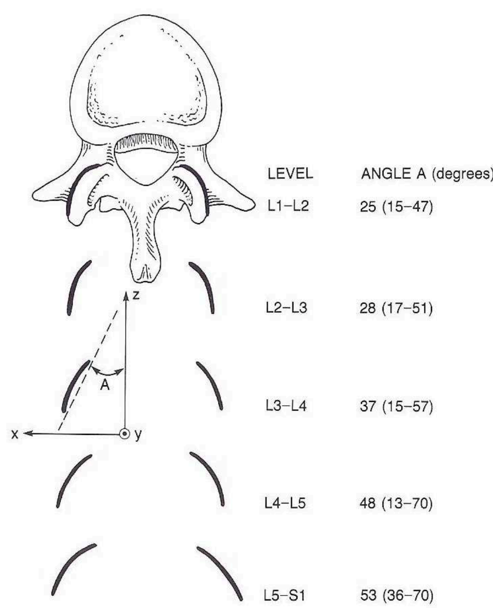

Figure 1.3: The shape and inclination of the lumbar facets with respect to the sagittal plane depicted in the transverse plane. (Picture adapted from White and Panjabi [144])

1.2.2 Progression of Degenerative Disc Disease

A healthy disc is analogous to an inflated tire with the annulus fibrosus resisting tensile hoop stresses similar to that of the tire walls, and the nucleus pulposus acting as the internal pressurized fluid. As we age the nucleus pulposus loses water, from about 80% at age 18 to 65 % at age 77, as well as proteoglycan content making the annulus and the nucleus less distinguishable [84, 88]. As a result, there is a reduction of intradiscal pressure and disc height, changing the load distribution to resemble something closer to a deflated tire. This forces the annulus to undergo transition from a tension-bearing structure to a compressive-bearing structure. Since the annulus is not designed to withstand compressive forces, tears and radial fissures develop and there is a decrease in axial stiffness of the spine [72, 93]. Laxity within the annulus also reduces bending and torsional stiffness, which may result in overloading of the facets [94]. Other structural consequences include radial bulge of the annulus, endplate defects, herniation of the nucleus, and posterior protrusion of the disc into the spinal canal. As degeneration continues further, the FSU eventually stiffens due to load-mediated remodeling and mineralization of the annulus fibrosus and the peripheral vertebral body [40, 88].

As the largest avascular organ in the body, the intervertebral disc has a limited nutrition supply delivered from the surrounding vertebral bodies through the cyclic loading and unloading of the pressurized disc. Degenerative biomechanical changes interrupt this flow and hence create a nearly irreversible degenerative cascade. While the exact mechanisms are unclear, these structural and biological changes are painful and can occur relatively early in life, especially if accelerated through a traumatic event. To alleviate pain conservative therapy is recommended, but if this fails, surgery is often the next step.

1.3 Current State of Surgical Treatment

Our fascination with the spine and the mystery of back pain has a long history tracing back to some of the most illustrious names in medicine, including Hippocrates, Galen, Paul of Aegina, and Ambroise Par [95]. Early non-surgical forms of treatment were initially focused on managing spinal disorders and deformities with gruesome looking external traction devices. Surgical treatment as we know it today did not emerge until 1829 when Alban Smith performed the first laminectomy on a patient suffering from paraparesis after falling off his horse [127]. His success in restoring sensation to the lower limbs moved others to follow his lead. This, paralleled with medical advances in the form of anesthesia [11] and radiography [116], helped propel spinal surgery into its own specialty by the turn of the twentieth century. Since then spinal surgery has grown to include a large variety of new approaches and techniques dividing spinal surgeons further into specializations such as spinal deformity, cervical, lumbar, and minimally invasive techniques, just to name a few.

Although we have come a long way in terms of surgical treatment over the past 200 years, clinical studies indicate that we have not yet overcome many of the obstacles presented by the spine's complex geometry and disease progression. In a 2009 review of surgical treatment for low back pain, fusion (the current gold-standard of treatment) was found to be no more effective than intensive rehabilitation, and its hopeful successor, the artificial disc, was shown to be only 'as effective' as fusion for non-radicular low back pain [20]. At first glance this seems discouraging, but optimism can be found as new technology continues to develop and we gain more insight into the intricacies of the spine. Below is a brief overview of current surgical techniques for low back pain starting with fusion, followed by a discussion on arthroplasty, and concluding with mention of a few devices that have not yet been FDA-approved.

1.3.1 Fusion

Since the procedure was first introduced by Albee [4] and Hibbs [62] in 1911 for the treatment of Pott's disease, spinal fusion (also known as arthrodesis) has become one of the most common surgical procedures in the spine. While there have been many improvements since its inception, the goal remains the same: to reduce or eliminate pain by diminishing motion between one or more spine segments. To accomplish this, bone graft is place between the vertebral bodies to provide stability and induce osteogenesis helping the bones heal together or 'fuse'. The bone graft used is typically in the form of autografts taken from the iliac crest or other areas where excess bone can be extracted of the patient, although in the past 20 years the use of allografts (organ donor bone from bone banks), biologics (e.g., demineralized bone matrix (DBM), autologous growth factor (AGF), and bone morphogenic protein (BMP)), internal fixation devices (e.g., screws), and graph carriers such as cages have been implemented to increase the rate of fusion. Similarly, techniques and surgical approaches have grown to include a wide-range of options. Initially the posterior approach was popular following the Hibb's technique of forming a continuous ridge across the spinous process. As the procedure grew to include treatment for low back pain, disc excision was added and the "combined approach" was implemented in 1947 [56] and became the popular technique for the next several decades. Today interbody fusion encompasses several different approaches (posterior, anterior, lateral, or a combination of) and in some cases is possible through minimally invasive techniques. Evolving with the procedure itself are the indications for which spinal fusion is performed. The most common being degenerative disc disease topping the list at an estimated $60 - 65\%$ of lumbar fusions, others include: spondylolisthesis, spinal stenosis, and spondylosis [78].

From its inception lumbar interbody fusion slowly gained international popularity until 1978 when Frymoyer et al. published a 10-year follow up investigating decompression with and without fusion that revealed relatively unsatisfactory results in both groups [45]. This produced a lull for several years that did not turn around until the advent of fusion instrumentation and advancements in other medical field such as magnetic resonance imaging and CT scanning. These developments brought fusion back into full swing, and by 1991 there were $32,701$ lumbar fusion operations in the U.S. Over the next ten years fusion became known as 'the gold-standard of treatment for back pain' with $122,316$ degenerative lumbar fusions in 2001 representing a 220% increase.

Interestingly, the slope of lumbar fusion rates after 1996 exceed those of knee and hip arthroplasty, two relatively successful procedures, despite being regarded as a controversial operation [20,32]. This counterintuitive point is most likely explained by the prevalence of back pain and the ambiguity surrounding its treatment. Evidence to this effect can be found in data on geographic variations in medical procedure rates which indicate that back surgery rates are more variable than many other types of surgery, and fusion rates are even more variable than spine surgery rates in general. This finding has been interpreted to suggest a poor professional consensus on the appropriate indications for performing spinal fusion. This is not surprising based on the literature which displays similarly confounding results with success rates of fusion for low back pain range anywhere from 32% to 99% [31]. In a 2003 review of over 7,000 patients and 84 articles Bono and Lee [13] determined an overall mean clinical successful rate of 76%. Breaking it down by decades, between 1979 and 1989 the success rate was 79% and between 1990 and 2000 it was 74%, indicating that there was no significant improvement despite the use of new techniques, instrumentation and other advancements that boast better fusion rates. This lack of consistent clinical success is discerning in light of its high cost, significant rates of complications, and prolonged postoperative recuperation time. In addition reports about fusion and its potential to accelerate degenerative changes in adjacent levels effect have been reported clinically [75, 77, 79] and demonstrated biomechanically [39, 120].

1.3.2 Arthroplasty

Limitations associated with fusion combined with encouraging results in knee and hip arthroplasty gave rise to the artificial disc. While literally hundreds of patents over the past half-century have been published (an extensive list is provided in the review by Szpalski et al. [137]) only a select few have actually made the elite rank of clinical implantation. The first attempt was reported in 1966 by Fernström [43], who tried to replicate the ball-joint of the disc with the insertion of a ball-bearing into the disc space. This technique was performed on about 250 patients before Fernström himself deemed the device a failure after repeated complications related to subsidence into the inferior vertebral body [137]. After this initially attempt others followed suit developing lumbar prostheses in France [42] and China [65] with disappointing results marked by numerous complications. Nothing promising surfaced until the late 1980s when three devices designed to overcome the setbacks of their predecessors appeared. After several device iterations the third generation Acroflex lumbar implant, made of a hexen-based polyfin rubber cushion sandwiched between two titanium endplates, showed promise in the lab but failed clinically after it was implanted in 50 patients. The remaining two devices, the SB Charité and the Prodisc, went on to successfully complete the Investigational Device Exemption (IDE) clinical trials and are currently the only two lumbar implants that are FDA-approved.

The SB Charité Artificial Disc

The Charité artificial disc was conceptualized in 1982 at the Charité hospital in Berlin by Schellnack and Büttner-Janz based on the low-friction articulation of Ultra High Molecular Weight Polyethylene (UHMWPE) on metal used in hip and knee prostheses [81]. This first model, known as Charité I, consisted of two stainless steel plates separated by an UHMWPE core, and attached to the surrounding vertebral endplates through anchoring teeth. Implanted in 1984, it showed promise, but concerns related to axial migration led to the Charité II with expanded 'wings' to better anchor the device. Both Charité I and II were never marketed outside of Germany and were only implanted at the Charité Hospital. Continued problems related to migration, subsidence, and metal fatigue led to the abandonment of these first two models and in 1987 a relationship was developed with the Link Spine Group to ameliorate these issues producing the LINK SB Charité III (Figure 1.4). This design stands today with minor modifications in terms of available sizes, choice of PE resin, endplate fixation and sterilization [81]. In 2003 DePuy Spine (Raynham, MA, USA) acquired the Link Spine Group and currently manufactures the renamed Charité artificial disc [70].

The Charité artificial disc gained FDA-approval for use within the United States in 2004. Results of the two-year follow-up, prospective, randomized FDA-IDE clinical study (which served as the basis of this approval) demonstrated that the artificial disc was equivalent to fusion with respective clinical success rates of 57.1% and 46.5% [12, 87]. The five-year follow-up, published in 2009, showed similar results [61]. While additional short and mid-term studies relay similar fair to good clinical outcomes [28, 59, 80], others report more cynical perspectives with apprehension of the device's long-term performance [114, 115, 140]. These concerns include: complicated revision surgeries, subsidence, subluxation, and facet joint arthrosis at both adjacent and/or index-level facets. With this in mind, the Charité artificial disc continues to be viewed as an experimental procedure.

Figure 1.4: FDA-approved lumbar total disc replacements: SB Charite III (left) and Prodisc-L (right)

The Prodisc-L Artificial Disc

Prodisc (Synthes Spine, Inc., Paoli, PA) was the second lumbar artificial disc to gain FDA-approval in August of 2006 [139]. Developed in the late 1980s, it was later implanted in 64 patients by its inventor, Dr. Thierry Marney, between 1990 and 1993 at the Clinique du Parc in Montpellier, France. Noting the apprehension surrounding lumbar disc replacements, Dr Marney waited through a full five-year follow-up period before performing any additional operations. His patience proved worthwhile when 93% of his patients reported satisfactory results with their implant. After a few design modifications a second generation device, Prodisc II was developed which went on to successfully complete the FDA's IDE study in the United States.

Similar in design to the Charité artificial disc, the Prodisc II is made of two metal plates separated by a UHMWPE core (Figure 1.4). The main difference is Prodisc's use of a fixed insert where the Charité's uses a semi-constrained PE core allowing it to translate on the inferior surface. Other variances exist, for instance instead of six small teeth Prodisc utilizes a single midline sagittal keel for anchorage to the surrounding vertebral bodies, but the difference between the constrained versus semi-constrained core has been the focus of debate between the two competing devices [46, 96, 117].

To date the Prodisc II shows initial signs of promise in short to mid-term studies available in the literature [150, 151], but being three years behind Charité long-term studies are lacking. This is not to say Prodisc is without adversaries. Complications such as accelerated facet degeneration, neuropathy, and segmental hyperlordosis have been reported [111, 125].

In general, total disc replacement (TDR) has yet to gain confidence within the orthopaedic community. Many surgeons argue that arthroplasty displays little to no improvements over fusion and runs the additional risk of complicated revision surgeries. In the end, arthroplasty may end up being a small niche market in the treatment of back pain as reports surface, indicating that only a very select group of patients are appropriate for TDR surgery [104] . While the debate continues, new devices are beginning to develop based on the lessons learned and extensive research gathered from the artificial disc.

1.3.3 New Technologies

Each year a sprouting of start-ups with promising non-fusion technology appear within the orthopaedic community. Recent developments include: second generation TDR devices designed to better match the anatomical and biomechanical properties of the natural disc (Spinal Kinetics, Sunnyvale, CA), total facet replacements (Facet Solutions Inc., Hopkinton, MA; Archus Orthopedics, Inc., Redmond, WA), interspinous devices to block extension (Impliant, Inc., Princeton, NJ; X-STOP, Medtronic Spine, LLC, Sunnyvale, CA), and novel surgical techniques to repair annular tears and post discectomy incisions (Xclose Anulex Technologies, Inc., Mennetonka, MN; Barricaid ARD Intrinsic Therapeutics, Inc., Woburn MA). Many of these technologies are just starting the long and tedious process of FDA-approval while others continually enter the pipeline. All of this suggests a revolution in treatment is eminent. With time, extensive biomechanical testing, and prudent clinical trials the technology that defines the future of spine surgery will eventually rise to the top.

1.4 Testing Protocols

Due to the difficulty of finding a well-matched animal model, pre-clinical biomechanical studies of motion preservation devices have primarily relied on *in vitro* human cadaveric studies. These studies typically involve one or more ligamentous FSUs potted in a fixture which attaches to a standardized testing machine. These machines apply known loads or displacements and the resultant response of the FSU(s) is recorded. The goal of biomechanical testing is to construct a protocol that is easily repeatable and approximates physiological loading conditions so devices can be functionally characterized as sufficient for clinical trial applications. This task has proven arduous without the surrounding musculature which, *in vivo*, creates complicated motion patterns along and about all three axes. In addition, these muscles are important for stabilizing the spine under axial load and without their support the ligamentous spine has been shown to buckle under relatively low load levels [24, 25]. This becomes problematic as axial loads are an integral part of our daily activities and therefore need to be included in simulations. This is especially true in the lumbar spine where large compressive loads (in excess of 1000 N) are experienced during daily activities such as standing and walking [91, 97].

Based on these complexities, biomechanical studies mainly focused on testing single motion segments until 1999 when Patwardhan et al. developed the compressive follower load [113]. This technique applies a load tangential to the spinal curvature (i.e., following the curve of the spine, hence 'follower load'), minimizing shear, and loading each segment with the same amount of compressive load with magnitudes up to 1200 N. Since then several other loading regimes have been developed, but by far, pure-moment loading with a compressive follower-load has become the most widely-accepted testing regime. Under this protocol, a follower pre-load of 400 N (average of about 60% of body weight above L3-L4) with a maximum of 1000 N is applied to the lumbar spine while the upper-most vertebrae is rotated through a pure-moment of $6 - 10$ Nm in an unconstrained, quasi-static manner (figure 1.5) [55]. The advantage of this method and the reason behind its eventual adaptation into the American Society of Testing Materials (ASTM) Spinal Implant Subcommittee's standardized testing procedure is its ability to test multi-segmental specimens with a uniform load across each segment. Despite its prevelance, there are several drawbacks. For one, this simple loading condition is not physiological and neglects several loading modes such as shear. In addition, it does not produce quality motion in modes other than flexion and extension [55].

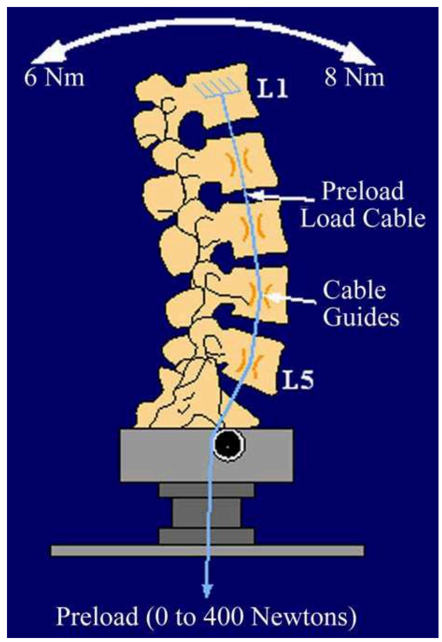

Figure 1.5: Diagram of a pure-moment set-up with a follower pre-load testing a six-segment lumbar specimen. (Picture adapted from Goel, V.K. et al. [55])

Regardless of the testing protocol, once the specimen is positioned in the testing frame additional sensors (strain gauges, pressure transducers, etc..) may be added to the specimen to capture other parameters such as force through the facets and nuclei pressure.

Data collection is typically recorded after several load cycles to equilibrate the viscoelastic elements of the specimen. For device evaluation, testing is first performed on the intact specimen followed by surgical manipulation at one or more levels. Kinematic and kinetic data for each FSU are then used to assess whether the device acheives adequate motion relative to the intact specimen and can tolerate physiological loads.

1.5 Kinematic and Kinetic Analysis

Kinematic and kinetic analyses are the two quantitative means for characterizing and comparing spinal devices to the natural disc [144]. Both are divisions of classical mechanics with the main difference being whether or not external forces and moments are taken into consideration. Kinematics describes the motion of bodies without taking into account the causes leading to the motion. Examples are range and patterns of motion. Kinetics, on the other hand, includes the study of the forces and moments responsible for motion.

Kinematics and kinetics are used in conjunction to provide a complete biomechanical picture of the device's performance. Unfortunately, acquiring sound kinetic and kinematic data from *in vitro* and *in vivo* research studies is not trivial. While various methods and techniques are scattered throughout the literature, concerns about accuracy, repeatability and the ability to elucidate movement in all six degrees of freedom continue plague biomechanical studies. The following dissertation focuses on two specific methods, the helical axis of motion (HAM) and the stiffness matrix, with the intent of strengthening their ability as effective tools for device evaluation.

1.5.1 Kinematic Analysis: Helical Axis of Motion

The primary kinematic parameter reported in biomechanical testing is range of motion (ROM). ROM refers to the translation or rotation along or about an anatomical axis from one extreme to another. It provides a quantitative assessment of a device's ability to match physiological extent of motion. While ROM may be adequate for determining the success of fusion surgeries, it does not fully characterize the complex three-dimensional motion provided by total disc replacements. For these devices, additional qualitative assessment is necessary to judge their performance. If a device does not effectively replicate the natural disc's pattern of motion, loads may be inappropriately distributed leading to unwanted outcomes such as facet arthritis, neuropathy, and adjacent segment degeneration.

Various methods for representing quality of motion have been presented, but in recent years a general consensus among the spine biomechanical community has formed in support of the helical axis of motion (HAM) [23]. HAM (otherwise known as the instantaneous axis of rotation and the screw axis) represents the motion of a rigid body as a unique axis about which and along which the body rotates and translates from one position to another (Figure 1.6). To determine HAM experimentally the relative motion of markers placed on the vertebral bodies of interest are tracked using optoelectronic cameras. Afterwards, one of several algorithms available to process the data is used to calculate the direction and location of the HAM as well as the angle and displacement about and along the axis. Commonly reported HAM metrics within the literature include its intersection and orientation with respect to specific anatomical planes.

Although HAM has been used to quantify intervertebral motion for over 30 years

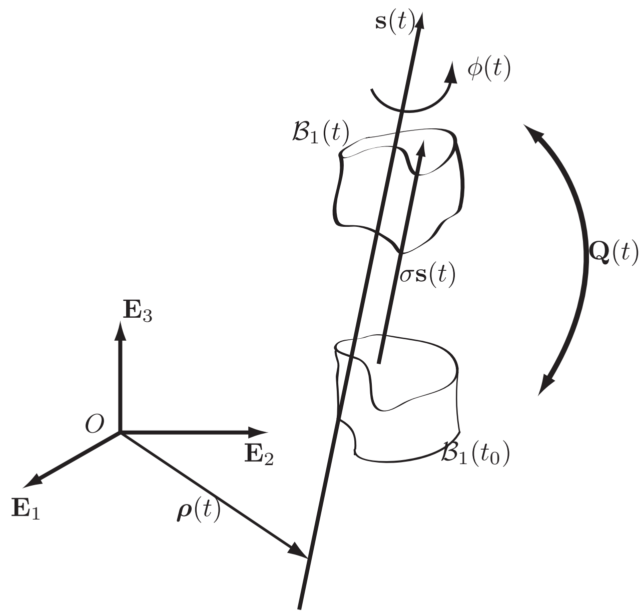

Figure 1.6: Schematic of the motion of a rigid body, $\mathcal{B}_1$, depicting the helical axis $\mathbf{s}(t)$, the angle of rotation $\phi(t)$, and the translation along the axis, $\sigma(t)$.

[107], the precision with which it can be measured experimentally has yet to be comprehensively discussed in the literature. In addition, varying displacement increments and multiple methods for calculating the parameters of HAM have been used, making it difficult to compare results between studies. To address these issues chapter 3 of this dissertation is focused on producing a set of best practices in characterizing and minimizing HAM error. The result of this study will determine the effect of intrinsic errors in HAM experimental measurements on our ability to compare the kinematics of motion preservation devices.

1.5.2 Kinetic Analysis: Stiffness Matrix

Load-displacement behavior of individual FSUs is a common kinetic means to characterize and compare various arthroplasty devices. In most cases a uniaxial load (i.e., pure moment with or without an accompanying follower-load) is applied to one or more FSUs and the resultant load-displacement curves are reported graphically. While this method is consistent, easily repeatable, and widely accepted, it has several drawbacks. Most apparent is that physiological loads rarely occur about or along a single axis and are more likely to consist of a combination of loads. In addition, FSUs consists of three joints, the intervertebral disc plus the two facets, and is non-symmetric in the coronal and transverse planes. This leads to coupled motion, a phenomenon in which there is an association of translation or rotation in one axis with motion about or along a second axis [144]. A common example can be seen during flexion in which case the FSU rotates about the horizontal axis while translating anteriorly. Uniaxial load-displacement curves do not account for this complex motion and therefore do not accurately represent overall spinal kinetics..

One metric that can accommodate these complexities is the 6x6 stiffness matrix. This 36-term matrix provides a stiffness coefficient for each on-axis (6 diagonal terms) and off-axis coupling (the remaining non-diagonal terms) response to any particular loading regime. The stiffness matrix, K, is calculated by measuring the displacement of a FSU in all 6 degrees of freedom during loading using the following relationship:

$$\mathsf{F} = \mathsf{F}_0 - \mathsf{Kd}. \tag{1.1}$$

Panjabi et al. was first to introduce the stiffness matrix to the spine in 1976 with their work on the 3-dimensional stiffness of the thoracic spine [109]. By assuming conservation of energy, symmetry about the sagittal plane, and that certain motions do not have a coupling effect, they reduced the number of coefficients to be determined from 36 to 12.

Once these assumptions were established, the 12 individual stiffness coefficients of cadaveric FSUs were measured experimentally by inverting the flexibility matrix. Initially the aim of this research was to provide experimentally-derived spine behavior data for incorporation into mathematical models. While there is no evidence that the authors themselves actually followed through with this application, later works by Stokes and Gardner-Morse made extensive use of this initial data set [49, 50, 132–134]. From 1995 to 2001 Stokes and Gardner-Morse used Panjabi et al.'s thoracic stiffness matrix to develop finite element models [50], surgical simulations [132], complex models to analyze lumbar muscle forces [133], eigenvalue bucking analyses of the spine [49], and optimization problems related to spinal muscles forces [134]. Noting the limitations associated with Panjabi et al.'s thoracic stiffness matrix, Stokes and Gardner-Morse eventually went on to develop their own method for experimentally determining the stiffness matrix in 2002 [135]. By using a Stewart-Platform-like testing machine which facilitated control over all 6 axes of movement, they were able to measure the stiffness matrix of a porcine FSU directly, eliminating the errors associated with inverting the flexibility matrix. Other improvements include the addition of a physiological preload, characterization of all six degrees of freedom, and testing in a fluid environment to better simulate *in vivo* conditions. This same testing device was later used in subsequent papers to further analyze the effects of preload on porcine specimens [51] as well as human lumbar FSUs before and after the removal of the posterior elements [52].

Unfortunately even with these improvements the stiffness matrix still has several restrictions limiting its utility. The most problematic is the inability to accommodate finite rotations and energy losses due to the poro-viscoelastic nature of the intervertebral disc and the nonconservative forces and moments due to the facet joints and ligaments. These and other deficiencies are addressed in chapter 4 by presenting an alternative method of calculating the stiffness matrix of a motion segment. In addition, a method for distilling the 36-component matrix into a single scalar is presented making it easier to convey the stiffness matrix to clinicians and use it as a statistical comparative tool before and after surgical manipulations. Prior to this work the stiffness matrix has not been used as a comparative tool.

1.6 Goal

The goal of this dissertation is three-fold. First, design issues related to current FDA-approved TDRs are investigated in chapter 2 using a unique testing protocol that includes physiologic shear forces. In chapter 3, the accuracy and efficacy of using HAM as a kinematic tool for characterizing motion preservation devices is thoroughly investigated. Lastly, chapter 4 presents an improved method for calculating the stiffness matrix and discusses the possibility of using it as a kinetic metric for evaluating TDRs. The conclusion examines the role of HAM and the stiffness matrix in analyzing TDRs and their potential in facilitating the design of next generation devices. This is followed by suggestions for future work.

Chapter 2

Facet Joint Stress after TDR: An In Vitro Investigation of Posture and the Sensitivity of Sagittal Device Placement

2.1 Introduction

Total disc replacement (TDR) technology has generated considerable clinical interest as an alternative to fusion surgery. This enthusiasm stems from the teleological view that motion preservation is beneficial to the patient in the long term, principally due to reduced risk for adjacent segment disease. That is, by supporting motion through mechanical means, it is hoped that TDR surgery will avert a cascade of degeneration to adjacent, untreated levels. This notion is based on research suggesting that elimination of motion via fusion at one level causes neighboring segments to compensate through increased stress and motion which in turn leads to accelerated disc and facet degeneration [75, 76]. Two TDR designs have been FDA-approved for use in the lumbar spine: the CHARITÉ (DePuy Spine, Raynham MA) and the Prodisc-L (Synthes, Paoli, PA), both of which consist of a metal-on-polymer articulating surface with the main kinematic difference being the CHARITÉ's mobile core as opposed to Prodisc-L's fixed core. Ideally, TDRs restore normal functional spine unit (FSU) kinematics, which depends on the implant's cooperative interaction with the facet joints. While the extent by which TDR restores physiologic FSU motion remains unclear, it is becoming apparent that the complexity of FSU kinematics is not fully mimicked by the ball-and-socket design of these devices [104].

In the normal FSU, the biomechanical roles of the disc and facets are complimentary, with the disc primarily supporting compression and the facets helping to resist shear and guide the FSU motion trajectory. Consequently, it is expected that the facet joints will invariably experience altered stresses when the biologically-complex and pliant disc is replaced by a rigid mechanical device. Even small changes in stress patterns may lead to cartilage damage and gradual disease progression. Alterations in joint kinematics can expose local areas of cartilage to higher than normal stresses and loading-rates [5, 6, 48, 138]. Articular cartilage, which lines the two articulating facets, responds to these pathological changes through biosynthetic dysfunction and accumulation of damage lending itself to osteoarthritis [7, 17, 60].

The consequences of TDR design on facet stresses are not well understood. Using an in vitro validated finite element model, Goel et al. investigated loading sharing among various structures at the implanted and adjacent level [53]. They reported a decrease in facet loads at both the instrumented and adjacent segments. Rousseau and colleagues preformed an in vitro study and noted that at L5/S1 the CHARITÉ's mobile core design leads to increased facet forces when compared to intact FSU, whereas the Prodisc-L TDR causes an overall unloading of the facets [117].

In theory, sagittal placement of the prosthesis within the intervertebral disc space will play a role in how the TDR interacts with the facet joints. The "ideal" position according to the manufacturer's recommendation is centered on the endplate, but whether this is indeed the ideal location from a biomechanical perspective has not been fully investigated. Clinical studies have attempted to address the issue using in vivo methods such as radiographic signs of facet arthritis and degeneration, but the results are conflicting and rely on subjective outcome measures [28, 80, 112, 152]. Detailed mechanical studies are limited. Using finite element methods, Dooris et al. concluded that the facets are better protected when the TDR device is implanted in a posterior position [34]. Their model predicted no facet loads during compression when the device is placed posteriorly, whereas an anteriorly placed device resulted in facet forces that were 2.5 greater than the intact disc.

The goal of the current study was to investigate posture-dependent the changes in facet loads due to surgical placement of the Prodisc-L device at L5/S1. In addition, sensitivity of implant sagittal alignment was explored to determine whether a centered TDR placement is kinematically ideal.

2.2 Materials and Methods

2.2.1 Specimen Preparation

Healthy, non-degenerate fresh-frozen human lumbosacral vertebrae from six donors (mean age: 44, 3F/3M) were selected. Care was taken to ensure each specimen was without bone disease, disc degeneration or facet arthritis. The L5/S1 ligamentous motion segment was isolated and potted in PMMA with the S1 endplate parallel to the potting surface. Specimens were wrapped in gauze soaked in saline solution infused with a protease inhibitor cocktail (Sigma-Aldrich, St. Louis, MO) during testing.

2.2.2 Mechanical Testing

Using a previously established protocol, the specimens were subjected to a combination of compressive and shear loading using a servo-hydraulic system (MTS Corp, Eden Prairie, MN) while in nine different rotational positions: neutral, 3° and 6° of flexion, extension, and left and right lateral bending, by adding wedges at the interface (Figure 2.1) [117, 118]. This testing apparatus was specifically designed to match loads experienced at L5/S1 based on the average sacral slope in the standing position.

Each load application was held for 2 minutes of which data was collected during the final 10 seconds. The rotation of L5 was measured using an optical tracking device (Motion Analysis Corp., Santa Rosa, CA). The load cell, facet sensors, motion cameras, and servo-hydraulic system were synchronized and recorded with LabView software (National Instruments Inc, Austin, TX).

Facet forces were measured using thin (0.1mm) pressure sensors (6900, Tekscan

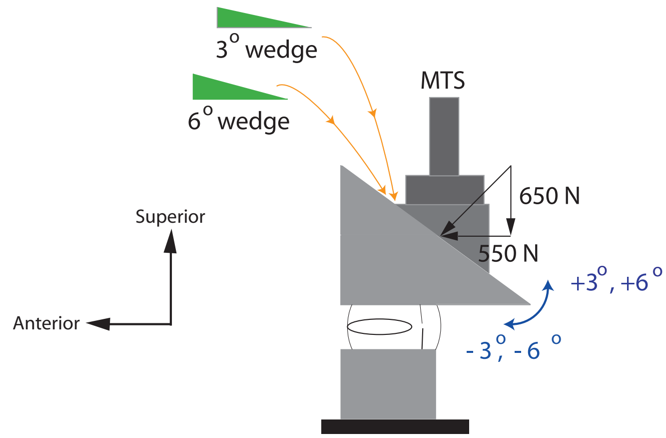

Figure 2.1: Schematic diagram of experimental set-up. 850 N was applied using the MTS machine at a 40^o angle (average sacral slope). 3^o and 6^o wedges were used to achieve the desired rotations in the sagittal and frontal planes.

Inc., South Boston, MA) that were carefully inserted into both the left and right facet capsule through a vertical incision. These sensors provided a 14 mm by 14 mm sensing region consisting of 121 sensels each with a spatial resolution of 0.62 mm^2. Sensor output was monitored and recorded using Tekscan's software which displayed each pixel, providing real-time feedback to ascertain that the sensor was properly placed within the capsule. Afterwards spray adhesive was applied to prevent migration during testing. A new sensor was used for each set of tests to minimize the effect of sensor wear. Prior to insertion, each sensor was calibrated based on the linear protocol described by Wilson et al. [145].

Specimens were initially tested with the disc intact. Once completed, an appropriate sized (4 medium, 2 large, all 6°/10 mm) Prodisc-L device was implanted by an orthopaedic surgeon 3 mm posterior to center of the inferior endplate based on lateral x-rays (Faxitron X-Ray, LLC, Wheeling, IL). After testing in the posterior position, the device was moved 3 mm anteriorly to the center of the endplate using Synthes' surgical instrumentation. The procedure was repeated once more for testing in the 3 mm anterior position. The decision to start in the posterior position and move the device incrementally forward was made to avoid resetting the chisel cuts for the device's central keel. Typically, intact tests were completed in one day, and all three device cases were completed the following day. Refrigeration and saline gauze were used to preserve specimens overnight and prevented deterioration between testing.

2.2.3 Data Analysis

Means and standard deviations for facet pressures (N/mm^2) were reported as opposed to facet forces in order to moderate differences between facet sizes among the specimens. Multivariate regression techniques and paired t tests were performed to determine whether there were statistical differences between the intact facet pressures and those experienced in the three device cases for each of the nine postures (JMP 7.0, SAS Institute Inc., Cary, NC). This analysis was repeated to compare the intact case to the combined device case (anterior, posterior and mid-placement) to determine the overall effect of the device despite the consequences of its surgical placement.

2.3 Results

The data presented here are the total facet pressures, representing the summation of left and right facet pressures. These were averaged across all six specimens, and the resultant mean for the nine different postures were graphically organized into rotations in the sagittal and frontal plane (Figures 2.2 and 2.3). Continuous lines were added between data points to illustrate trends between the four different testing conditions.

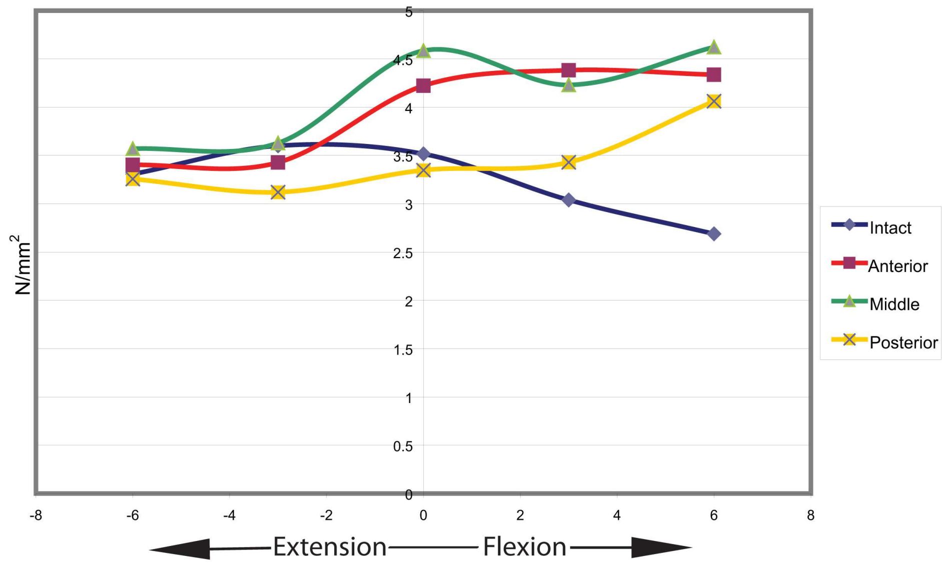

Figure 2.2: Average facet pressures were not altered by TDR in extension. However, after TDR the pressures were increased during flexion. Points on the graph indicate recorded data (at 3^o and 6^o extension, neutral, and 3^o and 6^o flexion). A continuous line connecting the point has been added to illustrate the trend from extension to flexion.

With the intervertebral disc intact, facet pressures were highest in extension and decreased as the specimens rotated into flexion during sagittal plane motion (Figure 2.2). In the frontal plane, ipsilateral pressure increased during left and right lateral bending. This effect was negated as summed left and right pressures are displayed resulting in a relatively flat trend across the frontal plane (Figure 2.3).

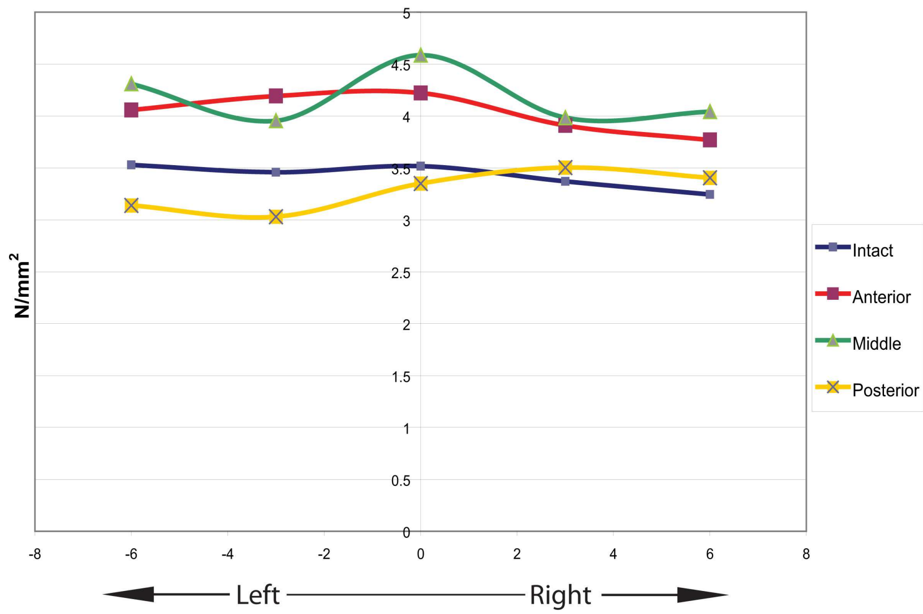

Figure 2.3: During coronal plane motion anterior and central placement of the device resulted in higher facet loads. Points on the graph indicate recorded data (at 3^o and 6^o left lateral bending, neutral, and 3^o and 6^o right lateral bending). A continuous line connecting the point has been added to illustrate the trend from left to right lateral bending.

Implantation of the TDR resulted in comparatively higher facet loads during flexion, reaching statistical significance (P = 0.0132) in the most extremely flexed position of 6 degrees (Figures 2.2 and 2.4). All three devices cases share the same trend of increasing pressure from extension to flexion during sagittal plane motion. This is the reverse of the trend seen during intact testing. During lateral bending, ipsilateral facet pressures increased during lateral bending. This result is similar to the intact disc and again the two facets cancel out and the pressures along the frontal plane appear flat (Figure 2.3).

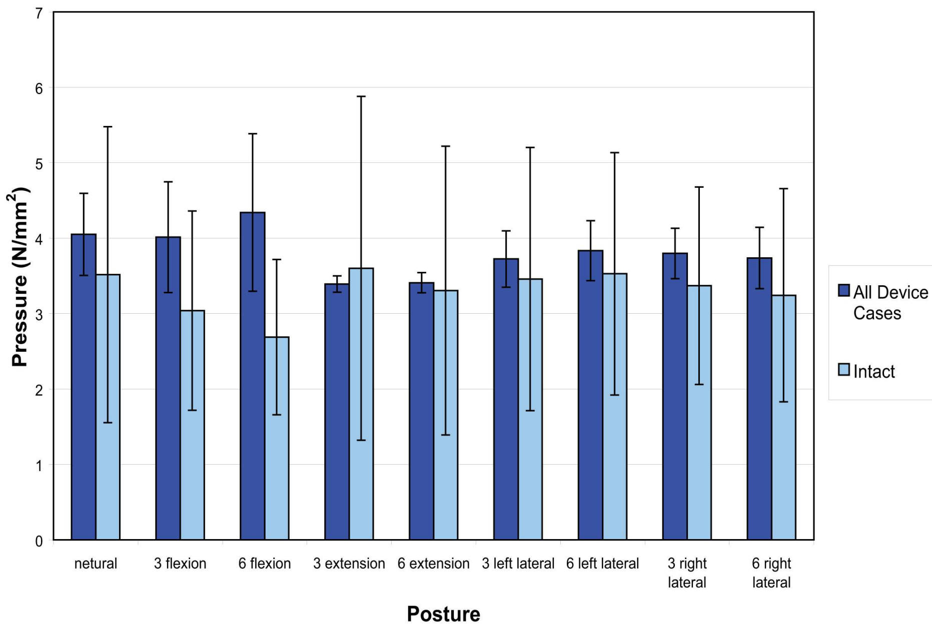

Figure 2.4: Average total facet pressure (+/− standard deviation) normalized to the intact motion segment in the 9 different postures (neutral, 3^o and 6^o of flexion, extension, left lateral and right lateral bending). Statistical analysis between the intact and all devices were not significant ($p \geq 0.05$).

Overall, the centered and anteriorly-placed TDR resulted in higher total facet pressures compared to the intact disc, with the exception of the two extended postures. Conversely, the facets in the posteriorly placed implant experienced pressures that were near to or below those of the intact disc.

2.4 Discussion

The attractive simplicity of the ball-and-socket prosthetic joint has proven effective in the hip and has seen promise in cervical spine [14]. It is not surprising that lumbar TDR development has followed a similar path. However, in order for this design to achieve clinical success in the lumbar spine it is important to factor the increased mechanical forces (particularly shear) and specific facet joint anatomy. We investigated changes in facet loading post-TDR with respect to sagittal placement of the Prodisc-L device. Overall, we observed that the Prodisc-L increased facet forces except when placed in the most posterior position compared to the intact motion segment. Also, it was of particular interest that patterns of facet loading during sagittal plane movement with the implant were opposite that of the intact case regardless of its position. That is, after TDR, facet forces tended to increase with flexion. These changes combined with the increased facet forces could potentially lead to facet arthritis and/or other deleterious effects over time, particularly since higher overall spine forces are associated with the flexed posture [47].

During physiological daily activities, the lower lumbar spine experiences large anterior and posterior (AP) shear forces reaching magnitudes of over 1500 N during lifting tasks [57]. In addition, due to lordosis, the lumbosacral joint is subjected to anterior shear stress in the upright standing position. Therefore appropriate in vitro loading conditions which approximate this effect, such as those used in the present study are necessary to accurately determine the biomechanical effects of lumbosacral TDR. Previous studies evaluating prosthetic kinematics primarily utilize the widely accepted pure moment protocol that imposes no shear force on the specimen. This neglects one of the most significant loading modalities responsible for low back disorders as described in occupational studies [33, 47] which, in part, may explain the discrepancy between positive device outcomes in vitro and the lack of long-term clinical data to support these results [26, 53, 80, 99, 104, 111, 124, 140].

In healthy non-degenerate spines, strain within the annular fibers of the intervertebral disc provide the primary source of shear resistance while the posterior elements – ligaments during posterior shear, and the facets during anterior shear – are there to assist the disc and prevent excessive translation [119, 148]. Thus, if the disc is altered in such a way that compromises its ability to oppose shear loads, a greater burden is placed upon the posterior elements [68]. TDR implantation necessitates removal of the nucleus pulposus and the majority of the annulus, leaving the coupled curvature of the superior articulating surface with the polyethylene inlay as the primary source of shear resistance.

The effectiveness of ball-and-socket TDR to resist shear is dependent on the degree of overlap between the two articulating surfaces. This overlap, however, is posture dependent (Figure 2.5). Assuming negligible friction and uniform contact pressure, the resistance to shear is the integral of the pressure multiplied by the local area under the superior endplate on the side opposite of the imposed shear:

$$\mathbf{R_x} = \iint \partial\sigma \partial A = \iint \partial\sigma \frac{\pi r^2}{360} \partial\theta \tag{2.1}$$

Inserting the geometric data for the Prodisc-L device, this equation becomes

$$\mathbf{R_{x_{6^o extension}}} = \int \partial\sigma \int_{\theta=0^o}^{\theta=41.5^o} \frac{\pi r^2}{360} \partial\theta = \int \partial\sigma \frac{83\pi r^2}{720}, \tag{2.2}$$

in full extension, and

$$\mathbf{R_{x_{6^o flexion}}} = \int \partial\sigma \int_{\theta=0^o}^{\theta=29.5^o} \frac{\pi r^2}{360} \partial\theta = \int \partial\sigma \frac{59\pi r^2}{720} \tag{2.3}$$

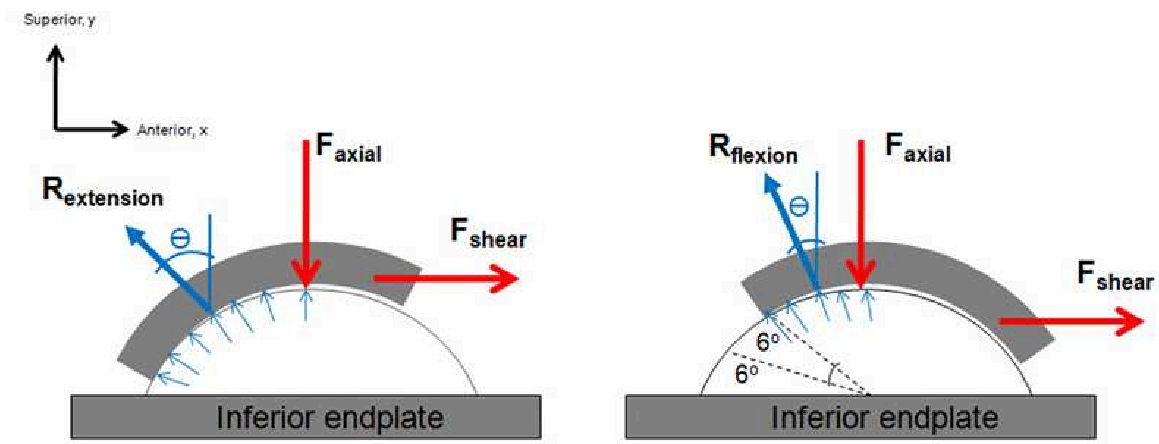

Figure 2.5: As the superior articulating surface rotates about the polyethylene inlay from extension (left) into flexion (right), there is diminished implant surface to resist anterior shear. θ is the angle measured from the midline of the device, σ is the stress on the surface of the inlay, and Rx is the component of the reaction force that resists the imposed shear

in full flexion. Prior to dislocation, this resistive force balances the compression and shear imposed on the device. It is evident that as the superior endplate rotates into flexion, less contact area is available to resist anterior translation of the superior vertebral body.

This sagittal-plane analysis provides a mechanical rationale for our experimental observations: that the Prodisc-L's ability to resist shear decreases with flexion (and hence the facet forces increase; Figure 2.5). Consistent with historical observations, we note that prior to TDR, the facet joints carry a higher percentage of force during extension which decreases as the specimen rotates into flexion [2,36,82,147]. This trend can be conceptually explained through the increased overlap between the superior and inferior facet surfaces in extension and the decreased height of the posterior column. After TDR implantation however, we observed the opposite trend with all three sagittal placements (anterior, centered, and posterior) of the device. Since with flexion the device becomes less capable of resisting shear (Figure 2.5), a greater burden is placed on the facets to achieve static equilibrium. This mechanism for increased facet pressure after TDR is supported by comparison between the experimentally measured average facet pressures and the theoretically-derived posture effect on the device's resistance to shear (Figure 2.6). This flexion-dislocation phenomenon is intrinsic to the ball and socket design.

Both the Prodisc-L and the CHARITÉ, rely on a similar ball-and-socket design in an effort to preserve motion across the disc space. The main difference between the two is CHARITÉ's mobile core. Theoretically, this provides even less shear resistance and in turn would place more stress on the posterior elements. In support of this theory, Rousseau et al. compared the two devices in a study similar to that presented here and reported significantly higher facet forces with the CHARITÉ [117]. Their facet forces were an order of magnitude lower than ours, but this is most likely due to differences in the sensor's ability to capture all of the force through the facets. The Flexiforce Tekscan sensor used in the Rouseau et al. study has a smaller sensing area (10 mm diameter circle) than that of the 6900 sensor (14x14 mm square) we used. Further evidence of inadequate shear resistance offered by the CHARITÉ are reports of post-operative anterior subluxation and migration [140].

Generally, we observed that TDR increased loads in the posterior elements and was most apparent in the mid and anterior positions. Posterior placement alleviated this effect, and in some cases reduced the facet loads to levels below that experienced with the disc intact. Dooris et al. reported similar results with a finite element model of the L3-L4 motion segment [34]. This unloading may be explained by greater distraction of the device in the posterior position. This, in theory, preserves tension in the posterior ligamentous structure and in turn maintains stability across the segment.

The most apparent limitation of this study is the lack of statistically powerful data. Several factors attribute to this result. For one, the complexity of this study combined with the difficulty of obtaining healthy spines within a practical amount of time restricted the number of specimens available for testing. Also, specimen variability in terms of size, shape, and degree of lordosis presumably contributed to inconsistencies within the data. Lastly, inaccuracies specific to Tekscan are accountable for a portion of the relatively large standard deviation. These inaccuracies have been reported in previous studies using the 6900 sensor in the facet joint and are estimated to be within 18% at 100 N [98, 145].

Despite these limitations, the combination of our experimental results and their mechanical interpretation suggests a flexion-dislocation phenomenon and provides support for reports indicating that suboptimal interactions between the implant and facets can have significant clinical consequences. For example, in a two year follow-up study by Park et al. adjacent segment disc and facet degeneration were found to be minimal, while nearly 30% of TDR segment facets experienced progressive facet degeneration [111]. Similarly, using fluoroscopically guided spine infiltrations, Siepe et al. reported the facet joint at the index level is the predominate source of pain in the lumbar spine, most significantly at the L5/S1 [125]. While further research into this phenomenon is needed, it is particularly discerning that the greatest discrepancy in load occurred during flexion. This is the most frequently relied upon posture for lifting and other load-bearing activities and should bear careful consideration in TDR design.

Our data demonstrate that there is a need to develop an improved understanding of the complexity of spine biomechanics after TDR. For the optimal clinical benefits of motion-preservation to be realized, physiological loading conditions need to be considered and improved design criteria developed. Until then, clinical studies are likely to continue to reveal inadequacies and reports of suboptimal performance.

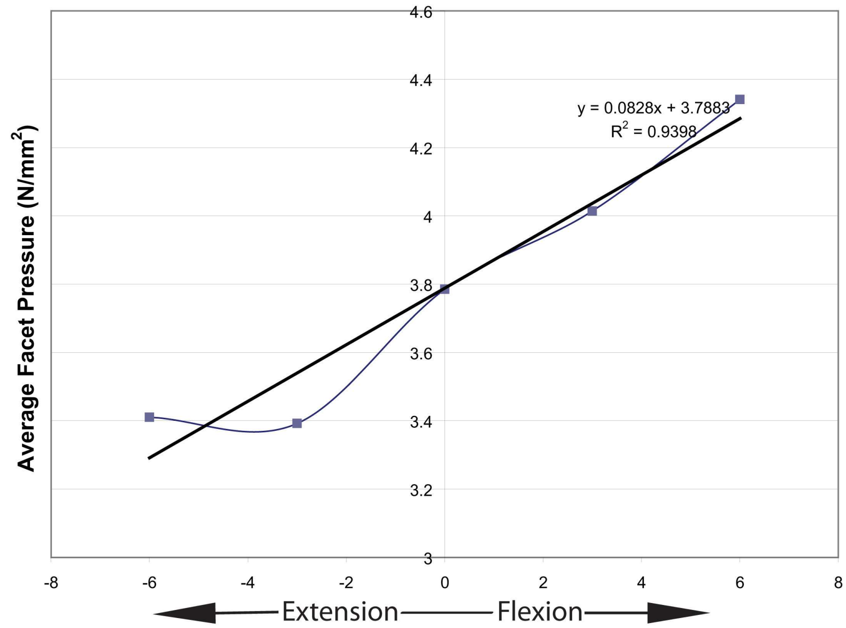

(a)

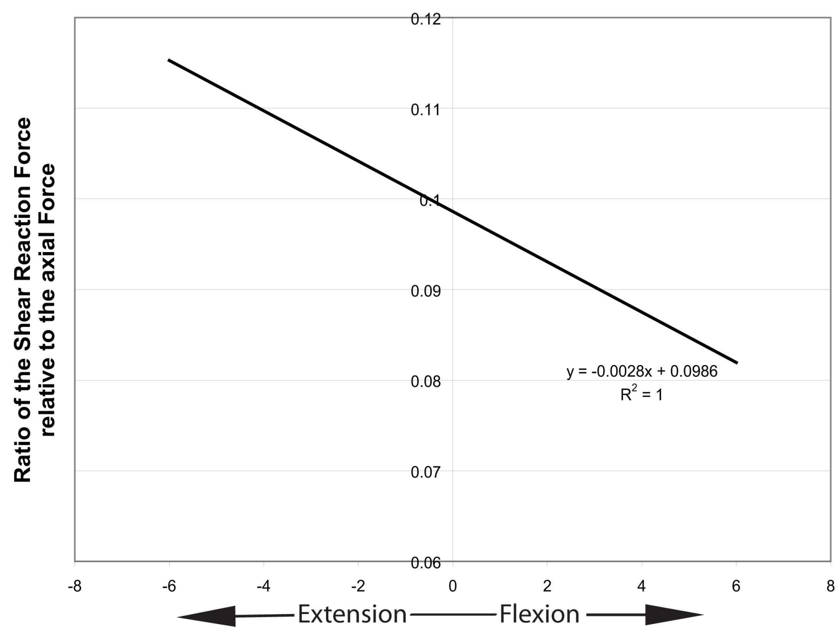

(b)

Figure 2.6: After TDR, the average facet pressures (mean pressure of all device placements from Figure 2.2 revisited as a line graph) increase progressively when the motion segment moves from extension to flexion (a) . Due to posture-dependent changes in joint congruity (Figure 2.5), there is a theoretical decrease in shear resistance as the motion segment rotates from extension to flexion. (b)

Chapter 3

Minimizing Errors Associated with Calculating the Helical Axis of Spinal Motion

3.1 Introduction

Physiologic spinal motion entails relative rotation and translation of vertebrae in all three anatomical planes. The goal of motion preserving implants, such as total disc replacement, is to best approximate this motion with mechanical devices. In order to test the efficacy of these products, it is important to quantitatively characterize the three-dimensional motion of both intact and treated spinal sections. One of the most commonly used biomechanical metrics for characterizing three-dimensional joint movement is the helical axis of motion (HAM). Although HAM has been used to quantify intervertebral motions for almost 40 years [106], the precision with which this metric can be measured experimentally has yet to be comprehensively discussed in the literature. Clearly, it is necessary to characterize the intrinsic errors in HAM experimental measurements as an integral part of kinematic assessment of motion preserving devices.

The three-dimensional motion of a functional spinal unit (FSU) may be fully characterized by a rotation about, and translation along, the HAM. Commonly used HAM metrics in the biomechanics literature include the orientation of the helical axis vector and the intersection of this vector with specific anatomical planes. HAM is determined experimentally by tracking the 3-D location of physical targets that are attached to spinal levels of interest. Regardless of the motion tracking system used, intrinsic experimental errors are present in all target position measurements; most commercial motion tracking systems have target location errors of $\pm 0.1 - \pm 0.25$ mm.

The HAM is calculated from target spatial coordinates using a motion-fitting algorithm which are nonlinear. As a consequence, target location errors propagate through to errors in HAM estimation leading to erroneous results that may lead to inaccurate interpretations of treatment efficacies. While several motion-fitting algorithms have been referenced within the spine literature, most notably the algorithm specified in [74] and the singular value decomposition (SVD) method of [146] there is no clear consensus as to which algorithm best minimizes HAM error (Table 3.1). To the best of our knowledge, only [73] have analyzed the errors associated with their experimental method; however, we were unable to determine the exact algorithm used.

Error comparisons of some of the different existing algorithms and noise character-

Article	Method Used	Error Analysis(y/n)
[15]	SVD	no
[18]	SVD	no
[22]	SVD	no
[58]	SVD	no
[73]	unspecified	yes
[98]	direct	no
[105]	direct	no
[118]	direct	no
[117]	direct	no
[149]	direct	no

Table 3.1: Use of the Helical Axis of Motion to Analyze Spinal Motion

istics have been performed separately by a number of different researchers. [146] performed a theoretical analysis of the HAM parameter error propagation under the assumption of zero mean, uncorrelated, isotropic noise, the results of which were validated by [130] using numerically generated data. [30] went further and compared the errors predicted by the analytical model of [146] to the actual errors using roentgen-stereophotogrammetry under a number of different experimental conditions. However, their paper does not include a comparison to the errors associated with any of the other existing algorithms used to determine the HAM parameters. This was followed by a comparison of the algorithms presented in [131] and [146] (developed as an improvement to that proposed by [131]) by [128] who deemed the latter more accurate, especially for ill-conditioned problems. Recently, [38] compared the singular value decomposition method of [9], the unit quaternion method of [63],[1] the orthonormal matrix method of [64] and the dual quaternion method of [143] using data with uncorrelated, isotropic, Gaussian noise and found no single method to be statistically

[1]This was independently developed by Davenport [71] as a solution to the error minimization problem in satellite dynamics posed by Grace Wahba in the1970's.

superior either in accuracy or stability to any of the others. [35] expanded upon this by considering the effect of experimental noise in a preferential direction (as in stereo vision), as well as the effect of the shape of the object in question, on the propagation of error in determining the rigid body motion parameters. All of the above analyses are similar in that they rely on numerically generated data to approximate errors that occur experimentally.

In this paper, we used experimental as opposed to artificially generated data to compare the errors associated with three motion-fitting algorithms. Two of these methods, referred to as the 'direct' method [74] and the 'SVD' method [146] respectively, are widely used in the spinal biomechanics community (Table 3.1) while the third method, denoted the 'triad' method is unique to spacecraft dynamics and was originally published in [123]. Our paper improves upon the analysis of [30] by comparing three different algorithms as opposed to focusing on the SVD method alone.

The results of our analysis were then used to identify the best approach for minimizing HAM error. An *in vitro* biomechanical case study was utilized to illustrate the relative magnitude of HAM error relative to kinematic changes that occur due to spinal instrumentation. A comparison between the theoretical error estimates and the actual errors was also performed to determine if the errors estimated mathematically accurately reflected the true errors. This improves upon that presented in [30] which focuses only on the SVD algorithm detailed in [146]. Clinically, this work is intended to help clarify whether experimental measures of HAM are sufficiently accurate to characterize the kinematics and clinical utility of spinal motion preserving devices.

3.2 Background

Any rigid body motion can be defined as a rotation about, and a translation along the helical axis of motion. In spinal kinematics, the main parameters of interest are the helical axis' directional vector, $\mathbf{s}$, the angle of rotation, Φ, the displacement $\mathbf{d}$ relative to the origin, and the point of intercept of the HAM with a particular plane of interest: $\boldsymbol{\rho}$. Each of the three algorithms mentioned utilize different techniques to compute the parameters of the HAM. These differences give rise to various levels of accuracy and repeatability when calculating the HAM in noisy environments such as those present in biomechanical testing. In this section, we first provide a brief outline of rigid body kinematics with respect to the relative motion between two vertebral bodies. This is followed by a brief description of the algorithms used to determine the HAM parameters of interest.

3.2.1 Spinal Kinematics

In spinal kinematics, the rigid body of interest (distal-most vertebral body) is defined by a set of 4 markers (targets) for all 3 methodologies, where $\mathbf{A}^K$ and $\mathbf{a}^K$ denote the position of the K^{th} marker in the initial and final configurations, respectively. (Cf. Figs. 3.1 and 3.2 below.)

We define

$$\mathbf{A}^K = \sum_{i=1}^{3} A_i^K \mathbf{E}_i, \qquad \mathbf{a}^K = \sum_{i=1}^{3} a_i^K \mathbf{E}_i, \tag{3.1}$$

where $\mathbf{E}_i$ and $\mathbf{e}_i$ refer to the fixed and rotated coordinate systems, respectively. Since both

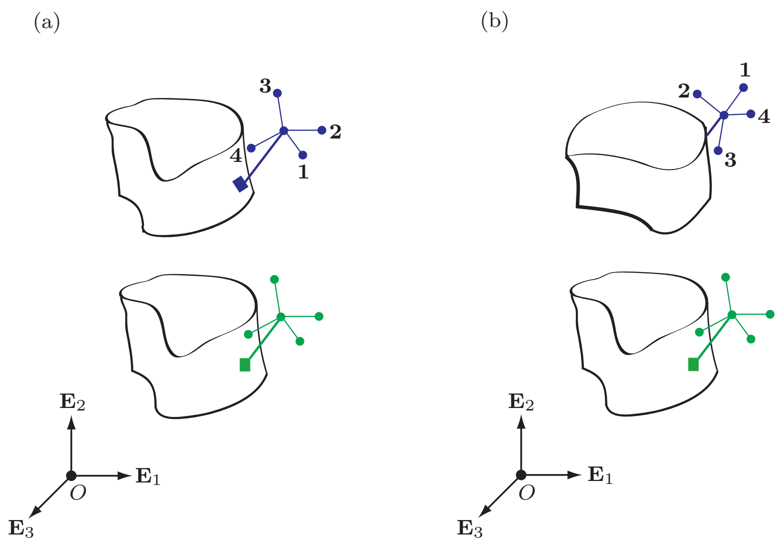

Figure 3.1: Motion of the caudal vertebra relative to the (fixed) cephalad vertebra. Both vertebras have a set of four markers attached to them which are labeled 1,2,3, and 4. The upper vertebra undergoes a rigid body motion relative to the lower vertebra which is fixed in space. The relative motion is determined by comparing the position of the markers on the upper vertebra (a) before and (b) after the motion as detailed in the text.

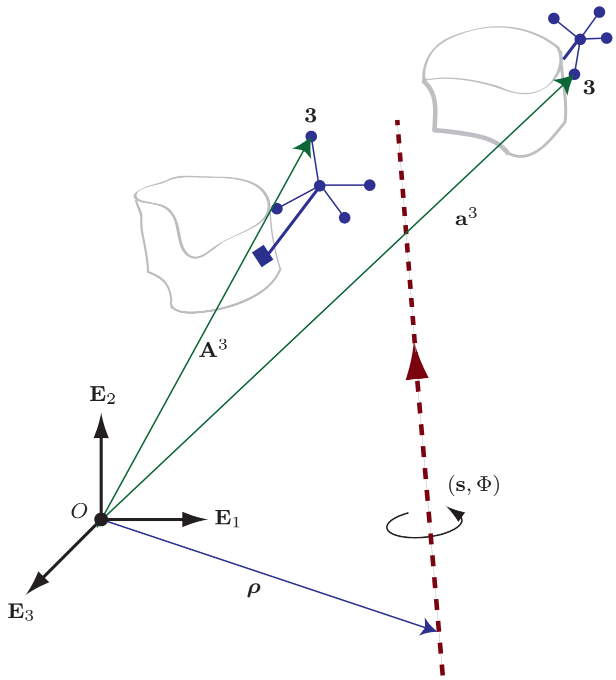

Figure 3.2: A close up view of the motion of the upper vertebra. The rigid body (and attached markers) are rotated and translated about the HAM (represented by the red arrow) from their initial position given by $\mathbf{A}^K$ into their final positions $\mathbf{a}^K$, $K = 1, 2, 3, 4$. The figure shows how the representative marker labelled 3 with an initial position vector of $\mathbf{A}^3$ is rotated and translated about the HAM to $\mathbf{a}^3$.

$\mathbf{A}$ and $\mathbf{a}$ are expressed in the fixed frame system, we have,

$$\mathbf{e}_i \quad = \quad \mathbf{Q}\mathbf{E}_i \quad \text{or, in component form} \quad \mathbf{e}_i = Q_{ik}\mathbf{E}_k. \tag{3.2}$$

As $\mathbf{a}^K = \mathbf{Q}^K(t)\mathbf{A}^K + \mathbf{d}^K(t)$, it follows that

$$\mathbf{a}^K = \sum_{i=1}^{3} a_i^K \mathbf{E}_i = \sum_{i=1}^{3}\sum_{j=1}^{3} \mathsf{Q}_{ij}^K A_j^K \mathbf{E}_i + d_i^K \mathbf{E}_i, \qquad K = 1, \ldots, N, \tag{3.3}$$

where $\mathbf{Q}$ is the rotation matrix with components $Q_{ij} = \mathbf{e}_i \cdot \mathbf{E}_j$, and $\mathbf{d}$ is the displacement vector given by,

$$\mathbf{d} = \mathbf{a} - \mathbf{Q}\mathbf{A} = (\mathbf{I} - \mathbf{Q})\,\boldsymbol{\rho} + \alpha\mathbf{s}. \tag{3.4}$$

Here, $\boldsymbol{\rho}$ is the position vector of the HAM with respect to the origin, and α corresponds to the component of the displacement that is parallel to the helical axis as depicted in Figure 3.3. Note that the value of α does not depend on the $\boldsymbol{\rho}$ used to determine the position of the HAM, and represents the amount of translation that is parallel to the HAM. In this paper, we focus on the vector $\boldsymbol{\rho}$ pointing from the origin to the point of intercept of the helical axis with a plane of interest. A brief note on the displacement vector is provided in the Appendix section of this study.

3.2.2 Algorithms

The direct, SVD, and triad methods each have a unique method for determining $\mathbf{Q}$ and $\mathbf{d}$. In addition, each of the methods mentioned utilize $\mathbf{Q}$ and $\mathbf{d}$ in a different manner in order to acquire the desired parameters, Φ, $\mathbf{s}$, and $\boldsymbol{\rho}$ that are of interest in spinal kinematics.

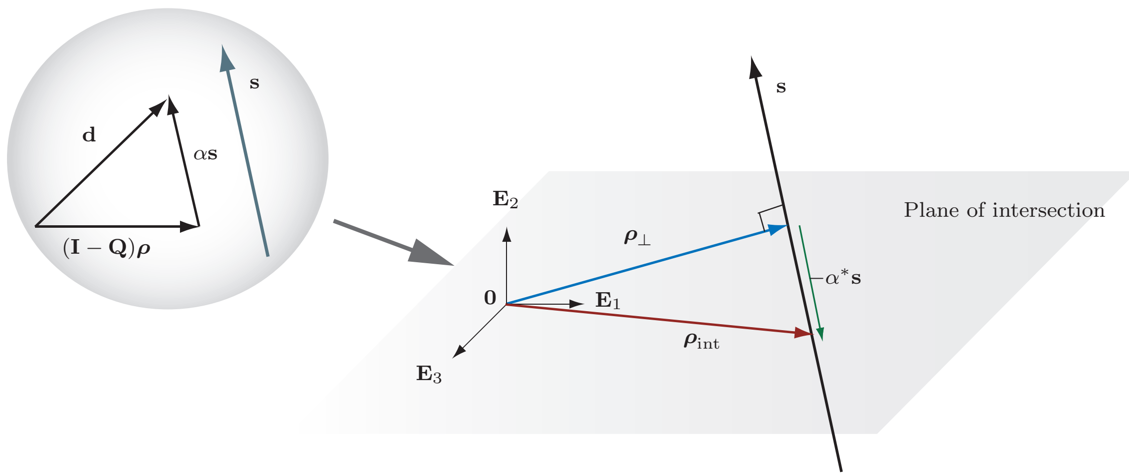

Figure 3.3: The displacement vector (inset) can be written as the sum of the two vectors $(\mathbf{I}-\mathbf{Q})\boldsymbol{\rho}$ and $\alpha\mathbf{s}$. The vector $\boldsymbol{\rho}$ determines the location of the helical axis. There are several ways of defining $\boldsymbol{\rho}$. In this figure, $\boldsymbol{\rho}_\perp$ is the perpendicular distance from from the helical axis to the origin of the coordinate system while $\boldsymbol{\rho}_{\mathrm{int}}$ is the distance from the origin to the point of intersection between HAM and the plane of intersection. Similar to the displacement, one can write $\boldsymbol{\rho}_{\mathrm{int}}$ as the sum, $\boldsymbol{\rho}_{\mathrm{int}} = \boldsymbol{\rho} - \alpha^*\mathbf{s}$. Note that $\alpha^* \neq \alpha$. In the remainder of this paper, we use $\boldsymbol{\rho}$ to denote $\boldsymbol{\rho}_{\mathrm{int}}$ unless otherwise specified.

The Direct Method

The direct method [74] is the most frequently cited paper amongst the spine biomechanics community for determining $\mathbf{s}$, Φ and $\boldsymbol{\rho}$. The original paper was designed to provide a method for describing motion in all six degrees of freedom with reference to the knee joint, which at the time was often simplified as planar motion. A brief summary of the mathematical technique is provided below.

Defining the augmented vectors as

$$\mathbf{A}^* = [1, A_1, A_2, A_3]^T, \qquad \mathbf{a}^* = [1, a_1, a_2, a_3]^T, \tag{3.5}$$

one can write the following relationship,

$$\mathbf{a}^* = \begin{bmatrix} 1 \\ \mathbf{a} \end{bmatrix} = \begin{bmatrix} 1 & \mathbf{0} \\ \mathbf{d} & \mathbf{Q} \end{bmatrix} \begin{bmatrix} 1 \\ \mathbf{A} \end{bmatrix}. \tag{3.6}$$

Given 4 non-coplanar points,

$$\begin{bmatrix} 1 & \mathbf{0} \\ \mathbf{d} & \mathbf{Q} \end{bmatrix} = \begin{bmatrix} \mathbf{a}^{1,*} & \mathbf{a}^{2,*} & \mathbf{a}^{3,*} & \mathbf{a}^{4,*} \end{bmatrix} \begin{bmatrix} \mathbf{A}^{1,*} & \mathbf{A}^{2,*} & \mathbf{A}^{3,*} & \mathbf{A}^{4,*} \end{bmatrix}^{-1}, \tag{3.7}$$

the rotation matrix and displacement can be determined from the submatrices within equation (3.7).

By definition, the axis of rotation $\mathbf{s}$ is not affected by the rotation. Thus, the equation $(\mathbf{Q} - \mathbf{I})\mathbf{s} = \mathbf{0}$ provides three equations for the unknown components of $\mathbf{s}$:

$$\begin{aligned} s_1 &= s_1, \\ s_2 &= \frac{s_1}{(Q_{22}-1)(Q_{33}-1) - Q_{23}Q_{32}} \left(Q_{23}Q_{31} - Q_{21}(Q_{33}-1)\right), \\ s_3 &= \frac{s_1}{(Q_{22}-1)(Q_{33}-1) - Q_{23}Q_{32}} \left(Q_{21}Q_{32} - Q_{31}(Q_{22}-1)\right). \end{aligned} \tag{3.8}$$

The angle of rotation, Φ can then be computed using the identity

$$\Phi = \operatorname{acos}\left(\frac{Q_{11} - s_1^2}{1 - s_1^2}\right). \tag{3.9}$$

Once Φ, $\mathbf{s}$, and the displacement $\mathbf{d}$ are determined, and a plane of intersection is chosen, the following three equations

$$\begin{bmatrix} Q_{11} - 1 & Q_{12} & Q_{13} \\ Q_{21} & Q_{22} - 1 & Q_{23} \\ Q_{31} & Q_{32} & Q_{33} - 1 \end{bmatrix} \begin{bmatrix} \rho_1 \\ \rho_2 \\ \rho_3 \end{bmatrix} = \begin{bmatrix} \alpha s_1 - d_1 \\ \alpha s_2 - d_2 \\ \alpha s_3 - d_3 \end{bmatrix}, \tag{3.10}$$

can be solved for α and the two remaining components of $\boldsymbol{\rho}$. Here, α is the magnitude of the displacement that is parallel to the helical axis.

The SVD Method

The SVD algorithm, initially developed by [9], has been used extensively in the biomechanics community to quantify the kinematics of joints. This method involves minimizing a least squares error criterion given by,

$$r^2 = \frac{1}{2}\sum_{K=1}^{N} \left\| \mathbf{a}^K - (\mathbf{Q}\mathbf{A}^K + \mathbf{d}) \right\|^2. \tag{3.11}$$

Equation (3.11) is then solved for the optimum rotation matrix $\mathbf{Q}$ and displacement vector $\mathbf{d}$ using the SVD method as specified in [141, 146] and [128].

The axis and angle of rotation are then determined using the method described in [131]. Briefly, the axis of rotation is determined from the skew-symmetric part of the rotation matrix, and normalized to give a vector with unit magnitude,

$$\mathbf{s}^{temp} = \begin{bmatrix} Q_{32} - Q_{23} \\ Q_{13} - Q_{31} \\ Q_{21} - Q_{12} \end{bmatrix}, \qquad \mathbf{s} = \frac{\mathbf{s}^{temp}}{\|\mathbf{s}^{temp}\|}, \tag{3.12}$$

The angle of rotation is then determined using the criteria below:

$$\begin{aligned} \Phi &= \operatorname{asin} \left\|\mathbf{s}^{temp}\right\| && \text{if } \left\|\mathbf{s}^{temp}\right\| < 1 \\ \Phi &= \operatorname{acos} \left(\frac{1}{2}\left(\operatorname{tr}(\mathbf{Q}) - 1\right)\right) && \text{if } \left\|\mathbf{s}^{temp}\right\| \geq 1. \end{aligned} \tag{3.13}$$

(If Φ approaches 180°, equations 35 and 36 of [131] are utilized instead. We neglect to include that explanation here since we focused on rotations that were, at most, 45° in magnitude.)

The equation for displacement (3.4) is then used to determine the point of intercept of the helical axis with the plane of interest. For example, if the plane of intersection is given by $y = y_0$, then $\rho_2 = \boldsymbol{\rho} \cdot \mathbf{E}_2 = y_0$ and equation (3.3) can be rewritten as

$$\underbrace{\begin{bmatrix} 1 - Q_{11} & -Q_{13} & s_1 \\ -Q_{21} & -Q_{23} & s_2 \\ -Q_{31} & 1 - Q_{33} & s_3 \end{bmatrix}}_{\boldsymbol{\kappa}} \begin{bmatrix} \rho_1 \\ \rho_3 \\ \alpha \end{bmatrix} = \begin{bmatrix} d_1 + y_0 Q_{12} \\ d_2 + y_0(Q_{22} - 1) \\ d_3 + y_0 Q_{32} \end{bmatrix} \tag{3.14}$$

One can then solve for the components of $\boldsymbol{\rho}$ and α by pre-multiplying both sides of the equation by $\boldsymbol{\kappa}^{-1}$. Note that the direct method utilizes the exact same equations, but determines α and the components of $\boldsymbol{\rho}$ by solving the series of algebraic equations directly.

The Triad Method

The triad algorithm has previously been used in the context of spacecraft dynamics to quantify rigid body motion [121,123] but has not to our knowledge been applied to joint kinematics. It consists of constructing two orthonormal bases using two pairs of vector measurements (the first with components measured in the fixed frame while the components of the second are measured in the rotated frame). Discussions of the triad algorithm and the optimal estimate of the translation can be found in several papers, e.g., [35,123,131]. A thorough explanation of the triad method is given in [41]; here, we provide a brief summary.

Defining $\{\mathbf{V}_1, \mathbf{V}_2, \mathbf{V}_3\}$ and $\{\mathbf{v}_1, \mathbf{v}_2, \mathbf{v}_3\}$ as the orthogonal basis vectors formed from the relative position vectors (produced from a pair of markers) before and after the motion respectively, two orthonormal matrices, $\mathbf{V} = [\mathbf{V}_1, \mathbf{V}_2, \mathbf{V}_3]$ and $\mathbf{v} = [\mathbf{v}_1, \mathbf{v}_2, \mathbf{v}_3]$ are defined and used to calculate the rotation matrix,

$$\mathbf{Q} = \begin{bmatrix} \mathbf{v}_1 & \mathbf{v}_2 & \mathbf{v}_3 \end{bmatrix} \begin{bmatrix} \mathbf{V}_1 & \mathbf{V}_2 & \mathbf{V}_3 \end{bmatrix}^T = \mathbf{v}\mathbf{V}^T. \tag{3.15}$$

The displacement vector is subsequently calculated using the mean position of the markers before and after the motion,

$$\mathbf{d} = \mathbf{a}_{mean} - \mathbf{Q}\mathbf{A}_{mean}, \qquad \mathbf{A}_{mean} = \frac{1}{4}\sum_{K=1}^{4} \mathbf{A}^K, \qquad \mathbf{a}_{mean} = \frac{1}{4}\sum_{K=1}^{4} \mathbf{a}^K. \tag{3.16}$$

Due to the existence of noise in the data, each set of orthonormal basis vectors results in slightly different results, giving 24 possible rotation matrices and their corresponding displacements. For each set of $(\mathbf{Q}.\mathbf{d})$ we seek to minimize the error between the true and calculated positions after the motion,

$$e^2 = \left\| \left[\mathbf{a}^1, \mathbf{a}^2, \mathbf{a}^3, \mathbf{a}^4\right] - \left(\mathbf{Q}\left[\mathbf{A}^1, \mathbf{A}^2, \mathbf{A}^3, \mathbf{A}^4\right] + [\mathbf{d}, \mathbf{d}, \mathbf{d}, \mathbf{d}]\right) \right\|. \tag{3.17}$$

The rotation matrix and corresponding displacement with the smallest error are deemed to be the optimum values ($\mathbf{Q}^{opt}, \mathbf{d}^{opt}$), and used to determine the axis and angle of rotation using the relations

$$\Phi = \text{acos}\left(\frac{1}{2}\left(\text{tr}\left(\mathbf{Q}^{opt}\right) - 1\right)\right) \qquad \mathbf{s} = -\frac{1}{2\sin(\Phi)}\begin{bmatrix} Q_{32}^{opt} - Q_{23}^{opt} \\ Q_{13}^{opt} - Q_{31}^{opt} \\ Q_{21}^{opt} - Q_{12}^{opt} \end{bmatrix}. \tag{3.18}$$

$$\boldsymbol{\rho}_\perp = \frac{1}{2}\left(\mathbf{d}_\perp + \cot\left(\frac{\Phi}{2}\right)\mathbf{s}\times\mathbf{d}\right), \qquad \mathbf{d}_\perp = \mathbf{d} - \alpha\mathbf{s}, \qquad \alpha = \mathbf{d}\cdot\mathbf{s}. \tag{3.19}$$

As the helical axis intersects a plane of interest, the distance from the origin to the point of intersection $\boldsymbol{\rho}$ can be written as the vector sum of $\boldsymbol{\rho}_\perp$ and a vector $\alpha^*\mathbf{s}$ parallel to the helical axis,

$$\boldsymbol{\rho} = \boldsymbol{\rho}_\perp - \alpha^*\mathbf{s}. \tag{3.20}$$

Note that $\alpha^* \neq \alpha$: α is the magnitude of the component of the displacement that is parallel to the helical axis as shown in equation (3.19) while α^* is the magnitude of the translation along the helical axis from the point of intersection of the HAM with the plane of interest to the perpendicular vector from the origin to the HAM (cf. Figure 3.3).

Since we are interested in the interception of $\mathbf{s}$ with the $y = y_0$ plane, we first write $\boldsymbol{\rho} = \boldsymbol{\rho}_\perp - \alpha^*\mathbf{s}$ in component form. The following three equations

$$\begin{aligned} \rho_1 &= \rho_{\perp,1} - \alpha^* s_1 \\ \rho_2 &= \rho_{\perp,2} - \alpha^* s_2 \\ \rho_3 &= \rho_{\perp,2} - \alpha^* s_3, \end{aligned} \tag{3.21}$$

are then combined with

$$\boldsymbol{\rho} \cdot \mathbf{E}_2 = \rho_2 = y_0, \tag{3.22}$$

in equation $(3.21)_2$, to arrive at

$$\alpha^* = \frac{1}{s_2} \left(\rho_{\perp,2} - y_0 \right). \tag{3.23}$$

Equation (3.23) is then inserted into equation $(3.21)_1$ and $(3.21)_3$ to determine the other components of $\boldsymbol{\rho}$. The triad and SVD algorithms for determining $\boldsymbol{\rho}$ are mathematically similar. However, depending on the amount of error in the data and the size of the rotation angle, it may be advantageous to use one method over the other.

3.3 Experimental Methods

This section describes the experimental set-up used to determine the accuracy of the three different computational methods. An outline of the statistical methods used to analyze the data is included. Lastly, a previously-collected set of data from a in vitro biomechanical experiment investigating the anterior-posterior placement of a total disc replacement is described. This data set is used to determine whether the intrinsic errors that arise when calculating the HAM supersede its ability to detect changes before and after instrumentation.

3.3.1 Experimental Data Collection

To simulate typical *in vitro* pure-moment biomechanical studies, a simple hinge-joint mechanical test fixture was mounted to a servo-hydraulic test frame (MTS Bionix 858, MTS, Eden Praire, MN). By using the rotary variable differential transducer of the MTS machine, exact rotations to within one tenth of a degree of motion were capable. Two sets of five 6 mm diameter spherical infrared markers were rigidly attached to the rotating portion of the hinge. Each set of markers consisted of four coplanar markers and one out-of-plane marker. One set of markers were clustered 2.5cm apart, while the second set of markers were spread further apart with 10cm between each marker.

An optical camera system (Optotrak Certus System, Northern Digital Inc., Ontario, Canada) was used to track target motions. The target positions were recorded for 5 seconds at 60 Hz with the jig positioned at $0, 1, 2, 4, 6, 8, 10, 20, 45$ degrees of axial rotation (about the y-axis). Markers were placed at both 7cm and 15cm from the center of rotation (axis of the MTS machine). Five trials were conducted for each rotation to measure the reliability of each HAM algorithm.

The three-dimensional rigid transformation for all rotational positions was processed through a series of MATLAB code that computed the parameters of interest of the HAM using the direct, SVD, and triad algorithms. For the point of intercept three planes perpendicular to the HAM with increasing distance (y=0, y=10mm, and y=100mm) from the origin were investigated to determine changes in accuracy as the distance from HAM increased.

3.3.2 Statistical Analysis

Each of the above methods were processed through MATLAB and the resultant HAM parameters was evaluated using JMP Software (SAS Institute Inc., Cary, NC). Non-parametric and parametric methods were used when appropriate to determine significant differences between the direct, triad and SVD algorithms. In addition, other independent variables including: angle of rotation, co-planar vs. non-coplanar, distance of markers from center of rotation, and marker spread, were investigated to determine whether they make a significant difference in the accuracy and reliability of the respective dependent variable. Typically the absolute difference between a measured value and the actual value were compared which resulted in non-normal distributions. In these cases, the Kruskal-Wallis or Wilcoxon statistical methods were selected. Lastly, as specified in [74], the direct method is not intended for coplanar markers and is therefore not used to compare coplanar vs. non-coplanar markers. For this reason, the direct method was only used to determine the HAM parameters using the non-coplanar set of markers.

3.3.3 Case Study

Motion tracking data from a previous study [102] investigating the fore-aft positioning of a FDA-approved total disc replacement was revisited to calculate the HAM parameters using the most accurate method based on the results of the statistical analysis. This provided information on the relative changes in HAM parameters before and after instrumentation in three different locations (2mm anterior, centered, and 2mm posterior), which were then compared to the intrinsic errors inherent in the calculation to determine whether the HAM is sensitive enough to be used as a comparative tool.

3.4 Results

3.4.1 Rotational Parameters

For each angle of rotation, the calculated angle, Φ, was compared to the actual amount of rotation as read by the MTS machine. Using non-coplanar markers, the direct method was found to be significantly ($p < .001$) less accurate than the other two for all angles with the exception of the 45° rotation. The direct method's overall error had a mean of 0.76° and a maximum error of 4.7°. The triad and SVD methods were not significantly different from each other and had an average and maximum error of (0.07°, .59°) and (0.10°, 1.21°) respectively. The standard deviation among the repeated trials for each angle were consistently below 0.05 for the triad and SVD methods with the 2.5cm spaced markers, and dropped to less than 0.01 when using the 10cm spaced markers. The direct method's standard deviation varied with the angle of rotation and was magnitudes higher than the other two methods, figure 3.4.

The average percent error across all trials decreased as the angle of rotation increased for all three methods, figure 3.5. Statistical differences ($p < .05$) between each angle were determined to find the angle at which the percent error was no longer dependent on the amount of rotation. The direct method displayed a statistical difference between 1° – 2° and 2° – 4°. After 4°, no statistical difference was found in the percent error between any of the angles up to 45°. The triad method displayed a similar cut-off angle of 4°, but differed in that there was no statistical difference between angles 1° and 2°. The SVD method only showed a statistical difference for 1°; all other degrees were not found to be significantly different.

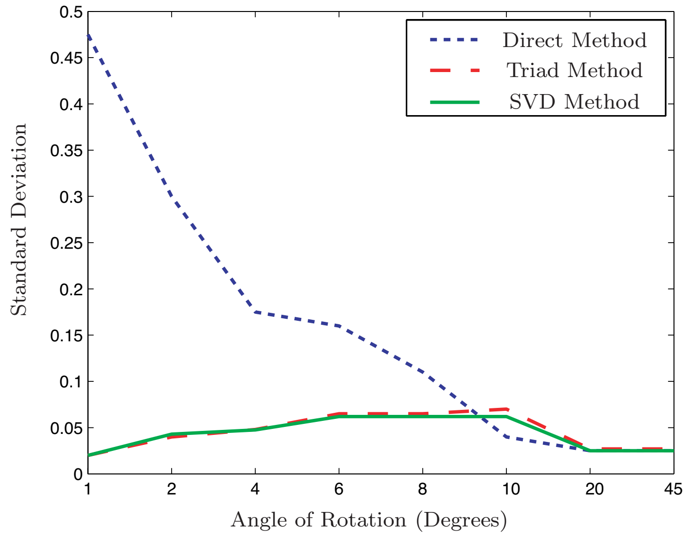

Figure 3.4: Plot of the standard deviation of Φ as a function of the amount of rotation. This standard deviation is for the trials run with the 2.5cm spaced markers located 7cm from the center of rotation.

Marker spacing played a significant role ($p < 0.001$) in the accuracy of the calculated angle favoring markers spaced further apart (in this case, 10cm > 2.5cm). Coplanar markers significantly reduced the accuracy of the triad and SVD data ($p < .001$), with the coplanar markers having an average difference from the true rotation of 0.14° versus the non-coplanar's difference of 0.08°. The distance from the markers to the center of rotation did not significantly affect the ability to accurately measure the amount of rotation.

3.4.2 Directional Parameters

The true axis of rotation is parallel to the axis of the MTS machine which, in this case, coincides with the y-axis in the fixed coordinate system and is located 76.4 mm away

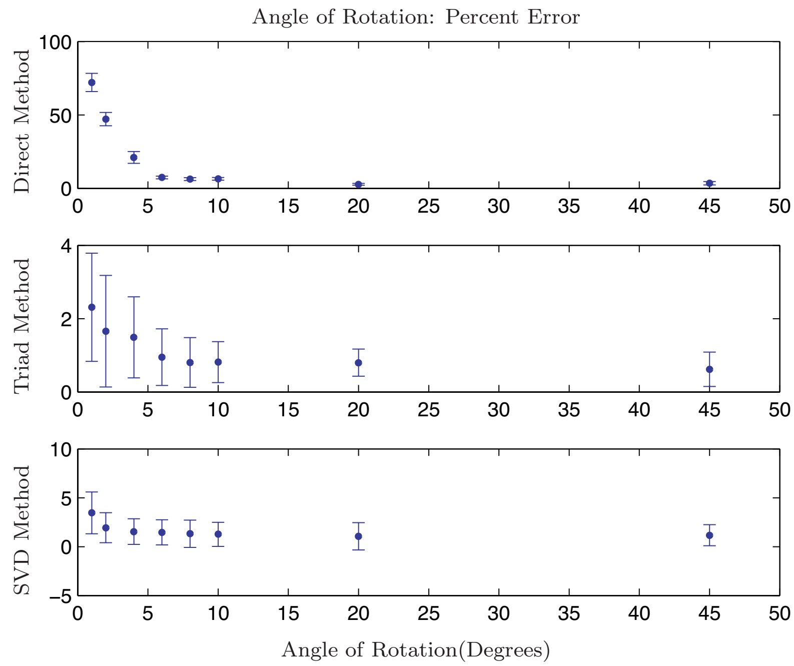

Figure 3.5: Plot of the percent error in calculating the angle of rotation. All three methods show an increase in accuracy as the angle of rotation increases.

from the x-axis of the origin of the coordinate system. The error between this vector and the calculated directional vector, $\mathbf{s}$ is reported as the square root of the sum of the difference of the squares of each vector component, as shown in the equation below:

$$\Delta \mathbf{s} = \sqrt{(s_1 - s_{a1})^2 + (s_2 - s_{a2})^2 + (s_3 - s_{a3})^2}. \tag{3.24}$$

Here $\Delta \mathbf{s}$ is the reported error, and $\mathbf{s}_a = \mathbf{E}_2$ is the true axis of rotation. Visually, this is the distance between the tips of the two vectors. If they are parallel the error is zero; as they deviate the value increases approaching a maximum of 2 when they are antiparallel. Similarly, the standard deviation is reported as the square root of the sum of the difference of the squares of the standard deviation of each vector component,

$$\Delta \mathbf{s_{sd}} = \sqrt{\sum_{i=1}^{3} \left(\sigma(s_i) - \sigma(s_{a,i})\right)^2} \tag{3.25}$$

where σ stands for standard deviation. Using this approach, the direct method was determined to be significantly less accurate with an average $\Delta\mathbf{s}$ of 0.36 among all non-coplanar trials, figure 3.6. The triad and SVD methods were not significantly different using non-coplanar markers, with average errors of 0.025 and 0.015 respectively. When comparing these two methods using all data sets (coplanar and non-coplanar combined) the coplanar triad data values of $\Delta\mathbf{s}$ were significantly higher than the non-coplanar triad values and all the SVD errors combined.

The standard deviation $\Delta\mathbf{s_{sd}}$ of the axis of rotation for each data set (fixed angle, marker spacing and distance to the center of rotation) was consistently less than 0.015 for both the triad and SVD methods across all angles. The direct method varied with each angle similar to the standard deviation seen when calculating the angle of rotation (see figure 3.4), ranging from a maximum of 1.01 at 1° of rotation with the 2.5cm markers 7cm from the center of rotation, to a minimum $\Delta\mathbf{s_{sd}}$ of 0.0016 at 45° of rotation with the same marker spacing and location.

All other independent variables played a significant role ($p < 0.001$) in the accuracy of the axis of rotation. The 10cm-spaced markers were more accurate than the 2.5cm-spaced markers and were even more accurate when placed 7cm from the axis of rotation compared to 15cm. Coplanar markers were less accurate than non-coplanar markers for both the triad and SVD methods.

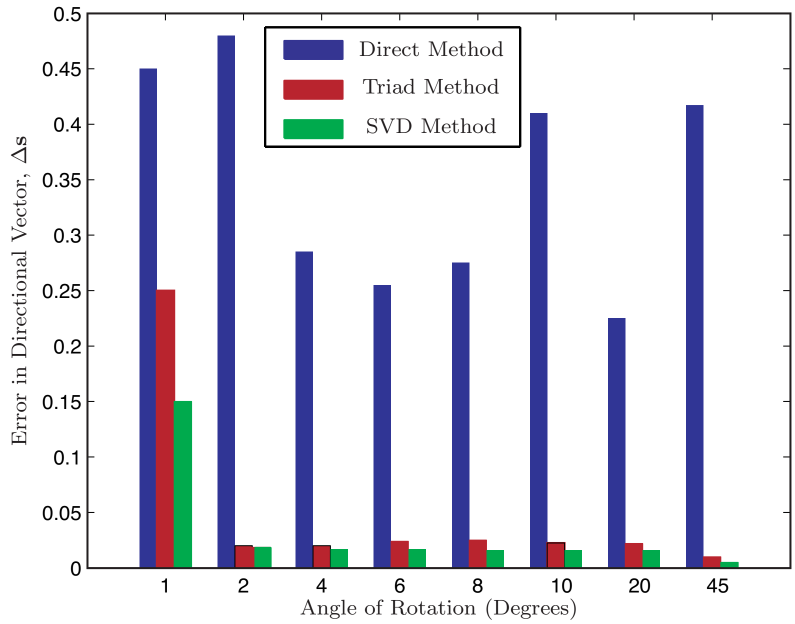

Figure 3.6: The error, $\Delta\mathbf{s}$, in calculating the directional vector of the helical axis of motion for the direct, triad, and SVD methods. (This data is for non-coplanar points only, to accommodate the direct method.)

3.4.3 Location Parameters

The point of intercept, $\boldsymbol{\rho}$, was calculated for three different planes parallel to the $x-z$ plane and perpendicular to the HAM: $y = 0$mm, $y = 10$mm, and $y = 100$mm. The error is reported as the distance,$\Delta\boldsymbol{\rho}$, between the calculated point of intercept and the true location as defined by the center of the MTS actuator. Depending on the plane of intersect, different methods were determined to be statistically more accurate ($p < 0.001$) than others, table 3.2. When determining $\boldsymbol{\rho}$ at $y = 0$mm and $y = 10$mm, the direct method was most accurate, whereas the SVD method calculated the intercept most accurately at $y =$

Average Error: Point of Intercept			
Method	$y = 0$	$y = 10$	$y = 100$
Direct	**1.9**	**1.7**	2.7
Triad	2.9	3.0	3.8
SVD	3.4	3.3	**2.0**

Table 3.2: Average error (in mm) when calculating the location of the helical axis as defined as a point of intercept with three different planes of interest: $y = 0$, $y = 10$, and $y = 100$. Bold type indicates the most accurate algorithm for each plane.

100mm. The error generally decreased for all methods as the amount of rotation increased, although only the triad and direct methods exhibited statistical differences between the angles. The accuracy of the direct method increased after 4°. The triad method did not become statistically more accurate until 45° of rotation.

Again, all independent variables played a significant role ($p < 0.001$) in determining the accuracy of calculating $\boldsymbol{\rho}$ with the 10cm-spaced markers placed 7cm from the axis of rotation producing the most accurate results. As with the previous two parameters, coplanar markers were less accurate than non-coplanar markers for both the triad and SVD methods.

3.4.4 Case Study

With the results of the above statistical analysis, we devised a 'hybrid method' which combines the SVD method for calculating rotation matrix, angle and axis of rotation, and the direct method for calculating the displacement $\mathbf{d}$, and point of intercept with a specific anatomical plane $\boldsymbol{\rho}$. This new method was then applied to motion tracking data for $0°$ to $6°$ of flexion, extension, and lateral bending for a single specimen with the disc intact followed by the implantation of a TDR in three different anterior-posterior positions. Since the helical axis is typically represented graphically by displaying the orientation of the helical axis vector and its intersection with specific anatomical planes, these two parameters were the focus of this case study.

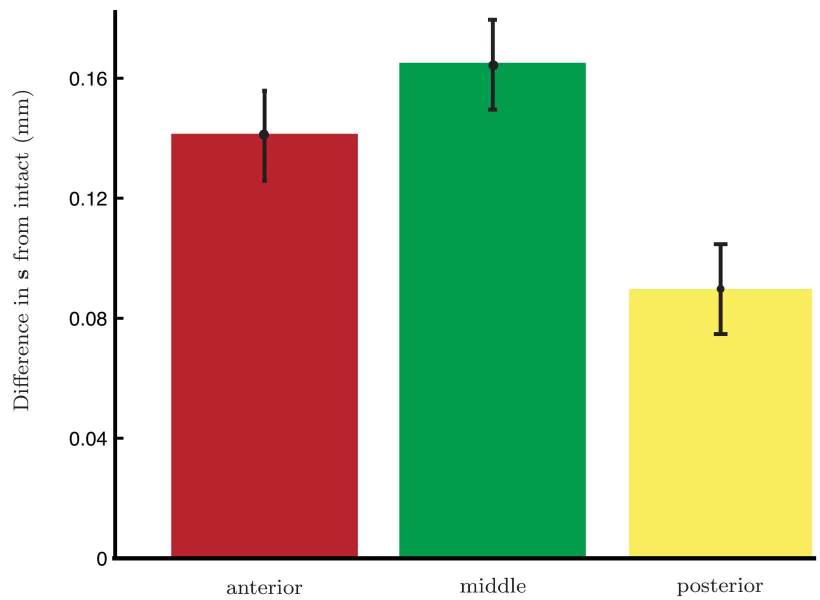

Figure 3.7: Difference between the directional vector for instrumented segment and that of the intact disc calculated as the square root of the sum of the difference of squares (cf. equation 3.24). Error bars are the calculated error ($\Delta\mathbf{s} = 0.015$) associated with $\mathbf{s}$ at $6°$ of rotation using the hybrid method.

Computation of the directional vector $\mathbf{s}$, between the instrumented and un-instrumented disc revealed that the intact disc experienced more coupled motion, evident by an increase in the obliquity of the vector. The directional vector for the intact case was then compared to each device placement case using equation 3.24. Figure 3.7 graphically shows this comparison for 6 degrees of right lateral bending. The error associated with using the hybrid method for 6° of rotation (see figure 3.6) is indicated by the error bars ($\Delta\mathbf{s} = 0.015$) revealing a measurable difference between each device placement case and the intact case, as well as between the posterior position and the anterior and middle placement of the device. Using the direct method with its associated error of 0.25, these differences would not be distinguishable as the error exceeds any of differences between the intact and three device cases.

Calculating the point of intercept using the hybrid method resulted in a wide range of results between the intact, anterior, posterior, and centered device, with differences anywhere between 1mm and 10mm. Figure 3.8 displays the point of intercept for 0° to 6° of right lateral bending determined for the four different device placement cases. The circles around each data point indicate the error associated with each point. Using the hybrid method, the error is 2mm, compared to 3.5mm with the SVD method. The greater error associated with the SVD method obscures the ability to detect changes in the point of intercept between the four different cases.

3.5 Discussion

The helical axis of motion has been used to analyze the 6-dimensional motion of the spine for several decades and is becoming a popular metric for evaluating non-fusion implants. When used in this manner, it is important that the calculated errors in the reported HAM parameters do not exceed the magnitude of change produced by the implanted

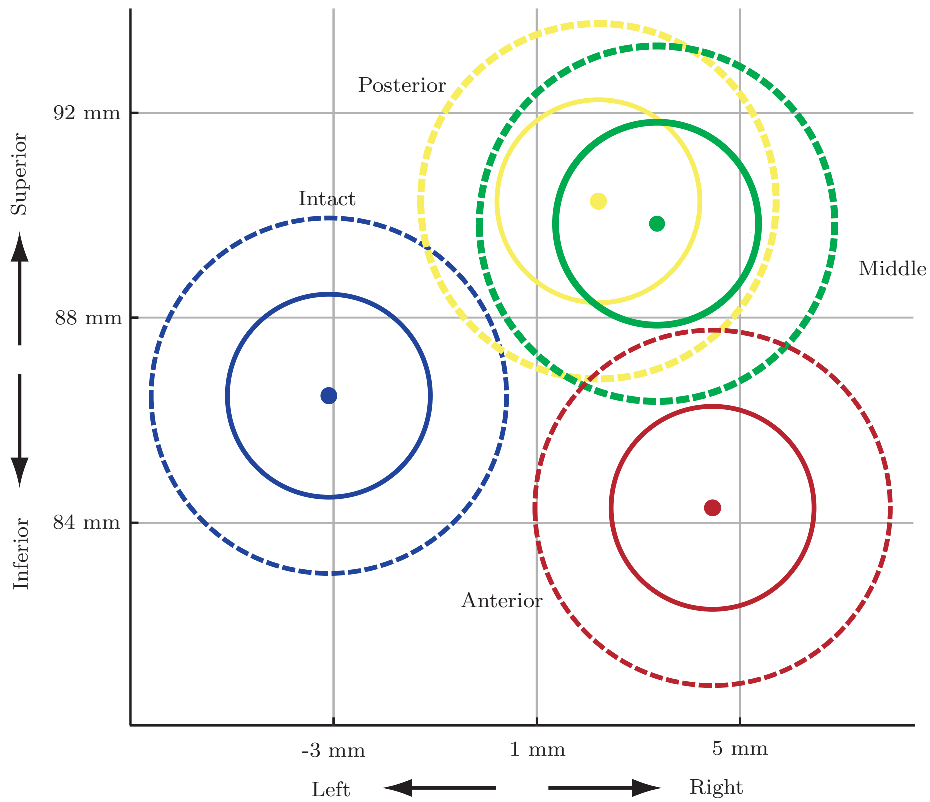

Figure 3.8: Location of the intersection with the mid-coronal plane during 6° of right lateral bending. The solid circle around each point indicates the 2mm error associated with calculating $\boldsymbol{\rho}$ at 6° of rotation using the hybrid method, where the dotted circle shows the 3.5mm error associated with the SVD method. The greater amount of error seen with the SVD method creates more overlap between the four points of intercept, making the anterior and intact no longer distinguishable from the posterior placement.

device. Therefore, the purpose of this paper was to investigate the accuracy and reliability of calculating the HAM in the context of a typical pure-moment *in vitro* biomechanical experiment. Different variables were explored, including choice of algorithm and marker design, to determine the optimal combination.

The results of this study indicate that variables within the design of the experiment can play an important role in increasing the accuracy of the HAM. Using non-coplanar markers that were placed further apart proved to increase the accuracy of the angle, axis, and location of the helical axis of motion, in agreement with the results of [30, 129, 141, 146]. Additionally, increasing the distance of the markers from the center of rotation (i.e., further from the specimen) produced more precise measures of the direction and location of the HAM in consensus with the analysis in [146] (further validated by [30, 54, 130] and mathematically analyzed in [128, 129]).

A comparison of the direct, triad, and SVD methods revealed that no one method was the optimum choice for calculating all three HAM parameters. The triad and SVD methods both performed better when calculating the angle Φ, and direction of the helical axis of motion $\mathbf{s}$ while the direct method was consistently more accurate at determining the point of intercept $\boldsymbol{\rho}$. As expected, increasing the angle of rotation reduced the error associated with determining Φ and $\mathbf{s}$ for all three algorithms. However, only the accuracy of the direct method in calculating $\boldsymbol{\rho}$ increased as Φ increased, in contrast with the theoretical error estimated published in [146]. We suspect that the relative inaccuracy of the SVD algorithm for determining $\boldsymbol{\rho}$ is due to the fact that the least square error equation (cf. equation 3.11) is optimized for data with isotropic noise, which is hard to achieve in spinal testing. Furthermore, both methods mentioned are orders of magnitude more complex than the direct method and thus more susceptible to numerical error propagation.

Based on this comparison, a 'hybrid' method consisting of a combination of the SVD and direct methods was constructed and used to convert motion tracking data into HAM parameters. This method has the additional advantage of being a composition of the two most commonly used algorithms in determining HAM parameters thus rendering the algorithm slightly more usable than other existing novel algorithms out there that have yet to gain traction. [2]

It was shown, vis-á-vis a case study investigating the anterior-posterior placement of a total disc replacement, that the HAM is sufficiently sensitive to be used as a kinematic metric, provided it is calculated using the hybrid method, and the recommended experimental techniques suggested previously are followed. Failing this, it is possible that HAM errors will supersede the ability to detect changes before and after various surgical alterations making any interpretation of these result misleading.

3.6 Conclusion

In conclusion, the helical axis of motion can be a reliable tool to accurately convert motion tracking data from various motion preserving devices into parameters that characterize their six-dimensional behavior. However, because the algorithms used to calculate HAM are highly non-linear and can amplify errors if not chosen carefully, it is important to choose experimental and computational methods which generate repeatable and consistent

[2] The associated MATLAB code can be found at http://www.me.berkeley.edu/spine/.

information. Errors in the HAM parameters were found to decrease when the markers were

1. placed closer to the HAM.

2. non-coplanar.

3. spaced further apart from each other.

Additionally, the hybrid method, consisting of of a combination of the SVD algorithm for determining the axis and angle of rotation, and the direct method for determining the displacement and point of intercept of the HAM with a plane of interest, was devised and resulted in the least amount of experimental error compared to the other three algorithms analyzed here.

Chapter 4

On the Stiffness Matrix of the Intervertebral Joint: Application to Total Disc Replacement

4.1 Introduction

While there are hopes of seeing vertebral disc replacement travel the same successful path as total hip and knee replacements, the complexity of the joint structure between pairs of vertebrae has caused unforeseen complications (see [10, 26, 29, 114] and references therein) The intervertebral disc has a complex structure and function that includes synergistic functioning with the facets in constraining motion and supporting load. These structural complexities obscure optimal design choices since the relative motion of vertebra is non-trivial to characterize and measure. More importantly, inappropriate modifications to this motion may lead to other problems such as osteoarthritis in the facet joints and motion segment instability, which may lead to impingement of neural structures [110]. Spine mechanics are further complicated by a loading regime that consists of bending moments and loads that are multi-directional and often coupled.

A wide-range of measurements are currently being used to characterize spinal movements within the orthopaedic research community, including: range of motion (see, e.g., [86]), disc pressure (see, e.g., [27]), neutral zone [108], helical axis of motion (see, e.g., [83,130]), vertebral strain (see, e.g., [3]), facet forces (see, e.g., [117,119]), and stiffness (see, e.g., [109]). Collectively this has provided a vast amount of information on the motion of the spine. Much of this data is crucial in the design and development of effective total disc replacements (TDR). Of particular interest in this paper is an examination of the stiffness changes induced by a TDR.

To examine the stiffness changes induced by a TDR, one is first lead to the seminal paper by Panjabi et al. [109] which was published in 1976. In [109], a stiffness matrix characterizing a six degree-of-freedom vertebral motion segment in the thoracic spine was proposed. Using symmetry arguments, restricting attention to infinitesimal rotations, and assuming certain symmetries, the number of stiffnesses in this matrix were reduced from 36 to 12. Subsequent work by Gardner-Morse, Stokes et al. [51, 52, 135, 136], have measured these 12 parameters. A related stiffness matrix for the lumbar spine was proposed by McGill and Norman [89], and in subsequent works the potential energy of the muscle forces and external forces was incorporated into this matrix (see Cholewicki and Norman [19], Howarth et al. [67], McGill and Bennett [90], and references cited therein).

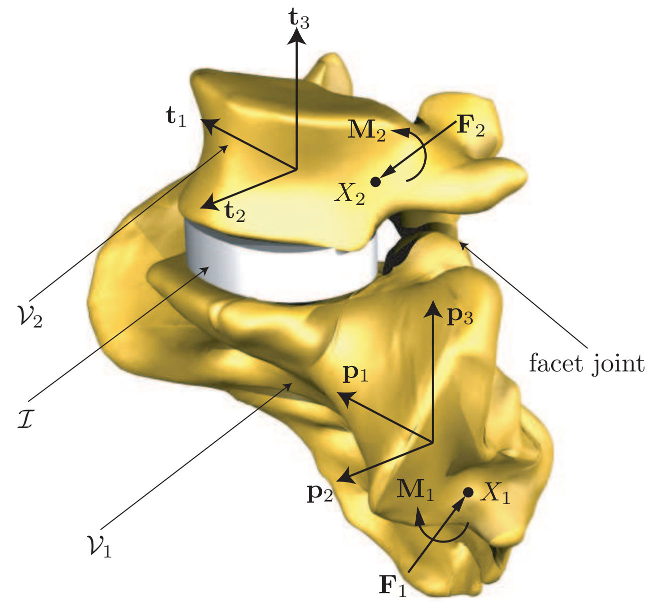

Figure 4.1: Schematic of a motion segment consisting of a pair of vertebral bodies $\mathcal{V}_1$ and $\mathcal{V}_2$ and the intervertebral disc $\mathcal{I}$. One of the pair of facet joints is also indicated, as are the bases $\{\mathbf{p}_1, \mathbf{p}_2, \mathbf{p}_3\}$ for $\mathcal{V}_1$ and $\{\mathbf{t}_1, \mathbf{t}_2, \mathbf{t}_3\}$ for $\mathcal{V}_2$.

Unfortunately, the stiffness matrices proposed by Panjabi et al. [109] and McGill and Norman [89] have several restrictions which limit their utility. The most problematic is the inability to accommodate finite rotations and energy losses due to the poro-viscoelastic nature of the intervertebral disc and the nonconservative forces and moments due to the facet joints and ligaments. These and other deficiencies are addressed in this paper by presenting an alternative method of calculating the stiffness matrix of a motion segment. The segment in question consists of two vertebral bodies, their adjoining intervertebral disc, the facet joints, and the ligaments connecting the two bodies. The construction of the stiffness matrix is performed with the help of the developments in O'Reilly [100] and O'Reilly and Srinivasa [103], and by exploiting a recently developed basis which is known as the dual Euler basis. The methodology is valid for finite rotations and can accommodate the (non-conservative) forces and moments due to the facet joints and ligaments. Thus, the matrix proposed in this paper will be non-symmetric due to the nonconservative forces that are included in the model.

The use of the dual Euler basis in the present paper is similar to the use of a related dual basis in Howard et al. [66] and Žefran and Kumar [142] which recently came to the attention of the authors. As noted in [66, 100, 101, 142], dual bases are very useful in establishing compact representations for conservative moments and wrenches. In the pair of papers [66, 142], Žefran et al. use screw theory to describe the wrench (force and moment) components with respect to a dual basis and use these components to establish a stiffness-twist relationship. Their basis couples the individual components of the twists (displacements and rotations), and their work could also be used to formulate a stiffness matrix for the motion segment.

The primary aim of the present paper is to introduce the theory which supports this new formulation of the stiffness matrix. Secondly, a method for distilling the 36-component matrix into a single scalar for statistical purposes is presented. The third and final aim is to demonstrate the value of both the stiffness matrix and its respective scalar by applying them experimentally to characterize the kinetics of a TDR. In particular, these metrics are used to evaluate the sagittal placement of the SYNTHES PRODISC-L TDR system and compare it to an intact vertebral disc. The results presented in this paper are the first such characterization of a TDR system.

An outline of the paper is as follows. In the following section, the parameterization of the displacement and relative rotation of a pair of vertebra is discussed. In the interests of conciseness, many of the details on the parameterization are placed in Appendix A. Section 2 contains a presentation of the stiffness matrix of a motion segment and a discussion of several of its unusual features. Most of the details on the derivation of this stiffness matrix are presented in Appendix B. A discussion of the kinetics of a motion segment follows. The application of the stiffness matrix K to the characterization of a TDR forms the primary focus of Section 3. In particular, the experimental measurements of K for an intact disc and three distinct placements of a TDR are presents. The paper closes with discussions of the objectives of the paper and how they were achieved, and the directions of future research on K. For the readers' convenience a section on nomenclature follows Section 4.4.

4.2 Theory

A motion segment consists of two vertebral bodies, an intervertebral disc, a pair of facet joints and the muscles and ligaments connecting the vertebra (cf. Fig. 4.1). The relative motion of the discs can be characterized by a set of three displacements and three Euler angles. The stiffness matrix K relates a set of forces and moments to the three displacements and three angles.

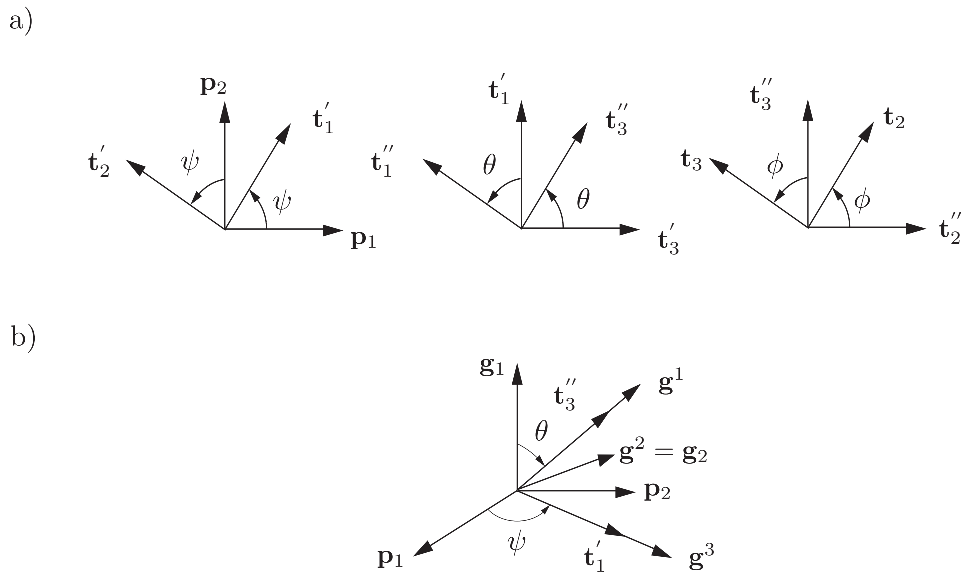

Figure 4.2: Schematic of the 3-2-1 set of Euler angles: ψ, θ, and ϕ. In this figure, the vectors $\mathbf{g}_1 = \mathbf{p}_3$, $\mathbf{g}_2 = \mathbf{t}_2^{'} = \cos(\psi)\mathbf{p}_2 - \sin(\psi)\mathbf{p}_1$, and $\mathbf{g}_3 = \mathbf{t}_1^{''} = \cos(\theta)\mathbf{t}_1^{'} + \sin(\theta)\mathbf{p}_3$ form the Euler basis. As illustrated in b), the dual Euler basis $\left\{\mathbf{g}^1, \mathbf{g}^2, \mathbf{g}^3\right\}$ is distinct from the Euler basis.

4.2.1 Kinematics

The three-dimensional displacement vector $\mathbf{y}$ is defined by the relative motion of two points X_1 and X_2, one on each vertebra. Although the selection of these points is arbitrary, their selection will effect the stiffness matrix. To define the Euler angles a pair of right-handed orthonormal bases is needed. One of these basis, which is denoted by $\{\mathbf{p}_1, \mathbf{p}_2, \mathbf{p}_3\}$ is fixed to the lower vertebra, and the other, which is denoted by $\{\mathbf{t}_1, \mathbf{t}_2, \mathbf{t}_3\}$ is affixed to the upper vertebra. An example featuring the L5/S1 motion segment is shown in Fig. 4.1.

In studies on the kinematics of the spine, it is standard to refer to the angles as axial rotation (ψ), lateral bending (θ), and flexion-extension (ϕ). Referring to Fig. 4.2(a), the axial rotation represents a rotation about $\mathbf{p}_3$ through an angle ψ. This is followed by a lateral bending about $\mathbf{t}_2^{'} = \cos(\psi)\,\mathbf{p}_1 + \sin(\psi)\,\mathbf{p}_2$. The final angle of rotation is a flexion-extension ϕ about $\mathbf{t}_1$. The axes of rotation $\mathbf{p}_3, \mathbf{t}_2^{'}$, and $\mathbf{t}_1$ define the Euler basis:

$$\begin{bmatrix} \mathbf{g}_1 \\ \mathbf{g}_2 \\ \mathbf{g}_3 \end{bmatrix} = \begin{bmatrix} \mathbf{p}_3 \\ \mathbf{t}_2^{'} \\ \mathbf{t}_1 \end{bmatrix} = \begin{bmatrix} 0 & 0 & 1 \\ -\sin(\psi) & \cos(\psi) & 0 \\ \cos(\theta)\cos(\psi) & \cos(\theta)\sin(\psi) & -\sin(\theta) \end{bmatrix} \begin{bmatrix} \mathbf{p}_1 \\ \mathbf{p}_2 \\ \mathbf{p}_3 \end{bmatrix}. \tag{4.1}$$

Based on the choice of axes, the set of Euler angles used here is known as the 3-2-1 set, and, as discussed by Crawford et al. [21], this is the optimal choice of Euler angles for the motion segment. Further details on the Euler angles used in this paper, the Euler basis and the dual Euler basis can be found in Appendix A.

4.2.2 The Stiffness Matrix K

To define the stiffness matrix K, one presumes that one can measure the resultant force and moment on one of the vertebra. For the upper vertebra, the resultant force is denoted by $\mathbf{F}_2$ and the resultant moment, relative to X_2, is denoted by $\mathbf{M}_2$. Correspondingly, the resultant force on the lower vertebra is denoted by $\mathbf{F}_1$ and the resultant moment, relative to X_1, is denoted by $\mathbf{M}_1$. When one measures these forces and moments and then correlates them to the displacements $\mathbf{y}$ and relative rotations ψ, θ, and ϕ, the forces and moments when the displacements and relative rotations are zero will not necessarily vanish. These residual forces and moments are denoted by a subscript 0. The stiffness matrix is then defined by the relationship

$$\mathsf{F} = \mathsf{F}_0 - \mathsf{K}\mathsf{d}. \tag{4.2}$$

In Eq. (4.2), the generalized force vector F, the generalized residual force vector F_0, the generalized displacement vector d, and stiffness matrix K are

$$\mathsf{F} = \begin{bmatrix} \mathbf{F}_2 \cdot \mathbf{p}_1 \\ \mathbf{F}_2 \cdot \mathbf{p}_2 \\ \mathbf{F}_2 \cdot \mathbf{p}_3 \\ \mathbf{M}_2 \cdot \mathbf{g}_1 \\ \mathbf{M}_2 \cdot \mathbf{g}_2 \\ \mathbf{M}_2 \cdot \mathbf{g}_3 \end{bmatrix}, \quad \mathsf{F}_0 = \begin{bmatrix} \mathbf{F}_{20} \cdot \mathbf{p}_1 \\ \mathbf{F}_{20} \cdot \mathbf{p}_2 \\ \mathbf{F}_{20} \cdot \mathbf{p}_3 \\ \mathbf{M}_{20} \cdot \mathbf{g}_1 \\ \mathbf{M}_{20} \cdot \mathbf{g}_2 \\ \mathbf{M}_{20} \cdot \mathbf{g}_3 \end{bmatrix}, \quad \mathsf{d} = \begin{bmatrix} \mathbf{y} \cdot \mathbf{p}_1 \\ \mathbf{y} \cdot \mathbf{p}_2 \\ \mathbf{y} \cdot \mathbf{p}_3 \\ \psi \\ \theta \\ \phi \end{bmatrix}, \quad \mathsf{K} = \begin{bmatrix} k_{11} & \cdots & k_{16} \\ \vdots & \ddots & \vdots \\ k_{61} & \cdots & k_{66} \end{bmatrix}. \tag{4.3}$$

The residual force $\mathbf{F}_{20}$ and residual moment $\mathbf{M}_{20}$ are the respective values of $\mathbf{F}_2$ and $\mathbf{M}_2$ when the displacement $\mathsf{d} = \mathsf{0}$.

There are several unusual features in Eq. (4.2). First, as shown in Eqs. (C.13) and (C.17) of Appendix C.3, the forces $\mathbf{F}_1$ and $\mathbf{F}_2$ are equal and opposite, as are the moments $\mathbf{M}_1$ and $\mathbf{M}_2$:

$$\mathbf{F}_1 = -\mathbf{F}_2, \qquad \mathbf{M}_1 = -\mathbf{M}_2. \tag{4.4}$$

Second, it is necessary to compute the components $\mathbf{M}_2 \cdot \mathbf{g}_k$, and as the Euler basis vectors $\mathbf{g}_k$ depend on the Euler angles θ and ψ these components are often not intuitive. Indeed, as discussed in Appendix C, computing $\mathbf{M}_2 \cdot \mathbf{g}_k$ is equivalent to expressing $\mathbf{M}_2$ in terms of it components relative to the dual Euler basis $\{\mathbf{g}^1, \mathbf{g}^2, \mathbf{g}^3\}$.

In comparison to the stiffness matrix presented by Panjabi et al. [109], it is unrealistic to expect that K will be symmetric: It is well-known in structural dynamics that the presence of nonconservative forces and moments can destroy the symmetry of the stiffness matrix. However, if attention is restricted to infinitesimal rotations, and the symmetry restrictions of Panjabi et al. are imposed, then K will simplify to the stiffness matrix proposed in [109]. The precise details on this equivalence can be found in Appendix B.1 The moment components determined by Panjabi et al.'s stiffness matrix correspond to $\mathbf{M} \cdot \mathbf{p}_k$. Unfortunately, it has long been known [100] that a constant moment $M_0\mathbf{p}_3$, where M_0 is a constant, is nonconservative when finite rotations are present. However, the moment $M_0\mathbf{g}^1$ is conservative. The use of the components $\mathbf{M}_2 \cdot \mathbf{g}_k$ in (4.3) are precisely to ensure that when K is symmetric, then $\mathbf{F}_2 - \mathbf{F}_{20}$ and $\mathbf{M}_2 - \mathbf{M}_{20}$ are guaranteed to be conservative even in the presence of finite rotations.

4.2.3 An Aggregate Stiffness Ratio

Comparison of the stiffness matrices for two motion segments on a term by term basis is difficult and often not very illuminating. An alternative strategy, which is proposed here, is to define a aggregate stiffness to be the norm of the stiffness matrix:

$$k = \sqrt{\mathrm{tr}\left(\mathsf{K}\mathsf{K}^T\right)}, \tag{4.5}$$

where tr denotes the trace of a matrix. To compare the aggregate stiffness of two motion segments, one can then define a normalized value S:

$$S = \frac{k_{\mathrm{I}} - k_{\mathrm{II}}}{k_{\mathrm{I}}}, \tag{4.6}$$

where k_{I} and k_{II} are the aggregate stiffnesses associated with the respective stiffness matrices of the two motion segments. The aggregate stiffness ratio S is distinct from the stability indices discussed in Howarth et al. [67]. Indeed, as one cannot expect the stiffness matrices to be symmetric or positive definite, such stability indices may not be revealing.

4.3 Stiffness Alterations due to Total Disc Replacements

To demonstrate the utility of the stiffness matrix presented in this paper, the present section details its application to a data set that has recently been collected to determine the sensitivity of TDR placement along the saggital plane.

4.3.1 Experimental Protocol

Specimen Preparation

Healthy, non-degenerate fresh-frozen L5/S1 motion segments were harvested from human spines (n=5, mean age: 44, three females and two males). Specimen preparation included meticulous removal of muscular tissue so as to retain the integrity of the capsular and ligamentous elements. Afterwards, the specimens were potted in polymethylmetacrylate (PMMA), so that the S1 end-plate was parallel to the PMMA surface and clamping faces.

Mechanical Testing

Each specimen was placed in a servo-hydraulic apparatus (Bionix 858, MTS Systems Corp. Eden Meadow, MN) such that the disc was oriented at 40° relative to the horizontal axis (Fig. 4.3) as described previously in Rousseau et al. [117, 118]. The specimens were loaded with 850 N generating 650 N of disc compression and 550 N of horizontal shear consistent with free body analyses of L5/S1 based on specific morphometric studies (see, [2, 37, 89, 92, 144]). Wedges were added at the frictionless interface to impose 3° and 6° of flexion, extension, and lateral bending postures, while axial torsion was unconstrained.

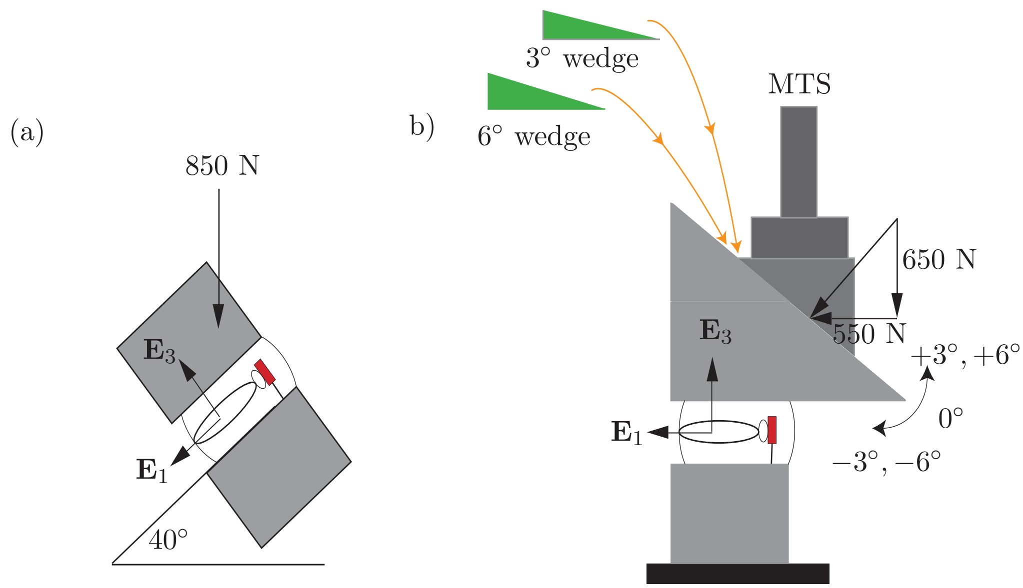

Figure 4.3: Schematic diagram of experimental set-up: 40° sacral slope and 850 N load in standing position: (a), Testing device constrained L5 posture in flexion, extension, and bending for investigating L5/S1 kinematics and (b), load is uniformly distributed and applies both shear of 550 N and compression of 650 N. In (b), the 3° and 6° wedges which are used to achieve the desired relative motion of the vertebrae are also shown.

The 12° total range of motion in the sagittal and the frontal plane was below the normal physiological zone of the L5/S1 joint [110].

Once tested with the disc intact, a TDR was performed (ProDisc-L, Synthes Inc. West Chester, PA USA). This particular device has a polyethylene (UHMWPE) on metal (CoCrMo) bearing interface with a non-retentive ball-and-socket design allowing 3 degrees-of-freedom. The device was initially positioned 3 mm (±0.5 mm) posterior to the center of the inferior (S1) endplate. The specimen was tested in this position, and the device was then moved forward 3 mm to the central location and tested, followed by 3 mm anterior.

This enabled measurement of the sensitivity of device placement along the sagittal plane.

Specimen preconditioning consisted of three cycles of complete loading and unloading prior to testing in each posture and was reduced to one cycle when the specimen was instrumented. During testing, data were collected after one minute of loading for each posture. Tissues were kept moist during testing by wrapping in saline-soaked gauze. A three-camera optoelectronic system (Motion Analysis Corpl, Santa Rosa, CA) was used to track the motion between the two vertebral bodies, while a load cell rigidly attached to S1 simultaneously recorded the resultant force and moments.

4.3.2 Data Analysis

Kinematic data was computed using software that integrated data from the load cell and motion analysis files. An optimization algorithm was applied to the optical targets between neutral (no wedge) and each of the rotated postures to get the optimal estimates of the Euler angles and the translation of a marker on L5 for each motion. In this manner, the six components necessary to resolve the displacement vector d for each motion were determined. The algorithm used is based on the TRIAD algorithm and a classical optimal estimate of the translation. Discussions of these optimal estimates can be found in several papers, e.g., Dorst [35], Shuster and Oh [123], Spoor et al. [130, 131], and Woltring et al. [146].

Load cell data for each motion was translated into the six components of the generalized force vector F. The difference between rotated postures and the neutral posture were determined to give relative forces and moments. These vectors were then transformed to the dual Euler basis as described in the two earlier sections to allow accurate calculations despite the relatively large angles of rotation. The result is a six component vector $\mathsf{F} - \mathsf{F}_0$ consisting of three forces components and three moment components.

The displacement and load vectors for the rotations were organized into 6-by-6 matrices, d_E and F_E respectively, where each column represents a different motion, indicated by $m_1, \ldots, m_6$:

$$\mathsf{d}_E = \left[\begin{array}{ccc} \{\mathsf{d}\}_{m_1} & \cdots & \{\mathsf{d}\}_{m_6} \end{array}\right], \qquad \mathsf{F}_E = \left[\begin{array}{ccc} \{\mathsf{F} - \mathsf{F}_0\}_{m_1} & \cdots & \{\mathsf{F} - \mathsf{F}_0\}_{m_6} \end{array}\right]. \tag{4.7}$$

To compute the stiffness matrix K, one then computes $\mathsf{F}_E \left(\mathsf{d}_E\right)^{-1}$. The resulting matrix is composed of 36 stiffness coefficients relative to a neutral posture.

To analyze the TDRs influence on the stiffness matrix K of the motion segment, the stiffness matrix of the intact disc is compared to the corresponding matrix of the motion segment after the implantation of the TDR. The former and latter matrices are labeled by K_{I}, and K_{T}, respectively. Following Eq. (4.6), the stiffness ratio S was then computed:

$$S = \frac{k_{\mathrm{T}} - k_{\mathrm{I}}}{k_{\mathrm{I}}}, \tag{4.8}$$

where $k_{\mathrm{T,I}}$ are the aggregate stiffnesses associated with the matrices $\mathsf{K}_{\mathrm{T,I}}$.

4.3.3 Results

The four resultant stiffness matrices (intact and three device placements) varied considerably from specimen to specimen. In the interests of brevity, the outcomes are demonstrated with the stiffness matrices for a single representative specimen, and the aggregate stiffness ratio S is relied upon for interpreting general changes between device positions among the five motion segments.

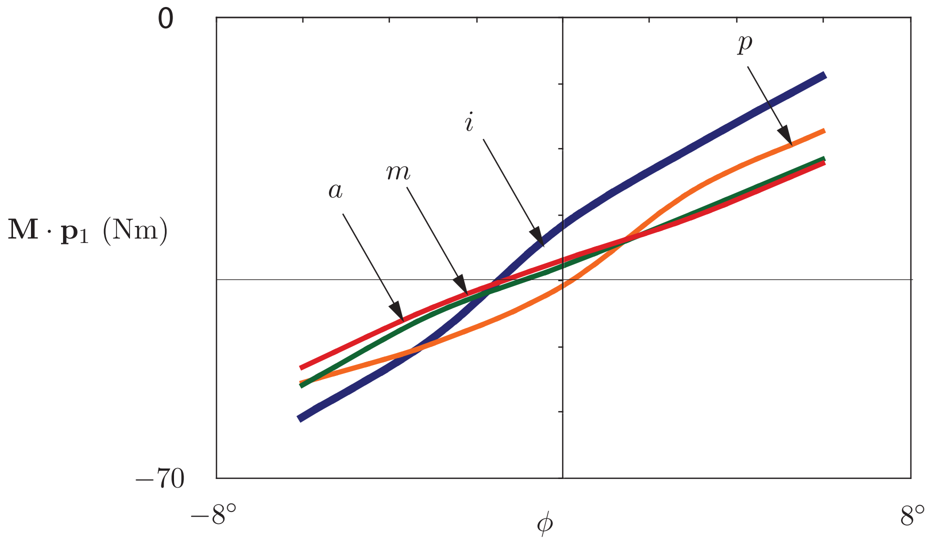

Figure 4.4: The moment component $\mathbf{M}\cdot\mathbf{p}_1$ as a function of the angle ϕ of flexion/extension for an intact motion segment and a three different positionings of a TDR. Here, and in Figs. 4.5 and 4.6, the label i stands for intact, p stands for posterior, a denotes anterior, and m denotes a centered positioning of the TDR.

Stiffness Matrices

For one of the five specimens, the following stiffness matrices were computed. The first of these matrices, K_i is for the intact specimens, while the matrices $\mathsf{K}_{p,m,a}$ correspond

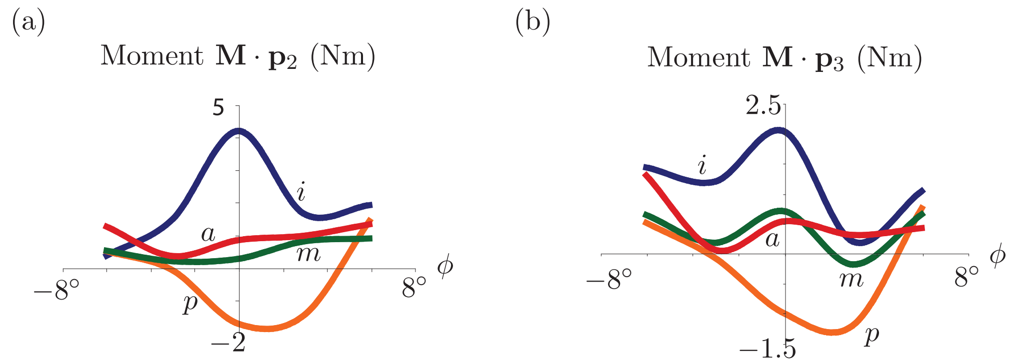

Figure 4.5: The moment components (a) $\mathbf{M}\cdot\mathbf{p}_2$ in the lateral direction and (b) $\mathbf{M}\cdot\mathbf{p}_3$ in the axial direction as a function of the angle ϕ of flexion/extension for an intact motion segment and a three different positionings of a TDR. The label i stands for intact, p stands for posterior, a denotes anterior, and m denotes a centered positioning of the TDR.

to the respective posterior, middle and anterior placements of the TDR:

$$\mathsf{K}_i = \begin{bmatrix} 80307 & 155477 & 29398 & -65.43 & -1102 & 1892.3 \\ 34377 & 382690 & 91836 & -113.8 & -1779 & 1585.5 \\ 8882.4 & -17381 & 3227.2 & -400 & -537.3 & 1630.6 \\ 599.5 & 1439.9 & 399.83 & -11.52 & -11.97 & 13.468 \\ 7544.9 & 16460 & 2832 & -50.85 & 174.02 & -276.9 \\ -105 & 7014.3 & 1468.5 & 7.9949 & -154.8 & 307.05 \end{bmatrix},$$

$$\mathsf{K}_p = \begin{bmatrix} 40731 & 31188 & 9704.2 & -315.8 & 35.422 & -393.2 \\ 59442 & 248555 & 52209 & -1510 & 1225 & -752.3 \\ 24364 & -46694 & 11257 & -977.4 & -1116 & 4754.9 \\ -74.46 & 560.93 & 66.933 & -1.935 & 8.0895 & -38.99 \\ -552.3 & -1369 & -53.01 & 107.87 & -81.85 & -454.9 \\ -5468 & -3523 & -973 & 97.05 & -23.56 & -234.9 \end{bmatrix},$$

$$\mathsf{K}_m = \begin{bmatrix} 36784 & 1954.5 & -8646 & 672.07 & 689.97 & -1651 \\ 39612 & 127890 & 62070 & -2068 & 4910.3 & -8295 \\ 4175.6 & 15301 & -6291 & 922.22 & -1258 & 2181.2 \\ 162.18 & 120.06 & 196.37 & -12.96 & 1.6026 & -12.87 \\ 6924.9 & 4106.4 & -623.5 & 107.96 & 49.332 & -147.8 \\ -2413 & 3323.1 & 547.01 & 28.409 & -153.3 & 227.34 \end{bmatrix},$$

$$\mathsf{K}_a = \begin{bmatrix} 18016 & 18719 & -8076 & 800.31 & -164.2 & -506 \\ -39459 & 186498 & 23518 & 1019.8 & -60.67 & -2705 \\ 22129 & -9158 & 1813.8 & -312.5 & 235.24 & 767.71 \\ 218.16 & 63.657 & 124.48 & -8.551 & -3.891 & 1.0397 \\ 4050.3 & 2576.9 & -1038 & 86.583 & -20.16 & -23.57 \\ -461.4 & -2808 & 574.83 & -70.38 & -8.937 & 103.03 \end{bmatrix}. \tag{4.9}$$

It is interesting to note that some of the diagonal stiffness elements are negative. In further contrast to the stiffness matrices reported in the literature, the matrices presented above are not symmetric. Concerning units, the displacements and rotations used to measure these matrices had units of meters and radians, respectively. Likewise, the forces and moments were computed using unit of Newtons and Newton meters. As a result, the stiffnesses have distinct units, for example, K_{11} has units of Newtons/meter, K_{16} and K_{61} have units of Newtons, and K_{45} has units of Newton meters.

Residual Forces and Moments and Negative Stiffnesses

The experimental set-up resulted in substantial moments of extension calculated about the center of the intact disc in the neutral position (see Fig. 4.4). This moment was calculated using the identity $\mathbf{M} = \mathbf{M}_{\mathrm{m}} + \boldsymbol{\pi} \times \mathbf{F}_{\mathrm{m}}$ where $\boldsymbol{\pi}$ is the position vector of the center of mass of the intact disc relative to the load cell and $\mathbf{F}_{\mathrm{m}}$ and $\mathbf{M}_{\mathrm{m}}$ are the force and moment measurements from the load cell. Furthermore, torsional and lateral bending moments were present during flexion and extension (see Fig. 4.5). Since the stiffness coefficients are calculated from the force and displacement vectors relative to the neutral posture, it is useful to display these results. It should be noticed from these figures that residual values of the moment $\mathbf{M}$ are present even when the angle $\phi = 0°$, and the slopes of these graphs are consistent with some of the negative values for individual stiffnesses that were found. In many cases, the motion segment had a more rigid response in the neutral posture than in the rotated postures, especially once the device was inserted. This can be explained by the high elastic modulus of the device which resists axial loads, but low coefficient of friction between the UHMWPE and the chrome-moly upon bending.

For each specimen, the aggregate stiffness ratio, S, between the instrumented and intact motion segment was calculated for the three device positions. The value of S is dimensionless and can be thought of as a fractional change from the intact disc. For instance, if the value of S is 0.5, the device caused the motion segment to respond 50%

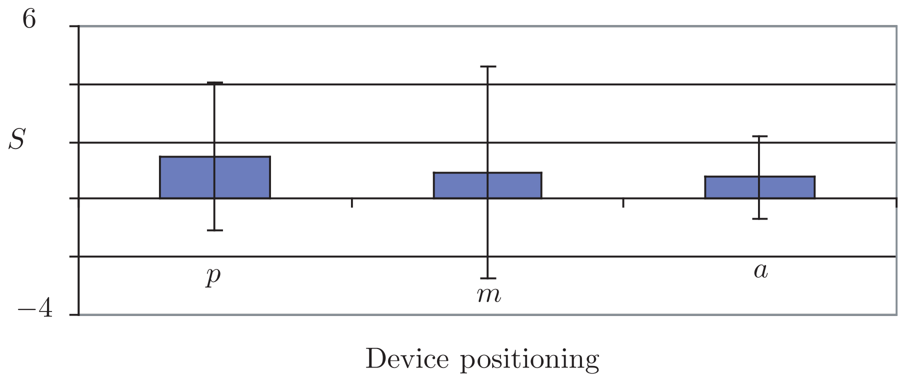

Figure 4.6: The values of the aggregate stiffness ratio S for the posterior (p), centered (m), and anterior (a) positionings of the TDR.

more rigidly than the intact disc on average over the six degrees-of-freedom. It was found that the average S of the five specimens that were tested was not significantly different ($P \leq 0.5$) for any of the device positions (Fig. 4.6), but there was a trend of increasing stiffness as the device was moved posteriorly.

4.4 Discussion

The objective of this paper was twofold. First, a new method of calculating the stiffness matrix that provides accurate calculations for large, more physiologic angles of rotation was described. This method is one of the only two possible formulations of this matrix which is valid for finite rotations.The second formulation, which would, in principle, feature screw theory and be based on the developments of Howard et al. [66] and Žefran and Kumar [142], remains to be fully developed. The principal difference in the computation of the stiffness matrix for the finite rotation case compared to the classical counterpart is the need to use the values of the angles θ, ϕ, and ψ, when computing the moment components.

As a second objective, the stiffness matrix was used to compare the changes in kinetics induced by a TDR. Although several research efforts aimed at characterizing the kinematical changes induced by a TDR have appeared (see, e.g., [117, 118]), this paper has presented the the first kinetic comparison of a TDR to an intact disc. Three placements of the TDR were also considered in this comparison. In an attempt to distill the tremendous amount of data into a possibly clinically relevant metric, an aggregate stiffness ratio S was introduced. This ratio compares two matrices (in this case, instrumented versus intact) and distills the result into a single metric. Preliminary results of the S ratio calculations (cf. Fig. 4.6) display its ability as an efficient tool to compare and contrast devices as it is easy to interpret both clinically and statistically. There is a clear need for such a metric, apparent by the stream of technology that has poured into the orthopaedic spine community in the past decade. While further work is needed to prove its efficacy, it has the potential for quantifying device stiffness in vitro.

The stiffness matrix introduced in this paper is unique from those presented in earlier works since, as described above, the kinematic values are measured relative to a neutral or pre-loaded state. Additionally, previous studies in spinal kinetics have typically calculated each stiffness coefficient independently or assumed their value from symmetry. By combining six displacement vectors and their respective force vectors the stiffness matrix presented in this paper represents a comprehensive stiffness measure in all six degrees-of-freedom. Present work by the authors involves performing an extensive error analysis which aims to quantify how accurately one can determine the stiffness matrix K given the limitations inherent in the measurements of rotations, displacements, forces, and moments.

Chapter 5

Conclusions

Back pain is one of the most prevalent and costly conditions in the United States. It affects approximately 90% of Americans at some point in their lives and is ranked 3rd among the most expensive disorders after heart disease and cancer. While numerous surgical treatments have been developed to treat chronic back pain over the past century, no intervention has been shown to greatly improve patients' outcome. Largely responsible is the complex structure and motion of each individual functional spine unit (FSU) confounded by the intricate interactions among all 24 FSUs over the length of the entire spine. These structural complexities present obstacles to engineering a mechanical means of replacing painful degenerated discs, and underline the need for more robust and accurate metrics for measuring spinal kinematics and kinetics. The biomechanical tests and theoretical work presented here reveal weaknesses in current testing protocols and provide methods to improve two metrics used to evaluate spinal prostheses. This work, combined with the suggestions for future studies as described below, is intended to enhance the kinematic assessment of total disc replacements (TDRs) and create future designs that more accurately replicate the six-dimensional movement of the spine.

The study presented in Chapter 2 investigated the response of TDRs to physiological-levels of shear loading in the L5-S1 motion segment. In addition, it compared three different sagittal locations of the Prodisc-L device to determine how surgical placement alters loading in the facet joints. The results of this study revealed that the Prodisc-L increased facet forces except when it was placed 2mm posteriorly. With the artificial disc in place, patterns of facet loading were observed to be opposite of the intact disc during sagittal plane movement regardless of its fore-aft position. That is, after TDR, facet forces tended to increase with flexion. This rather unexpected result was explained by a mechanical rationale that pointed to potential inadequacies of the ball-and-socket-design of first generation TDRs.

Chapter 2 focused on first generation, FDA-approved, artificial disc devices, namely: the Prodisc-L and its competitor, the Charité Artificial Disc. Both of these devices have a ball-and-socket design based on the success of their predecessors, the artificial knee and the artificial hip. Unfortunately, the artificial disc has not experienced similarly favorable clinical results. This is most likely because the shallow ball-and-socket design of the artificial disc does not take into account the unique three-joint system characteristic of the intervertebral joint, neglecting the left and right facets. Chapter 2's experimental evidence suggests that this design's ability to resist shear is a function of overlap between the inferior and superior surfaces. This overlap however, is a function of rotation. As the motion segment rotates into flexion less overlap is available to resist anterior shear leaving the facets with a greater burden to prevent subluxation. This mechanical rationale combined with the knowledge that shear forces within the lumbaosacral spine are significant, indicates a need for a better design. Evidence to this effect are reports of poor clinical results using TDRs in the lumbosacral spine that have surfaced in recent years [111, 124, 125].

Pure-moment loading is the gold-standard form of in vitro biomechanical testing despite the fact that it greatly simplifies physiologic loading conditions. In vivo, the spine experiences complex loading patterns along and about all three anatomical axes. One of the forces not represented in pure-moment testing is shear, an integral loading modality in lifting, pulling, and pushing tasks, all of which have been faulted as responsible for low back pain in occupational studies [57]. Shear is especially important when testing devices intended for the low back where lordosis combined with the weight of the upper torso creates large anterior-directed forces in the upright standing position. Neglecting shear, or any important physiologic loading modalities, can be detrimental when moving from the bench-top to clinical trials. This was demonstrated in 2007 when Impliant, a spinal device company, was forced to suspend the pivotal IDE trial of their Total Posterior Arthroplasty Device (TOPS (^{TM})) after excessive shear caused a device related failure [69]. If thorough pre-clinical in vitro biomechanical testing (which included shear) had been performed this unfortunate event may have been prevented.

The results of Chapter 2 demonstrate that under loading conditions which include shear, TDRs behave significantly different than the intact spine, subjecting the facets to higher-than-normal stress levels. This additional stress could lead to arthritic and painful facets, negating any positive benefits that the implant might have. In addition, the work in Chapter 2 emphasizes the importance of including shear loads when performing biomechanical tests especially for devices intended for the lumbar region of the spine.

Chapter 2 was mainly limited by its inability to provide statistically significant data as many of the results were based on trends. With a sample size of 6, statistical significance was only achieved in the most extremely flexed posture of 6 degrees. A post hoc power analysis indicated that an additional 11 specimens (totaling $n = 17$) would be necessary to demonstrate intact and TDR facet pressures are significantly different throughout rotation in flexion. Despite this limitation the resultant increase in facet pressure post-TDR in conjunction with the described flexion-subluxation hypothesis provide a sound argument for redesigning current lumbar TDRs.

Chapter 3 dissected the helical axis of motion (HAM), one of the most common kinematic measurements used in spine research, to determine whether it is sensitive enough to describe changes in motion patterns before and after surgical manipulation. Numerous studies have used the HAM as a comparative tool between instrumented and intact motion segments despite the fact that the algorithms used to calculate HAM parameters are highly error-prone. Typically, standard deviations among a given sample size are reported but the errors inherent in the calculations themselves are rarely discussed. These errors can be comparable to the measured parameters and therefore should not be overlooked.

The study in Chapter 3 is the first to compare the accuracy and reliability of the two most popular HAM algorithms used in spine biomechanics and a third algorithm frequently used in spacecraft dynamics. These algorithms convert data collected from 3D motion-tracking cameras into the parameters necessary to fully describe the HAM, which include: the angle of rotation about the axis, its directional vector, and a vector describing its location based on the intersection with a plane of interest. The results of Chapter 3 revealed the most popular method used in spine biomechanics, denoted the 'direct' method, is the least accurate method for calculating the angle and directional vector, but was actually more accurate when calculating HAM's point of intercept. This seemingly conflicting result can be explained by the error-minimizing techniques within the other two methods ('SVD' and 'triad') which are useful for the angle and axis calculations, but propagate error in the more complicated calculation for determining the HAM location. The logic behind this is detailed in Chapter 3, but the point to emphasize here is that no one method was the optimum choice for calculating all three HAM parameters.

Based on the comparison in Chapter 3, a hybrid method was developed that combined the best of the three algorithms to calculate HAM parameters. In addition, experimental techniques that increase the accuracy of motion camera data were recommended. The accuracy acquired through the use of these experimental suggestions combined with the hybrid algorithm were compared to variation in HAM parameters between the intact and TDR-implanted motion segments to determine if HAM is sensitive enough to be used as a kinematic metric. The results showed HAM's resolution is sufficient to delineate differences between experimental cases, validating its extension as a comparative tool for analyzing TDRs. This conclusion is important because HAM is a powerful and visually-descriptive tool for describing rigid body motion. Clinically this is significant because it communicates changes in motion without requiring an extensive background in rigid body dynamics especially when graphically laid over anatomical pictures, thus providing a robust and accurate means of describing complex motion to surgeons and physicians.

Chapter 3 revealed the most popular algorithm for calculating two of HAM's three parameters is significantly inaccurate and unreliable, suggesting many of the previous studies using this direct method should be read with careful consideration. All of the papers reviewed for this purpose of this study failed to include any form of error analysis. Many of these also failed to mention that error within the motion tracking data can propagate through the non-linear calculations involved in determining the HAM. This suggests that the conclusions deduced in these studies may be based on misrepresentations of the actual motion. Chapter 3 exposes these misrepresentations and emphasizes the importance of reporting error when performing data analysis on motion tracking data. By surfacing this information we intend to advance future research to a higher standard of accuracy and reporting.

Recommendations for future research following Chapter 3's investigation include performing an in vitro study that utilizes the suggested experimental and analytical methods to determine changes before and after TDR. The case study in Chapter 3 was based on previously collected data tracking three markers, making it impossible to use the hybrid method which requires at least 4 markers. Applying the practices developed in Chapter 3 would likely strength the argument for making the hybrid method a standard in the field of biomechanics.

In Chapter 4 the stiffness matrix was revisited after left untouched for over a decade based on some fairly debilitating limitations and complex mechanical testing needs. By borrowing techniques from advanced rigid-body dynamics, these limitations were overcome and a stiffness matrix capable of comparing motion segments before and after implantation of

TDRs was developed. In addition, a method of distilling the 6x6 stiffness matrix into a single scalar was presented, providing a more communicative and statistically manageable method for comparing different motion segments. An example of its utility was demonstrated in a comparison of instrumented versus non-instrumented motion segments.

The stiffness matrix developed in Chapter 4 exploits a novel system of describing basis vectors for the moving body (upper verterbral body in this case) that allows for finite rotations and non-conservative forces that are typical of the intervertebral disc. This basis is called the dual-Euler basis, developed by one of my thesis advisors, Professor Oliver O'Reilly [100]. Prior to this method, the stiffness matrix was calculated from a fixed frame of reference, limiting rotations to less than 2 degrees above which errors in moment calculations became too large to consider. In other words, prior to the work described in this dissertation, the stiffness matrix was incapable of analyzing about 80% of the lumbar's range of motion. The dual Euler basis eliminates this restriction by providing a basis that follows the moving vertebrae, turning the stiffness matrix into a kinetic metric that covers the spine's full range of motion. Previous studies of the stiffness matrix also relied on the assumption that spinal motion is symmetric about the coronal plane. Chapter 4 demonstrated this assumption is invalid and overlooks coupled motion patterns characteristic of the spine. By accommodating complex motion, the dual Euler basis provides a comprehensive description of the spine's 6-dimensional motion.

To date, researchers applied a load along a particular direction and measured the resultant displacements (or vice versa) to calculate each of the 36 matrix entries. This long and tedious process provided unilateral data, but was not representative of true spinal motion. The method described in Chapter 4, on the other hand, allows for the application of physiological loads and measurement of the spine's exact response. This data is directly converted into the 6x6 stiffness matrix using elementary matrix multiplication. The result is a robust and comprehensive matrix that can easily be implemented into spine simulations and other mathematical models requiring structural properties of the intervertebral joint.

Chapter 4 describes the first use of the stiffness matrix in a comparative study of motion segments before and after TDR. Unlike most kinematic methods of characterization, the stiffness matrix and its scalar counterpart include information on altered forces and moments, painting a more vivid picture of the TDR's effect on the spine. Future research is needed to validate and expand the use of the stiffness matrix for this particular application. Specifically, a large sample size of repetitive motion would help demonstrate the stiffness matrix as a reliable tool. In addition, a simple computer simulation that inputs loads and uses the stiffness matrix to predict spinal motion would confirm its utility. An error analysis on the calculation of the stiffness matrix paralleled this work and can be found in Nur Adila Faruk Senan's Master's Thesis [41].

In conclusion, this dissertation has made substantial and novel contributions to our knowledge of spinal rigid body dynamics. Through this work, current FDA-approved devices were found inappropriate for lower lumbar regions of the spine. In addition, a thorough analysis of two metrics for measuring spinal kinematics and kinetics verified their efficacy for comparing and contrasting various spinal constructs. Although the future of back pain treatment is currently focused on biological solutions, the technologies behind such advancements are still in their infancy. Meanwhile, hundreds of thousands of patients are undergoing surgical treatment to alleviate their pain today. The experimental and theoretical work described herein provides the tools and guidelines necessary to expand our current understanding of spinal motion. This, in turn, will guide the design of future surgical instrumentation and second generation TDRs that will hopefully result in a mechanical solution for back pain.

Bibliography

[1] M. Adams, W. Hutton, and J. Stott. The resistance to flexion of the lumbar intervertebral joint. *Spine*, 5:245–253, 1980.

[2] M. A. Adams and W. C. Hutton. The effect of posture on the role of the apophysial joints in resisting intervertebral compressive forces. *J Bone Joint Surg Br*, 62(3):358–62, 1980.

[3] D. S. Adams. M. A., McNally and P. Dolan. 'stress' distributions inside intervertebral discs: The effects of age and degeneration. *J. Bone Joint Surg. Am.*, 78(6):965–972, 1996.

[4] F.H. Albee. Transplantation of a portion of the tibia into the spine for potts disease. *JAMA*, 57:855–858, 1911.

[5] T. P. Andriacchi, P. L. Briant, S. L. Bevill, and S. Koo. Rotational changes at the knee after acl injury cause cartilage thinning. *Clin Orthop Relat Res*, 442:39–44, 2006.

[6] T. P. Andriacchi and C. O. Dyrby. Interactions between kinematics and loading during walking for the normal and acl deficient knee. *J Biomech*, 38(2):293–8, 2005.

[7] T. P. Andriacchi, A. Mundermann, R. L. Smith, E. J. Alexander, C. O. Dyrby, and S. Koo. A framework for the in vivo pathomechanics of osteoarthritis at the knee. *Ann Biomed Eng*, 32(3):447–57, 2004.

[8] S. S. Antman. Solution to Problem 71–24: "Angular velocity and moment potential for a rigid body," by J. G. Simmonds. *SIAM Review*, 14:649–652, 1972.

[9] K. S. Arun, T. S. Huang, and S. D. Blostein. Least-square fitting of two 3D point sets. *IEEE Transactions on Pattern Analysis and Machine Intelligence*, 9(5):698–700, 1987.

[10] R. Bertagnoli and S. Kumar. Indications for full prosthetic disc arthroplasty: A correlation of clinical outcomes against a variety of indications. *Eur. Spine J.*, 11(Supplement No. 2):S131–S136, 2002.

[11] H.J. Bigelow. Insensibility during surgical operations produced by inhalation. *Boston Med Surg J*, 35:309–317, 1846.

[12] S. Blumenthal, P.C. McAfee, R.D. Guyer, S.H. Hochschuler, F.H. Geisler, R.T. Holt, R. Garcia Jr, J.J. Regan, and D.D. Ohnmeiss. A Prospective, Randomized, Multicenter Food and Drug Administration Investigational Device Exemptions Study of Lumbar Total Disc Replacement With the CHARITE (TM) Artificial Disc Versus Lumbar Fusion: Part I: Evaluation of Clinical Outcomes. *Spine*, 30(14):1565, 2005.

[13] C.M. Bono and C.K. Lee. Critical Analysis of Trends in Fusion for Degenerative Disc Disease Over the Past 20 Years: Influence of Technique on Fusion Rate and Clinical Outcome. *Spine*, 29(4):455, 2004.

[14] Gina Brockenbrough. Ide trial shows similar pain reduction with intervertebral disc vs. fusion at 1 year. *OrthoSupersite*, 1st on the web(Spine), August 20, 2008.

[15] S. Çagli, R.H. Chamberlain, V.K.H. Sonntag, and N.R. Crawford. The Biomechanical Effects of Cervical Multilevel Oblique Corpectomy. *Spine*, 29(13):1420, 2004.

[16] J. Casey and V. C. Lam. On the relative angular velocity tensor. *ASME J. Mech. Transm.*, 108:399–400, 1986.

[17] C. T. Chen, N. Burton-Wurster, C. Borden, K. Hueffer, S. E. Bloom, and G. Lust. Chondrocyte necrosis and apoptosis in impact damaged articular cartilage. *J Orthop Res*, 19(4):703–11, 2001.

[18] T.Y. Chen, N.R. Crawford, V.K.H. Sonntag, and C.A. Dickman. Biomechanical effects of progressive anterior cervical decompression. *Spine*, 26(1):6–13, 2001.

[19] J. Cholewicki and S. M. McGill. Mechanical stability of the in vivo lumbar spine: Implications for injury and chronic low back pain. *Clin. Biomech.*, 11(1):1–15, 1996.

[20] R. Chou, J. Baisden, E.J. Carragee, D.K. Resnick, W.O. Shaffer, and J.D. Loeser. Surgery for Low Back Pain: A Review of the Evidence for an American Pain Society Clinical Practice Guideline. *Spine*, 34(10):1094–1109, 2009.

[21] N. R. Crawford, G. T. Yamaguchi, and C. A. Dickman. Methods for determining spinal flexion/extension, lateral bending, and axial rotation from marker coordinate data: Analysis and refinement. *Human Movement Science*, 15(1):55–78, 1996.

[22] N.R. Crawford, N. Duggal, R.H. Chamberlain, S. Chan Park, V.K.H. Sonntag, and

C.A. Dickman. Unilateral cervical facet dislocation: injury mechanism and biomechanical consequences. *Spine*, 27(17):1858, 2002.

[23] PA Cripton, TR Oxland, and QA Zhu. Use of helical axis of motion and facet joint load information in the evaluation of non-fusion spinal implants: Concept and preliminary results. *Roundtables in Spine Surgery*, 1:22–30, 2005.

[24] J. J. Crisco III and M. M. Panjabi. Euler stability of the human ligamentous lumber spine. Part i: Theory. *Clin. Biomech.*, 7(1):19–26, 1992.

[25] J. J. Crisco III, M. M. Panjabi, I. Yamamoto, and T. R. Oxland. Euler stability of the human ligamentous lumber spine. Part i: Experiment. *Clin. Biomech.*, 7(1):27–32, 1992.

[26] B. W. Cunningham, A. E. Dmitriev, N. Hu, and P. C. McAfee. General principles of total disc replacement arthroplasty: Seventeen cases in a nonhuman primate model. *Spine*, 28:S118–S124, 2004.

[27] B. W. Cunningham, Y. Kotani, P. S. McNulty, A. Cappuccino, and P. C. McAfee. The effect of spinal destabilization and instrumentation on lumbar intradiscal pressure: An in vitro biomechanical analysis. *Spine*, 22(22):2655–2663, 2003.

[28] T. David. Long-term results of one-level lumbar arthroplasty: Minimum 10-year follow-up of the CHARITE artificial disc in 106 patients. *Spine*, 32(6):661–6, 2007.

[29] M. de Kleuver, F. C. Oner, and W. C. Jacobs. Total disc replacement for chronic low back pain: Background and a systematic review of the literature. *Eur. Spine J.*, 12(2):108–116, 2003.

[30] A. de Lange, R. Huiskes, and J. M. G. Kauer. Measurement errors in Roentgen-stereophotogrammetric joint-motion analysis. *Journal of Biomechanics*, 23(3):259–269, 1990.

[31] R.A. Deyo, D.T. Gray, MPA William Kreuter, S. Mirza, and B.I. Martin. United States Trends in Lumbar Fusion Surgery for Degenerative Conditions. *Spine*, 30(12):1441–1445, 2005.

[32] RA Deyo, A. Nachemson, and SK Mirza. Spinal Fusion Surgery: the case for restraint. *New England Journal of Medicine*, 350:722–726, 2004.

[33] P. Dolan, M. Earley, and M. A. Adams. Bending and compressive stresses acting on the lumbar spine during lifting activities. *J Biomech*, 27(10):1237–48, 1994.

[34] A. P. Dooris, V. K. Goel, N. M. Grosland, L. G. Gilbertson, and D. G. Wilder. Load-sharing between anterior and posterior elements in a lumbar motion segment implanted with an artificial disc. *Spine*, 26(6):E122–9, 2001.

[35] L. Dorst. First order error propagation of the Procrustes method for 3D attitude estimation. *IEEE T. Pattern Anal.*, 27(2):221–229, 2005.

[36] R. B. Dunlop, M. A. Adams, and W. C. Hutton. Disc space narrowing and the lumbar facet joints. *J Bone Joint Surg Br*, 66(5):706–10, 1984.

[37] G. Duval-Beaupere and G. Robain. Visualization on full spine radiographs of the anatomical connections of the centers of the segmental body mass supported by each vertebra and measured in vivo. *Int. Orthop.*, 11:261–269, 1987.

[38] D. W. Eggert, A. Lorusso, and R. B. Fisher. Estimating 3-D rigid body transformations: A comparison of four major algorithms. *Machine Vision and Applications*, 9(5–6):272–290, 1997.

[39] J.S. Erulkar, J.N. Grauer, et al. Flexibility analysis of posterolateral fusions in a New Zealand white rabbit model. *Spine*, 26(10):1125–1130, 2001.

[40] D.R. Eyre. *The biology of the intervertebral disc*, chapter Collagens of the disc, pages 171–188. CRC Press, 1988.

[41] N. A. Faruk Senan. How Accurately can the Stiffness Matrix of a Vertebral Unit be Measured? Master's thesis, University of California at Berkeley, 2008.

[42] B. Fassio and JF Ginestie. Prothése discale en silicone. Etude experimentale et premiéres observations cliniques. *Nouv Press Med*, 21:207, 1978.

[43] U. Fernstrm. Arthroplasty with intercorporal endoprothesis in herniated disc and in painful disc. *Acta Chir Scand Suppl*, 357:154–159, 1966.

[44] The International Society for the Advancement of Spine Surgery. 9^{th} annual global symposium on motion preservation technology. In *A Time for Brilliance*, 2009.

[45] J.W. Frymoyer, E. Hanley, J. Howe, D. Kuhlmann, and R. Matteri. Disc excision and spine fusion in the management of lumbar disc disease: a minimum ten-year followup. *Spine*, 3(1):1, 1978.

[46] F. Galbusera, C. M. Bellini, T. Zweig, S. Ferguson, M. T. Raimondi, C. Lamartina,

M. Brayda-Bruno, and M. Fornari. Design concepts in lumbar total disc arthroplasty. *Eur Spine J*, 17:1635–1650, Dec 2008.

[47] S. Gallagher, W. S. Marras, A. S. Litsky, and D. Burr. Torso flexion loads and the fatigue failure of human lumbosacral motion segments. *Spine*, 30(20):2265–73, 2005.

[48] R. Ganz, M. Leunig, K. Leunig-Ganz, and W. H. Harris. The etiology of osteoarthritis of the hip: an integrated mechanical concept. *Clin Orthop Relat Res*, 466(2):264–72, 2008.

[49] M. Gardner-Morse, I. A. Stokes, and J. P. Laible. Role of muscles in lumbar spine stability in maximum extension efforts. *J. Orthop. Res.*, 13:802–808, Sep 1995.

[50] M. G. Gardner-Morse, J. P. Laible, and I. A. Stokes. Incorporation of spinal flexibility measurements into finite element analysis. *J Biomech Eng*, 112:481–483, Nov 1990.

[51] M. G. Gardner-Morse and I. A. Stokes. Physiological axial compressive preloads increase motion segment stiffness, linearity and hysteresis in all six degrees of freedom for small displacements about the neutral posture. *J. Orthop. Res.*, 21(3):547–552, 2003.

[52] M. G. Gardner-Morse and I. A. F. Stokes. Structural behavior of the human lumbar spinal motion segments. *J. Biomech.*, 37(2):205–212, 2004.

[53] V. K. Goel, J. N. Grauer, TCh Patel, A. Biyani, K. Sairyo, S. Vishnubhotla, A. Matyas, I. Cowgill, M. Shaw, R. Long, D. Dick, M. M. Panjabi, and H. Serhan. Effects of charite artificial disc on the implanted and adjacent spinal segments mechanics using a hybrid testing protocol. *Spine*, 30(24):2755–64, 2005.

[54] V. K. Goel and J. M. Winterbottom. Experimental investigation of three-dimensional spine kinetics. *Spine*, 16(8):1000–1002, 1991.

[55] V.K. Goel, M.M. Panjabi, A.G. Patwardhan, A.P. Dooris, and H. Serhan. Test protocols for evaluation of spinal implants. *The Journal of Bone and Joint Surgery*, 88:103–109, 2006.

[56] Young H.H. Gohrmerly R.K., Love J.G. The "combined operation" in low back and sciatic pain. Follow-up study. *In: Collected papers. Mayo Clinic and Mayo Foundation. Rochester, Minnesota: Mayo Foundation*, 20:475–579, 1947.

[57] K. P. Granata, W. S. Marras, and K. G. Davis. Variation in spinal load and trunk dynamics during repeated lifting exertions. *Clin Biomech (Bristol, Avon)*, 14(6):367–75, 1999.

[58] S. Grassmann, T.R. Oxland, U. Gerich, and L.P. Nolte. Constrained testing conditions affect the axial rotation response of lumbar functional spinal units. *Spine*, 23(10):1155, 1998.

[59] S. L. Griffith, A. P. Shelokov, K. Bttner-Janz, J. P. LeMaire, and W. S. Zeegers. A multicenter retrospective study of the clinical results of the LINK SB Charit intervertebral prosthesis. The initial European experience. *Spine*, 19:1842–1849, 1994.

[60] F. Guilak. The deformation behavior and viscoelastic properties of chondrocytes in articular cartilage. *Biorheology*, 37(1-2):27–44, 2000.

[61] R. D. Guyer, P. C. McAfee, R. J. Banco, F. D. Bitan, A. Cappuccino, F. H. Geisler, S. H. Hochschuler, R. T. Holt, L. G. Jenis, M. E. Majd, J. J. Regan, S. G. Troman-

hauser, D. C. Wong, and S. L. Blumenthal. Prospective, randomized, multicenter Food and Drug Administration investigational device exemption study of lumbar total disc replacement with the CHARITE artificial disc versus lumbar fusion: five-year follow-up. *Spine J*, 9:374–386, May 2009.

[62] R.A. Hibbs. An operation for progressive spinal deformities: a preliminary report of three cases from the service of the orthopaedic hospital. *NY Med J*, 93:1013–1016, 1911.

[63] B. K. P. Horn. Closed-form solution of absolute orientation using unit quaternions. *Journal of the Optical Society of America, Series A*, 4(4):629–642, 1987.

[64] B. K. P. Horn, H. M. Hilden, and S. Negahdaripour. Closed-form solution of absolute orientation using orthonormal matrices. *Journal of the Optical Society of America, Series A*, 5(7):1127–1135, 1988.

[65] TS Hou, KY Tu, YK Xu, ZB Li, AH Cai, and HC Wang. Lumbar intervertebral disc prosthesis. An experimental study. *Chinese medical journal*, 104(5):381, 1991.

[66] S. Howard, M. Žefran, and V. Kumar. On the 6×6 Cartesian stiffness matrix for three-dimensional motions. *Mech. Mach. Theory*, 33(4):389–408, 1998.

[67] S. J. Howarth, A. E. Allison, S. G. Grenier, J. Cholewicki, and S. M. McGill. On the implications of interpreting the stability index: A spine example. *J. Biomech.*, 37(8):1147–1154, 2004.

[68] R. C. Huang, F. P. Girardi, Jr. Cammisa, F. P., and T. M. Wright. The implications

of constraint in lumbar total disc replacement. *J Spinal Disord Tech*, 16(4):412–7, 2003.

[69] Impliant Company News. Impliant Restarts European Clinical Activities for Patented TOPS ^{TM}Spine System. http://www.impliant.com/default.asp?PageID=12&ItemID=22, July 2008.

[70] Depuy Spine Acromed Inc. News and Press Releases: DePuy AcroMed, Inc., Completes Acquisition of Link Spine Group, Inc. . http://www.depuyspine.com/about/about.press.060303.asp, June 2003.

[71] J. Keat. Analysis of Least-Squares Attitude Determination Routine DOAOP. CSC Report CSC/TM–77/6034, February 1977.

[72] TS Keller, DM Spengler, and TH Hansson. Mechanical behavior of the human lumbar spine. I. Creep analysis during static compressive loading. *Journal of Orthopaedic Research*, 5(4), 1987.

[73] A. Kettler, F. Marin, G. Sattelmayer, M. Mohr, H. Mannel, L. D
"urselen, L. Claes, and HJ Wilke. Finite helical axes of motion are a useful tool to describe the three-dimensional in vitro kinematics of the intact, injured and stabilised spine. *European Spine Journal*, 13(6):553–559, 2004.

[74] GL Kinzel, AS Hall Jr, and BM Hillberry. Measurement of the total motion between two body segments. I. Analytical development. *Journal of Biomechanics*, 5(1):93, 1972.

[75] M. N. Kumar, A. Baklanov, and D. Chopin. Correlation between sagittal plane changes and adjacent segment degeneration following lumbar spine fusion. *Eur Spine J*, 10(4):314–9, 2001.

[76] M. N. Kumar, F. Jacquot, and H. Hall. Long-term follow-up of functional outcomes and radiographic changes at adjacent levels following lumbar spine fusion for degenerative disc disease. *Eur Spine J*, 10(4):309–13, 2001.

[77] C.K. Lee et al. Accelerated degeneration of the segment adjacent to a lumbar fusion. *Spine*, 13(3):375–377, 1988.

[78] C.K. Lee and N.A. Langrana. A review of spinal fusion for degenerative disc disease: need for alternative treatment approach of disc arthroplasty? *The Spine Journal*, 4(6S):173–176, 2004.

[79] T. R. Lehmann, K. F. Spratt, J. E. Tozzi, J. N. Weinstein, S. J. Reinarz, G. Y. el Khoury, and H. Colby. Long-term follow-up of lower lumbar fusion patients. *Spine*, 12:97–104, Mar 1987.

[80] J. P. Lemaire, H. Carrier, H. Sariali el, W. Skalli, and F. Lavaste. Clinical and radiological outcomes with the Charité artificial disc: a 10-year minimum follow-up. *J Spinal Disord Tech*, 18(4):353–9, 2005.

[81] H. D. Link. History, design and biomechanics of the LINK SB Charité artificial disc. *Eur Spine J*, 11 Suppl 2:S98–S105, Oct 2002.

[82] M. Lorenz, A. Patwardhan, and Jr. Vanderby, R. Load-bearing characteristics of

lumbar facets in normal and surgically altered spinal segments. *Spine*, 8(2):122–30, 1983.

[83] M. Mansour, S. Spiering, C. Lee, H. Dathe, A. K. Kalscheuer, D. Kubein-Meesenburg, and H. Nägerl. Evidence for iha migration during axial rotation of a lumbar spine segment by using a novel high-resolution 6d kinematic tracking system. *J. Biomech.*, 37(9):583–592, 2004.

[84] A. Maroudas. *Nutrition and metabolism of the intervertebral disc*, chapter Nutrition and metabolism of the intervertebral disc, pages 1–37. CRC Press, 1988.

[85] B.I. Martin, R.A. Deyo, S.K. Mirza, J.A. Turner, B.A. Comstock, W. Hollingworth, and S.D. Sullivan. Expenditures and health status among adults with back and neck problems. *JAMA*, 299(6):656, 2008.

[86] T. G. Mayer, G. Kondraske, S. B. Beals, and R. J. Gatchel. Spinal range of motion. Accuracy and sources of error with inclinometric measurement. *Spine*, 22(17):1976–1984, 1997.

[87] P. C. McAfee, B. Cunningham, G. Holsapple, K. Adams, S. Blumenthal, R. D. Guyer, A. Dmietriev, J. H. Maxwell, J. J. Regan, and J. Isaza. A prospective, randomized, multicenter Food and Drug Administration investigational device exemption study of lumbar total disc replacement with the CHARITE artificial disc versus lumbar fusion: part II: evaluation of radiographic outcomes and correlation of surgical technique accuracy with clinical outcomes. *Spine*, 30:1576–1583, 2005.

[88] C.A. McDevitt. *The biology of the intervertebral disc*, chapter Proteoglycans of the intervertebral disc, pages 151–171. CRC Press, 1988.

[89] S. McGill and R. Norman. Effects of an anatomically detailed erector spinae model on L4/L5 disc compression and shear. *J. Biomech.*, 20(6):591–600, 1987.

[90] S. M. McGill, Seguim J., and G. Bennett. Passive stiffness of the lumbar torso about the flexion-extension, lateral bend and axial twist axes: The effect of belt wearing and breath holding. *Spine*, 19(6):696–704, 1994.

[91] S.M. McGill. Loads on the lumbar spine and associated tissues. *Biomechanics of the Spine: Clinical and Surgical Prospective*, page 65, 1990.

[92] K. McGlashen, J. Miller, A. Schultz, and G. Andersson. Load displacement behavior of the human lumbo-sacral joint. *J. Orthop. Res.*, 5(4):488–496, 1987.

[93] DS McNally and MA Adams. Internal intervertebral disc mechanics as revealed by stress profilometry. *Spine*, 17(1):66–73, 1992.

[94] M. Mimura, MM Panjabi, TR Oxland, JJ Crisco, I. Yamamoto, and A. Vasavada. Disc degeneration affects the multidirectional flexibility of the lumbar spine. *Spine*, 19(12):1371, 1994.

[95] J.H. Moe. Historical Aspects of Scoliosis. *Moe's textbook of scoliosis and other spinal deformities*, page 1, 1987.

[96] M. Moumene and F. H. Geisler. Comparison of biomechanical function at ideal and

varied surgical placement for two lumbar artificial disc implant designs: mobile-core versus fixed-core. *Spine*, 32:1840–1851, Aug 2007.

[97] A. Nachemson. Lumbar intradiscal pressure. Experimental studies on post-mortem material. *Acta orthopaedica Scandinavica. Supplementum*, 43:1, 1960.

[98] C. A. Niosi and T. R. Oxland. Degenerative mechanics of the lumbar spine. *The Spine Journal*, 4(6):S202–S208, 2004.

[99] P. O'Leary, M. Nicolakis, M. A. Lorenz, L. I. Voronov, M. R. Zindrick, A. Ghanayem, R. M. Havey, G. Carandang, M. Sartori, I. N. Gaitanis, S. Fronczak, and A. G. Patwardhan. Response of charite total disc replacement under physiologic loads: prosthesis component motion patterns. *Spine J*, 5(6):590–9, 2005.

[100] O. M. O'Reilly. The dual Euler basis: Constraints, potentials, and Lagrange's equations in rigid body dynamics. *J. Appl. Mech.*, 74(2):256–258, 2007.

[101] O. M. O'Reilly. *Intermediate Engineering Dynamics: A Unified Approach to Newton-Euler and Lagrangian Mechanics*. Cambridge University Press, New York, 2008.

[102] O. M. O'Reilly, M. F. Metzger, J. M. Buckley, D. A. Moody, and J. C. Lotz. On the stiffness matrix of the intervertebral joint: Application to total disk replacement. *ASME Journal of Biomechanical Engineering*, 131:081007–1–081007–9, 2009.

[103] O. M. O'Reilly and A. R. Srinivasa. On potential energies and constraints in the dynamics of rigid bodies and particles. *Math. Probl. Eng.*, 8(3):169–180, 2002.

[104] R. D. Orr, P. D. Postak, M. Rosca, and A. S. Greenwald. The current state of cervical and lumbar spinal disc arthroplasty. *J Bone Joint Surg Am*, 89 Suppl 3:70–5, 2007.

[105] TR Oxland, MM Panjabi, and RM Lin. Axes of motion of thoracolumbar burst fractures. *Journal of spinal disorders*, 7(2):130–138, 1994.

[106] M. Panjabi and AA White 3rd. A mathematical approach for three-dimensional analysis of the mechanics of the spine. *Journal of biomechanics*, 4(3):203, 1971.

[107] M. M. Panjabi. Centers and angles of rotation of body joints: A study of errors and optimization. *J. Biomech.*, 12(12):911–920, 1979.

[108] M. M. Panjabi. The stabilizing system of the spine. Part II. Neutral zone and instability hypothesis. *J. Spinal Disorders*, 5(4):390–397, 1992.

[109] M. M. Panjabi, R. A. Brand Jr., and A. A. White. Three-dimensional flexibility and stiffness properties of the human thoracic spine. *J. Biomech.*, 9(4):185–192, 1976.

[110] M. M. Panjabi, T. Oxland, I. Yamamoto, and J. Crisco. Mechanical behavior of the human lumbar and lumbosacral spine shown by three-dimensional load displacement curves. *J. Bone Joint Surg. Am.*, 76(3):413–424, 1994.

[111] C. K. Park, K. S. Ryu, and W. H. Jee. Degenerative changes of discs and facet joints in lumbar total disc replacement using prodisc ii: minimum two-year follow-up. *Spine*, 33(16):1755–61, 2008.

[112] V. V. Patel, C. Andrews, B. B. Pradhan, H. W. Bae, L. E. Kanim, M. A. Kropf, and R. B. Delamarter. Computed tomography assessment of the accuracy of in vivo

placement of artificial discs in the lumbar spine including radiographic and clinical consequences. *Spine*, 31(8):948–53, 2006.

[113] A. G. Patwardhan, R. M. Havey, K. P. Meade, B. Lee, and B. Dunlap. A follower load increases the load-carrying capacity of the lumbar spine in compression. *Spine*, 24(10):1003–1009, 1999.

[114] I. M. Punt, V. M. Visser, L. W. van Rhijn, S. M. Kurtz, J. Antonis, G. W. H. Schurink, and A. van Ooij. Complications and reoperations of the SB Charité lumbar disc prosthesis: Experience in 75 patients. *Eur. Spine J.*, 17(1):36–43, 2008.

[115] M. Putzier, J.F. Funk, S.V. Schneider, C. Gross, S.W. Tohtz, C. Khodadadyan-Klostermann, C. Perka, and F. Kandziora. Charite total disc replacementclinical and radiographical results after an average follow-up of 17 years. *European Spine Journal*, 15(2):183–195, 2006.

[116] W.C. Röntgen. Über eine neue Art von Strahlen (vorläufige Mittheilung). *Sber Phys-Med Ges Würzb*, 137:132–41, 1895.

[117] M. A. Rousseau, D. S. Bradford, R. Bertagnoli, S. S. Hu, and J. C. Lotz. Disc arthroplasty design influences intervertebral kinematics and facet forces. *Spine J*, 6(3):258–66, 2006.

[118] M. A. Rousseau, D. S. Bradford, T. M. Hadi, K. L. Pedersen, and J. C. Lotz. The instant axis of rotation influences facet forces at L5/S1 during flexion/extension and lateral bending. *Eur Spine J.*, 15(3):299–307, 2006.

[119] M. Sharma, N. A. Langrana, and J. Rodriguez. Role of ligaments and facets in lumbar spinal stability. *Spine*, 20(8):887–900, 1995.

[120] Y. Shono, K. Kaneda, K. Abumi, P. C. McAfee, and B. W. Cunningham. Stability of posterior spinal instrumentation and its effects on adjacent motion segments in the lumbosacral spine. *Spine*, 23:1550–1558, 1998.

[121] M. D. Shuster. A comment on fast three-axis attitude determination. *J. Astronaut. Sci.*, 31(4):579–584, 1983.

[122] M. D. Shuster. A survey of attitude representations. *J. Astronaut. Sci.*, 41(4):439–517, 1993.

[123] M. D. Shuster and S. D. Oh. Three-axis attitude determination from vector observations. *J. Guidance*, 4(1):70–77, 1981.

[124] C. J. Siepe, A. Korge, F. Grochulla, C. Mehren, and H. M. Mayer. Analysis of post-operative pain patterns following total lumbar disc replacement: results from fluoroscopically guided spine infiltrations. *Eur Spine J*, 17(1):44–56, 2008.

[125] C. J. Siepe, H. M. Mayer, M. Heinz-Leisenheimer, and A. Korge. Total lumbar disc replacement: different results for different levels. *Spine*, 32(7):782–90, 2007.

[126] J. G. Simmonds. Moment potentials. *Am. J. Phys.*, 52(9):851–852, 1984.

[127] AG Smith. Account of a case in which portions of three dorsal vertebrae were removed for the relief of paralysis from fracture, with partial success. *N Am Med Surg J*, 8:94–97, 1829.

[128] I. Söderkvist and P.-Å. Wedin. Determining the movements of the skeleton using well-configured markers. *Journal of Biomechanics*, 26(12):1473–1477, 1993.

[129] I. Söderkvist and P.-Å. Wedin. On condition numbers and algorithms for determining a rigid body movement. *BIT Numerical Mathematics*, 346(3):424–436, 1994.

[130] C. W. Spoor. Explanation, verification and application of helical-axis error propagation formulae. *Human Movement Science*, 3(1–2):95–117, 1984.

[131] C. W. Spoor and F. E. Veldpaus. Rigid body motion calculated from spatial coordinates of markers. *J. Biomech.*, 13(4):391–393, 1980.

[132] I. A. Stokes and M. Gardner-Morse. Three-dimensional simulation of Harrington distraction instrumentation for surgical correction of scoliosis. *Spine*, 18:2457–2464, Dec 1993.

[133] I. A. Stokes and M. Gardner-Morse. Lumbar spine maximum efforts and muscle recruitment patterns predicted by a model with multijoint muscles and joints with stiffness. *J Biomech*, 28:173–186, Feb 1995.

[134] I. A. Stokes and M. Gardner-Morse. Lumbar spinal muscle activation synergies predicted by multi-criteria cost function. *J Biomech*, 34:733–740, Jun 2001.

[135] I. A. Stokes, M. G. Gardner-Morse, D. Churchill, and J. P. Laible. Measurement of a spinal motion segment stiffness matrix. *J. Biomech.*, 35(4):517–521, 2002.

[136] I. A. F. Stokes and J. C. Iatridis. *Basic Orthopaedic Biomechanics and Mechano-*

Biology, chapter Biomechanics of the Spine, pages 529–561. Lippincott Williams & Wilkins, Philadelphia, third edition, 2005. Edited by V. C. Mow and R. Huiskes.

[137] M. Szpalski, R. Gunzburg, and M. Mayer. Spine arthroplasty: a historical review. *European Spine Journal*, 11:65–84, 2002.

[138] Y. Tochigi, M. J. Rudert, T. O. McKinley, D. R. Pedersen, and T. D. Brown. Correlation of dynamic cartilage contact stress aberrations with severity of instability in ankle incongruity. *J Orthop Res*, 2008. 1554-527X (Electronic) Journal article.

[139] U.S. Food and Drug Administration. PRODISC-L Total Disc Replacement - P050010. http://www.fda.gov/MedicalDevices/ProductsandMedicalProcedures/, August 2006.

[140] A. van Ooij, F. C. Oner, and A. J. Verbout. Complications of artificial disc replacement: a report of 27 patients with the sb charite disc. *J Spinal Disord Tech*, 16(4):369–83, 2003.

[141] F. E. Veldpaus, H. J. Woltring, and L. J. M. G. Dortmans. A least-squares algorithm for the equiform transformation from spatial marker co-ordinated. *Journal of Biomechanics*, 21(1):45–54, 1988.

[142] M. Žefran and V. Kumar. A geometrical approach to the study of the Cartesian stiffness matrix. *J. Mech. Design*, 124(1):30–38, 2002.

[143] M.W. Walker, L. Shao, and R.A. Volz. Estimating 3-D location parameters using dual number quaternions. *Computer Vision and Image Understanding*, 54(3):358–367, 1991.

[144] A. A. White III and M. M. Panjabi. *Clinical Biomechanics of the Spine*. Lippincott Williams & Wilkins, Philadelphia, second edition, 1990.

[145] D. C. Wilson, C. A. Niosi, Q. A. Zhu, T. R. Oxland, and D. R. Wilson. Accuracy and repeatability of a new method for measuring facet loads in the lumbar spine. *J Biomech*, 39(2):348–53, 2006.

[146] H. J. Woltring, R. Huiskes, A. de Lange, and F. E. Veldpaus. Finite centroid and helical axis estimation from noisy landmark measurements in the study of human joint kinematics. *Journal of Biomechanics*, 18(5):379–389, 1985.

[147] K. H. Yang and A. I. King. Mechanism of facet load transmission as a hypothesis for low-back pain. *Spine*, 9(6):557–65, 1984.

[148] V. R. Yingling and S. M. McGill. Anterior shear of spinal motion segments. kinematics, kinetics, and resultant injuries observed in a porcine model. *Spine*, 24(18):1882–9, 1999.

[149] Q. Zhu, C.R. Larson, S.G. Sjovold, D.M. Rosler, O. Keynan, D.R. Wilson, P.A. Cripton, and T.R. Oxland. Biomechanical Evaluation of the Total Facet Arthroplasty System (TM): 3-Dimensional Kinematics. *Spine*, 32(1):55, 2007.

[150] J. Zigler, R. Delamarter, J. M. Spivak, R. J. Linovitz, G. O. Danielson, T. T. Haider, F. Cammisa, J. Zuchermann, R. Balderston, S. Kitchel, K. Foley, R. Watkins, D. Bradford, J. Yue, H. Yuan, H. Herkowitz, D. Geiger, J. Bendo, T. Peppers, B. Sachs, F. Girardi, M. Kropf, and J. Goldstein. Results of the prospective, randomized, multicenter Food and Drug Administration investigational device exemption study of the

ProDisc-L total disc replacement versus circumferential fusion for the treatment of 1-level degenerative disc disease. *Spine*, 32:1155–1162, May 2007.

[151] J. E. Zigler. Lumbar spine arthroplasty using the ProDisc II. *Spine J*, 4:260S–267S, 2004.

[152] M. R. Zindrick, M. N. Tzermiadianos, L. I. Voronov, M. Lorenz, and A. Hadjipavlou. An evidence-based medicine approach in determining factors that may affect outcome in lumbar total disc replacement. *Spine*, 33(11):1262–9, 2008.

Appendix A

Chapter 2 Appendix

A.1 Standard Operating Procedure

Specimen ID ________

STANDARD OPERATING PROCEDURE

STUDY OF PRODISC DEVICE POSITIONING
M. Metzger, 02/11/07

OPERATOR ____________________________ DATE ____________________

INTRUMENTATION (circle): Intact / 3mm Anterior / Neutral / 3mm Posterior

I. IMPLANTATION OF DEVICE:

SURGEON: __________________________

Assessment of L5/S1 disc quality: ____
Assessment of vertebrae quality: ____

NOTES:

Specimen ID ________

PROCEDURE CHECKLIST:

A. Check MTS and Load Cell and Get all systems ready for execution:

____ Turn on both computers making sure the AMTI signaling box, MTS controller box, Eagle Hub, and Tekscan box are all on

____ Turn on MTS pumps (reset-low-high)

____ Start up software for each system

- ____ MTS: load test Star file ('melodie_prodisc.tcc in Prodisc folder on MTS computer)
- ____ Labview: Open master code ('prodisc_master.vi)
- ____ Motion Analysis: Click on EvaRT4.0 on desktop and load project file (prodisc_ma.prj)
- ____ Tekscan: Click on ResearchFoot and open patient (Melodie)

____ Check Load Cell using 5kg weight

____ Calibrate Motion Analysis with Block and Wand

- ____ Focal length ~25 for each camera
- ____ Save project file (prodisc_maSPECIMEN_NUMBER.prj)

B. Wet Work

1. TEKSCAN FACET SENSOR PLACEMENT

____ Insert and suture/glue Tekscan sensors into each facet capsule

____ Sensor used (6900 #___)

- ____ left facet is sutured with sensel: _1/2/3/4_
- ____ right facet sutured with sensel: _1/2/3/4_

Comments:

____ Insert Markers (11 total):

- ____ L5 (3 – L-shape)
- ____ S1 (3 – L-shape)
- ____ Pot (1 – on anterior right corner)
- ____ Center of Left facet (2 – stick)
- ____ Center of Right facet (2 – stick)

2. MARKER PLACEMENT

Facet Markers:

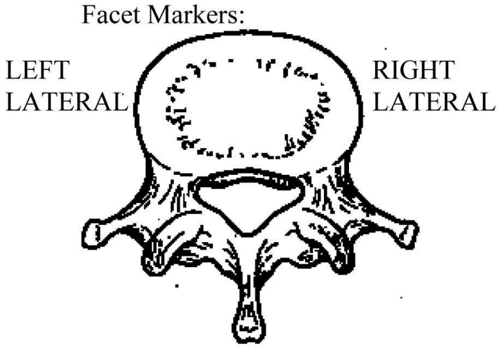

L5 and S1 Markers:

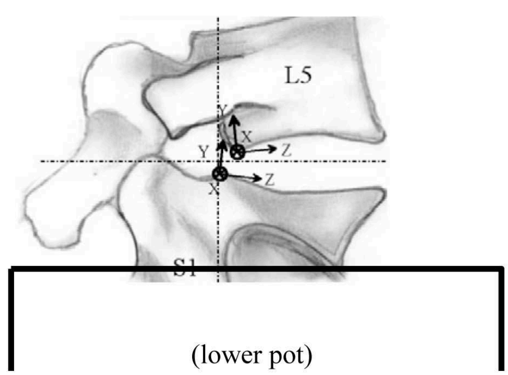

Specimen ID ________

D. Specimen Mounting and Preparation for loading:

____ Place specimen onto Jig (right side facing cameras)
____ Apply Molybdenum metal lubricant to plate surfaces and lower MTS so plates are barely touching
____ Zero forces and moments on Labview
____ Create Motion Analysis template for specimen
____ load Tekscan calibration file:____

1. First Run: Neutral

****Make sure preconditioning is set for 3/5 cycles for implanted/intact**

____ Preload to –50 N.
____ Zero MTS LVDT displacement
____ Zero Load on MTS
____ Start Testware (prodisc_melodie.000) and name XXXX(I/N/P/A)(F/E)0 file
____ Pull up scope (pink button) in Teststar and change axes: displacement: 0 to -30mm, Force: 0 to -700N
____ Motion Analysis set to record: Make sure all 3 cameras see all 11 markers
____ Check: (tracked ASCII, OK to overwrite, enable trigger-mode, Duration:1000s)

Comments on Mechanical Testing:

Data Saving and Back-up:

____ MA data file saved
____ Tekscan data file saved
____ Labview data file saved

****Change MTS file so that there is NO preconditioning**

2. Next test:____________________

____ Preload to –50 N.
____ Zero MTS LVDT displacement
____ Zero Load on MTS
____

Comments on Mechanical Testing:

Data Saving and Back-up:

____ MA data file saved
____ Tekscan data file saved
____ Labview data file saved

3. Next test:____________________

____ Preload to –50 N.
____ Zero MTS LVDT displacement
____ Zero Load on MTS

Comments on Mechanical Testing:

Data Saving and Back-up:

____ MA data file saved
____ Tekscan data file saved

Specimen ID ________

____ Labview data file saved

4. Next test:____________________

____ Preload to –50 N.
____ Zero MTS LVDT displacement
____ Zero Load on MTS
____

Comments on Mechanical Testing:

Data Saving and Back-up:

____ MA data file saved
____ Tekscan data file saved
____ Labview data file saved

5. Next test:____________________

____ Preload to –50 N.
____ Zero MTS LVDT displacement
____ Zero Load on MTS
____

Comments on Mechanical Testing:

Data Saving and Back-up:

____ MA data file saved
____ Tekscan data file saved
____ Labview data file saved

6. Next test:____________________

____ Preload to –50 N.
____ Zero MTS LVDT displacement
____ Zero Load on MTS
____

Comments on Mechanical Testing:

Data Saving and Back-up:

____ MA data file saved
____ Tekscan data file saved
____ Labview data file saved

7. Next test:____________________

____ Preload to –50 N.
____ Zero MTS LVDT displacement
____ Zero Load on MTS
____

Specimen ID ________

Comments on Mechanical Testing:

Data Saving and Back-up:

____ MA data file saved
____ Tekscan data file saved
____ Labview data file saved

8. Next test: ____________________

____ Preload to –50 N.
____ Zero MTS LVDT displacement
____ Zero Load on MTS
____

Comments on Mechanical Testing:

Data Saving and Back-up:

____ MA data file saved
____ Tekscan data file saved
____ Labview data file saved

9. Next test: ____________________

____ Preload to –50 N.
____ Zero MTS LVDT displacement
____ Zero Load on MTS
____

Comments on Mechanical Testing:

Data Saving and Back-up:

____ MA data file saved
____ Tekscan data file saved
____ Labview data file saved

10. Next test: ____________________

____ Preload to –50 N.
____ Zero MTS LVDT displacement
____ Zero Load on MTS
____

Comments on Mechanical Testing:

Data Saving and Back-up:

____ MA data file saved
____ Tekscan data file saved

Specimen ID ________

____ Labview data file saved

F.
____ files all transferred to laptop

G. X-rays:

____ Lateral
kVp and time:

____ A/P
kVp and time:

Appendix B

Chapter 3 Appendix

B.1 A Brief Note on the Displacement

It is common practice to determine the displacement using the equation

$$\mathbf{a} = \mathbf{Q}\mathbf{A} + \mathbf{d}.$$

However, as mentioned in Soderkvist [128], the rotation matrix and displacement computed using the SVD algorithm assume that the helical axis passes through the origin. This is almost never true in spinal kinematics where the HAM intercept is one of the main unknown variables. For this reason, we define the displacement obtained when the HAM is located at the origin as the *true* displacement,

$$\mathbf{a}^2 - \mathbf{a}^1 = \mathbf{Q}(\mathbf{A}^2 - \mathbf{A}^1) + \mathbf{d}^{\mathrm{true}}, \tag{B.1}$$

and the displacement determined via equation (3.4) as the HAM displacement $\mathbf{d}^{\mathbf{s}}$ since it is used to locate the position of the helical axis in space. (If there are more than 2 markers placed on the rigid body, then the mean of these displacement measurements, found by looking at all possible combinations of relative marker positions, should be used to determine $\mathbf{d}^{\text{true}}$.)

The difference between the two displacements is depicted in Figure B.1. Only the rotation matrix and the true displacement are invariant with respect to the origin of the coordinate system used; $\mathbf{d}^{s}$ is now.

The triad and SVD methods are designed to find the optimum $\mathbf{Q}$ and $\mathbf{d}^{\text{true}}$ instead of the best $\mathbf{Q}$ and $\mathbf{d}^{\mathbf{s}}$. We suspect that this is the reason both of these algorithms determine the axis and angle of rotation relatively accurately, but are inferior to the direct method for locating the HAM position in space.

B.2 MATLAB code

B.2.1 Hybrid Helical Axis of Motion

```
function [r,phi,disp,point_int,point_int10, point_int100]...
=hybrid(A,a,n_mark,intersect,coord_int)

%
% Description: Program calculates the rotation matrix (3x3) using a singular
%              value decomposition method (Soederkvist & Wedin 1993).
%              The displacement vector d (3x1) is then calculated using
%              the Direct method (Kinzel 1993
%               for a rigid body segment using a singular
%              value decomposition method (Soederkvist & Wedin 1993).
%
% Input:       A:   columns representing the XYZ positions of the markers in the
%                   initial/reference configuration
%              a:   columns representing the XYZ positions of the markers in the
%                   final/current configuration
%         n_mark:   number of markers. Needs to be >=4
%      intersect:   location of the screw axis where it intersects:
%                           y-z plane : intersect=1
%                           x-z plane : intersect=2
%                           x-y plane : intersect=3
```

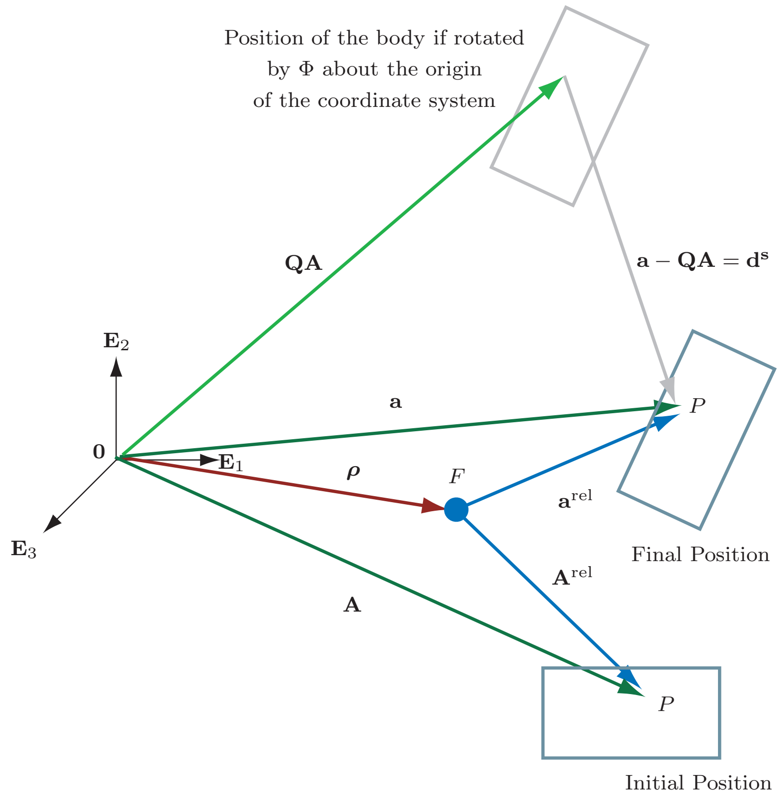

Figure B.1: Graphical representation of the absolute and relative position vectors of the point P of the rigid body before and after a pure rotation by Φ about the helical axis, $\mathbf{s}$ (located at F). The rigid body undergoes a pure rotation about the helical axis of motion from the initial to final configuration: $\mathbf{a}^{\text{rel}} = \mathbf{Q}\mathbf{A}^{\text{rel}} + \mathbf{d}^{\text{true}}(= 0)$. The vector $\boldsymbol{\rho}$ is the point of interception of the helical axis of motion with the plane of interest (in this case, the E_1-E_2 plane. The vectors $\mathbf{A}$ and $\mathbf{a}$ are the position vectors of the point P before and after the rotation is applied, as measured from the origin of the coordinate system while $\mathbf{A}^{\text{rel}}$ and $\mathbf{a}^{\text{rel}}$ are the position vectors of P as measured from the center of rotation. The angle of rotation Φ is always measured relative to the helical axis of motion. However, the displacement vector $\mathbf{d}^{\mathbf{s}}$ determined using equation (3.4) depends on the origin of the coordinate system used.

```
%       coord_int:   coordinate of the intersect point corresponding to
%                            the plane of interest.
%
% Output:       r:   unit vector with direction of helical axis
%             phi:   angle of rotation in degrees (measured positive
%                    anti-clockwise)
%            disp:   displacement of the rigid body, as measured from the origin
%                    of the coordinate system
%       point_int:   point of intercept of the Helical Axis with the plane of
%                    interest at height = coord_int
%
% References:     Kinzel G.L, Hall A.S. and Hillberry M., (1972).
%                 Measurement of the total motion between two body segments
%                 1. Analytical Development
%                 Journal of Biomechanics, 5: 93-105
%
%                 Spoor and Veldpaus (1980) Rigid body motion calculated
%                 from spatial co-ordinates of markers.
%                 Journal of Biomechanics, 13: 391-393
%
%                 Soderkvist I. and Wedin P. -A., (1993). Determining the
%                 movements of the skeleton using well-configured markers.
%                 Journal of Biomechanics, 26:1473-1477
%
%
% Authors: Melodie F. Metzger and Adila (How much wood would a wood chuck chuck
%           it were Chuck Norris's wood chuck?) Faruk
%           (some Matlab code adapted from Ron Jacobs, 1993 and
%            Christoph Reinschmidt, 1994)

% Date: August, 2009

%SVD Method to Calculate the Rotation Matrix --> angle and axis of Rotation %%%

% Create 3-by-n_mark matrices consisting of the marker positions before and
% after the motion
A=reshape(A,3,n_mark);
B=reshape(a,3,n_mark);

% Algorithm 1 of Soderkvist I. and Wedin P.-A.
%%%%%%%%%%%%%%%%%%%%%%%%%%%%%%%%%
Amean=mean(A,2); Bmean=mean(B,2);
%get relative distances
for i=1:size(A,2)
```

```
        Ai(:,i)=[A(:,i)-Amean];
        Bi(:,i)=[B(:,i)-Bmean];
end
C=Bi*Ai';
[P,T,Q]=svd(C);
R=P*diag([1 1 det(P*Q')])*Q';
% Displacement determined using the method given in Kinzel, 1972
%%%%%%%%%%%%%%%%%%%%%%%%%%%%%%%%

% Calculating the HAM parameters from R using hybrid_screw.m:
[r,phi]=hybrid_screw(R);

%%Direct/Kinzel Method to Calculate the displacement --> point of intercept %%%%

% Equation 14 of Kinzel, 1972
A=[1,1,1,1;A];
B=[1,1,1,1;B];
T=B*inv(A);

disp=T(2:4,1);

% To determine the axis and angle of rotation we use equation
% (19) in Kinzel's 1972 paper
%
N = (R(2,2)-1)*(R(3,3)-1)-R(2,3)*R(3,2);
a11 = R(1,1); a12 = R(1,2); a13 = R(1,3);
a21 = R(2,1); a22 = R(2,2); a23 = R(2,3);
a31 = R(3,1); a32 = R(3,2); a33 = R(3,3);
bsx = disp(1); bsy = disp(2); bsz = disp(3);

Nreal = (R(2,2)-1)*(R(3,3)-1)-R(2,3)*R(3,2);

S=solve('ux^2+uy^2+uz^2=1', 'uy=(ux/N)*((a23*a31)-a21*(a33-1))',...
'uz=(ux/N)*((a21*a32)-a31*(a22-1))');

digits(5)
ux = subs(S.ux); ux = subs(ux);
uy = subs(S.uy); uy = subs(uy);
uz = subs(S.uz); uz = subs(uz);

rD =[ux(1);uy(1);uz(1)]; rD=single(rD);
ax = rD(1); ay = rD(2); az = rD(3);

%%%%%%%Uncomment this for the case of a single coord_int%%%%%%%%
```

```
%
% eq1 ='(a11-1)*px + a12*py + a13*pz = zk*ax - bsx';
% eq2 ='a21*px + (a22-1)*py + a23*pz = zk*ay - bsy';
% eq3 ='a31*px + a32*py + (a33-1)*pz = zk*az - bsz';
%
% %To deal with different planes of intersection:
% if intersect == 1
%     eq4= 'px=coord_int';
% end
% if intersect == 2
%     eq4= 'py=coord_int';
% end
% if intersect == 3
%     eq4= 'pz=coord_int';
% end
%
% S=solve(eq1,eq2,eq3,eq4);
% px = subs(S.px);
% py = subs(S.py);
% pz = subs(S.pz);
% K = subs(S.zk); %Scalar displacement along the HAM (not used)
%
% return
% %%%%%%%%%%%%%%%%%%%%%%%%%%%%%%%%%%%%%%%%%%%%%%%%%%%%

% To determine the displacement, K, and the intercept with a particular
% plane we use equation (26) in Kinzel's 1972 paper.
c1 = coord_int(1); c2 = coord_int(2); c3 = coord_int(3);

eq1 ='(a11-1)*px + a12*py + a13*pz = zk*ax - bsx';
eq2 ='a21*px + (a22-1)*py + a23*pz = zk*ay - bsy';
eq3 ='a31*px + a32*py + (a33-1)*pz = zk*az - bsz';


%To deal with different planes of intersection:
if intersect == 1
    eq4= {'px=c1','px=c2','px=c3'};
end
if intersect == 2
    eq4= {'py=c1','py=c2','py=c3'};
end
if intersect == 3
    eq4= {'pz=c1','pz=c2','pz=c3'};
end
```

```
px=zeros(3,1);
py=zeros(3,1);
pz=zeros(3,1);

%Solve for the point of intersect of the HAM with the plane of interest
for i=1:3
 S=solve(eq1,eq2,eq3,eq4{i});
 py(i) = subs(S.py);
 px(i) = subs(S.px);
 pz(i) = subs(S.pz);
 K(i) = subs(S.zk); %Scalar displacement along the HAM (not used)
end

point_int = [px(1,:);py(1,:);pz(1,:)];
point_int10 = [px(2,:);py(2,:);pz(2,:)];
point_int100 = [px(3,:);py(3,:);pz(3,:)];
return
```

Appendix C

Chapter 4 Appendix

C.1 Nomenclature

$\mathbf{p}_1, \mathbf{p}_2, \mathbf{p}_3$	=	right-handed orthonormal basis
$\mathbf{t}_1, \mathbf{t}_2, \mathbf{t}_3$	=	right-handed orthonormal basis
$\mathbf{t}_1^{'}, \mathbf{t}_2^{'}, \mathbf{t}_3^{'}$	=	right-handed orthonormal basis
$\mathbf{t}_1^{''}, \mathbf{t}_2^{''}, \mathbf{t}_3^{''}$	=	right-handed orthonormal basis
$\mathbf{g}_1, \mathbf{g}_2, \mathbf{g}_3$	=	Euler basis
$\mathbf{g}^1, \mathbf{g}^2, \mathbf{g}^3$	=	dual Euler basis
ψ, θ, ϕ	=	angles of axial rotation, lateral bending, and flexion-extension
$\boldsymbol{\omega}, \boldsymbol{\omega}_1, \boldsymbol{\omega}_2$	=	angular velocity vectors
$\mathbf{x}, \mathbf{x}_1, \mathbf{x}_2$	=	position vectors
$\mathbf{y} = \mathbf{x}_2 - \mathbf{x}_1$	=	displacement vector
R	=	rotation matrix
K	=	stiffness matrix of motion segment
K_{u}	=	stiffness matrix owing to conservative contributions
U	=	potential energy function
$\mathbf{F}_{\mathrm{c}_1}, \mathbf{F}_{\mathrm{c}_2}$	=	conservative forces
$\mathbf{M}_{\mathrm{c}_1}, \mathbf{M}_{\mathrm{c}_2}$	=	conservative moments
$\mathbf{F}_{\mathrm{m}}$	=	force measured by load cell
$\mathbf{M}_{\mathrm{m}}$	=	moment measured by load cell
$\mathbf{F}_{\mathrm{v}_1}, \mathbf{F}_{\mathrm{v}_2}$	=	viscoelastic forces
$\mathbf{M}_{\mathrm{v}_1}, \mathbf{M}_{\mathrm{v}_2}$	=	viscoelastic moments
$\mathbf{F}_{\mathrm{nc}_1}, \mathbf{F}_{\mathrm{nc}_2}$	=	nonconservative forces
$\mathbf{M}_{\mathrm{nc}_1}, \mathbf{M}_{\mathrm{nc}_2}$	=	nonconservative moments
F, F_0	=	generalized force vectors
d	=	generalized displacement vector
k	=	norm of the stiffness matrix
S	=	Aggregate stiffness ratio

C.2 Background on Rotations, Euler Angles and the dual Euler basis

The rotation of interest is the relative rotation of a pair of vertebra $\mathcal{V}_1$ and $\mathcal{V}_2$. To parameterize the transformation induced by this rotation is a set of Euler angles is used. In this Appendix, relevant background on the Euler angles is presented which is based on the authorative review by Shuster [122] and supplemented by material on the dual Euler basis from [100, 101].

In what follows, it is presumed that a set of right-handed orthonormal basis vectors $\{\mathbf{p}_1, \mathbf{p}_2, \mathbf{p}_3\}$ are affixed to $\mathcal{V}_1$ and a similar set $\{\mathbf{t}_1, \mathbf{t}_2, \mathbf{t}_3\}$ are attached to $\mathcal{V}_2$ (see Fig. 4.1 and Fig. C.1). The rotation of interest can be considered as transforming $\mathbf{p}_1$ to $\mathbf{t}_1$, $\mathbf{p}_2$ to $\mathbf{t}_2$, and $\mathbf{p}_3$ to $\mathbf{t}_3$.

As may be seen from Fig. 4.2(a), the manner in which the Euler angles parametrize the rotation is easily visualized by imagining two intermediate bases $\left\{\mathbf{t}_1^{'}, \mathbf{t}_2^{'}, \mathbf{t}_3^{'}\right\}$, $\left\{\mathbf{t}_1^{''}, \mathbf{t}_2^{''}, \mathbf{t}_3^{''}\right\}$. The first angle ψ represents the rotation of $\mathbf{p}_1$ and $\mathbf{p}_2$ about $\mathbf{p}_3$ to their respective transformed values $\mathbf{t}_1^{'}$ and $\mathbf{t}_2^{'}$. Similarly, the second rotation through the angle θ about the vector $\mathbf{t}_2^{'}$ and it transforms $\mathbf{t}_3^{'}$ and $\mathbf{t}_1^{'}$ into $\mathbf{t}_3^{''}$ and $\mathbf{t}_1^{''}$, respectively. The third rotation is through the angle ϕ about the vector $\mathbf{t}_1^{''}$. This final rotation transforms $\mathbf{t}_2^{''}$ and $\mathbf{t}_3^{''}$ into $\mathbf{t}_2$ and $\mathbf{t}_3$, respectively.

One can define a proper-orthogonal matrix R to represent the transformation of $\mathbf{p}_i$ to $\mathbf{t}_i$:

$$\begin{bmatrix} \mathbf{t}_1 \\ \mathbf{t}_2 \\ \mathbf{t}_3 \end{bmatrix} = \begin{bmatrix} R_{11} & R_{21} & R_{31} \\ R_{12} & R_{22} & R_{32} \\ R_{13} & R_{23} & R_{33} \end{bmatrix} \begin{bmatrix} \mathbf{p}_1 \\ \mathbf{p}_2 \\ \mathbf{p}_3 \end{bmatrix},$$

$$\begin{bmatrix} \mathbf{p}_1 \\ \mathbf{p}_2 \\ \mathbf{p}_3 \end{bmatrix} = \begin{bmatrix} R_{11} & R_{12} & R_{13} \\ R_{21} & R_{22} & R_{23} \\ R_{31} & R_{32} & R_{33} \end{bmatrix} \begin{bmatrix} \mathbf{t}_1 \\ \mathbf{t}_2 \\ \mathbf{t}_3 \end{bmatrix}, \tag{C.1}$$

where the components of the matrix are

$$\begin{bmatrix} R_{11} & R_{12} & R_{13} \\ R_{21} & R_{22} & R_{23} \\ R_{31} & R_{32} & R_{33} \end{bmatrix} = \begin{bmatrix} \mathrm{c}(\psi) & -\mathrm{s}(\psi) & 0 \\ \mathrm{s}(\psi) & \mathrm{c}(\psi) & 0 \\ 0 & 0 & 1 \end{bmatrix} \begin{bmatrix} \mathrm{c}(\theta) & 0 & \mathrm{s}(\theta) \\ 0 & 1 & 0 \\ -\mathrm{s}(\theta) & 0 & \mathrm{c}(\theta) \end{bmatrix} \times \begin{bmatrix} 1 & 0 & 0 \\ 0 & \mathrm{c}(\phi) & -\mathrm{s}(\phi) \\ 0 & \mathrm{s}(\phi) & \mathrm{c}(\phi) \end{bmatrix}. \tag{C.2}$$

Here, the abbreviations $\mathrm{c}(x)$ for $\cos(x)$ and $\mathrm{s}(x)$ for $\sin(x)$ have been used. The three axes of rotation for the individual angles associated with the set of Euler angles are known as the Euler basis vectors. These unit vectors are denoted by $\{\mathbf{g}_1, \mathbf{g}_2, \mathbf{g}_3\}$. For the 3-2-1 set of Euler angles, Eq. (4.1) provides a definition of $\{\mathbf{g}_1, \mathbf{g}_2, \mathbf{g}_3\}$ in terms of the basis vectors $\mathbf{p}_1, \mathbf{p}_2, \mathbf{p}_3$. Alternatively, with the help of Eq. (C.1) and Eq. (C.2), one can express the Euler basis vectors in terms of the basis vectors $\{\mathbf{t}_1, \mathbf{t}_2, \mathbf{t}_3\}$.

As can be verified from Eq. (4.1), the Euler basis vectors form a basis provided $\theta \neq \pm\frac{\pi}{2}$. As a result, one restricts the second angle $\theta \in \left(-\frac{\pi}{2}, \frac{\pi}{2}\right)$ to ensure that the Euler basis vectors form a basis. The angle θ measures lateral bending and so this restriction is trivially satisfied physiologically. The other two angles are free to range from 0 to 2π.

The angular velocity vector $\boldsymbol{\omega}$ associated with the rotation has a convenient representation when the Euler basis vectors are used:

$$\boldsymbol{\omega} = \dot{\psi}\mathbf{p}_3 + \dot{\theta}\mathbf{t}_2' + \dot{\phi}\mathbf{t}_1. \tag{C.3}$$

In the sequel a set of vectors are need which can extract from $\boldsymbol{\omega}$ the angular speeds $\dot{\psi}$, $\dot{\theta}$, and $\dot{\phi}$. This set of vectors is known as the dual Euler basis vectors: $\left\{\mathbf{g}^1, \mathbf{g}^2, \mathbf{g}^3\right\}$ [100, 101].

By definition, the dual Euler basis vectors satisfy the relations

$$\boldsymbol{\omega} \cdot \mathbf{g}^1 = \dot{\psi}, \qquad \boldsymbol{\omega} \cdot \mathbf{g}^2 = \dot{\theta}, \qquad \boldsymbol{\omega} \cdot \mathbf{g}^3 = \dot{\phi}. \tag{C.4}$$

That is,

$$\begin{aligned}
&\mathbf{g}_1 \cdot \mathbf{g}^1 = 1, \quad \mathbf{g}_1 \cdot \mathbf{g}^2 = 0, \quad \mathbf{g}_1 \cdot \mathbf{g}^3 = 0, \\
&\mathbf{g}_2 \cdot \mathbf{g}^1 = 0, \quad \mathbf{g}_2 \cdot \mathbf{g}^2 = 1, \quad \mathbf{g}_2 \cdot \mathbf{g}^3 = 0, \\
&\mathbf{g}_3 \cdot \mathbf{g}^1 = 0, \quad \mathbf{g}_3 \cdot \mathbf{g}^2 = 0, \quad \mathbf{g}_3 \cdot \mathbf{g}^3 = 1.
\end{aligned} \tag{C.5}$$

Given the Euler basis vectors, one can use the nine equations Eq. (C.5) to compute expressions for the dual Euler basis vectors. After a series of straightforward manipulations, one would find that the dual Euler basis vectors have the representations

$$\begin{bmatrix} \mathbf{g}^1 \\ \mathbf{g}^2 \\ \mathbf{g}^3 \end{bmatrix} = \begin{bmatrix} \cos(\psi)\tan(\theta) & \sin(\psi)\tan(\theta) & 1 \\ -\sin(\psi) & \cos(\psi) & 0 \\ \cos(\psi)\sec(\theta) & \sin(\psi)\sec(\theta) & 0 \end{bmatrix} \begin{bmatrix} \mathbf{p}_1 \\ \mathbf{p}_2 \\ \mathbf{p}_3 \end{bmatrix}. \tag{C.6}$$

It is important to note that the vectors $\mathbf{g}^1$ and $\mathbf{g}^3$ do not have unit magnitude (cf. Fig. 4.2(b)). Expressions for the dual Euler basis vectors in terms of $\{\mathbf{t}_1, \mathbf{t}_2, \mathbf{t}_3\}$ can established using Eq. (C.2) and Eq. (C.6)

If the Euler angles are infinitesimal, then, from Eq. (C.6), it is easy to see that

$$\mathbf{g}^1 \approx \mathbf{p}_3 \approx \mathbf{t}_3, \qquad \mathbf{g}^2 \approx \mathbf{p}_2 \approx \mathbf{t}_2, \qquad \mathbf{g}^3 \approx \mathbf{p}_1 \approx \mathbf{t}_1. \tag{C.7}$$

Related results hold for the Euler basis vectors $\mathbf{g}_k$. For the spinal applications of interest, the angles of rotation are not infinitesimal and so the approximations Eq. (C.7) cannot be used.

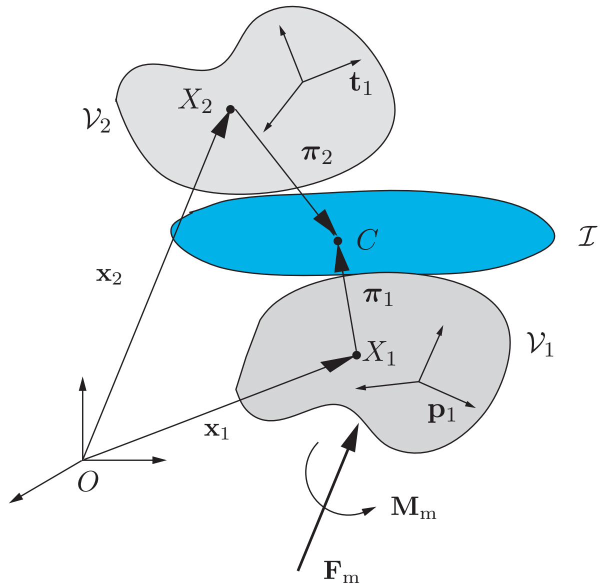

Figure C.1: A schematic drawing of an intervebral disc $\mathcal{I}$ between the vertebra $\mathcal{V}_1$ and $\mathcal{V}_2$. The point C of the disc $\mathcal{I}$ has a position vector $\mathbf{x}_1 + \boldsymbol{\pi}_1 = \mathbf{x}_2 + \boldsymbol{\pi}_2$ relative to the fixed origin O. The force $\mathbf{F}_{\mathrm{m}}$ and moment $\mathbf{M}_{\mathrm{m}}$ shown in this figure are supplied by the load cell. fig:vertunit

C.3 Derivation of the Stiffness Matrix of a Motion Segment

Consider the system consisting of two vertebra $\mathcal{V}_1$ and $\mathcal{V}_2$ located on either side of an intervertebral disc $\mathcal{I}$ shown in Fig. C.1. Of interest in this paper is the development of a mechanical model for the intervertebral disc and the facet joints. It is assumed that the disc and joints result in a force $\mathbf{F}_1$ and a moment $\mathbf{M}_1$ on $\mathcal{V}_1$ and a force $\mathbf{F}_2$ and a moment $\mathbf{M}_2$ on $\mathcal{V}_2$. The force $\mathbf{F}_1$ is assumed to act at the material point X_1 of $\mathcal{V}_1$ and the moment $\mathbf{M}_1$ is taken relative to this point (cf. Fig. 4.1). Similarly, $\mathbf{F}_2$ is assumed to act at the material point X_2 of $\mathcal{V}_2$ and the moment $\mathbf{M}_2$ is relative to X_2. In an experimental apparatus to examine the kinetics of a segment of the spine, it is standard to place a load cell directly under the vertebral body $\mathcal{V}_1$. The load cell provides two sets of measurements: the three force components and three moment components: $\mathbf{F}_{\mathrm{m}_k} = \mathbf{F}_{\mathrm{m}} \cdot \mathbf{p}_k$ and $\mathbf{M}_{\mathrm{m}_k} = \mathbf{M}_{\mathrm{m}} \cdot \mathbf{p}_k$ where $k = 1, 2, 3$.

The rotation of $\mathcal{V}_2$ relative to $\mathcal{V}_1$ can be characterized by a rotation R. The rotation is parameterized in this paper using a set of a set of 3-2-1 Euler angles: ψ, θ, and ϕ. Hence, the difference between the angular velocity vectors $\boldsymbol{\omega}_1$ and $\boldsymbol{\omega}_2$ of $\mathcal{V}_1$ and $\mathcal{V}_2$ can be expressed as

$$\boldsymbol{\omega}_2 - \boldsymbol{\omega}_1 = \dot{\psi}\mathbf{g}_1 + \dot{\theta}\mathbf{g}_2 + \dot{\phi}\mathbf{g}_3. \tag{C.8}$$

For further background on relative angular velocity vectors, the reader is referred to Casey and Lam [16]. The position vectors of the points X_1 and X_2 of the vertebrae are denoted by $\mathbf{x}_1$ and $\mathbf{x}_2$, respectively. It is standard to express these vectors in terms of the fixed basis $\{\mathbf{p}_1, \mathbf{p}_2, \mathbf{p}_3\}$, e.g., $\bar{\mathbf{x}}_1 = \sum_{k=1}^{3} x_{1_k}\mathbf{p}_k$. Furthermore, it is necessary to define the relative displacement vector of the point X_2 relative to X_1:

$$\mathbf{y} = y_1\mathbf{p}_1 + y_2\mathbf{p}_2 + y_3\mathbf{p}_3 = \mathbf{x}_2 - \mathbf{x}_1. \tag{C.9}$$

Although, it is customary to choose X_1 to be the center of mass of $\mathcal{V}_1$ and X_2 to be the center of mass of $\mathcal{V}_2$, this choice is often not convenient. Further, precise identification of the center of mass of a vertebra is non-trivial.

C.3.1 Potential Energy, Conservative Forces, and Conservative Moments

To postulate a potential energy for the motion segment and correlate its derivatives to the forces and moments on the vertebra, the methodology used in O'Reilly and Srinivasa [103] is followed. This work is compatible with, and a generalization of, works on moment potentials (e.g., [8, 126] and is entirely consistent with previous developments on moment potentials in the dynamics of rigid bodies. The crucial assumption is that the potential energy for the conservative forces and conservative moments supplied by the facets, ligaments, and intervertebral disc is

$$U = U\left(\mathbf{y}, \psi, \theta, \phi\right). \tag{C.10}$$

In this case, the relative translation and rotation of the vertebra are independent. The forces ($\mathbf{F}_{c_1}$ and $\mathbf{F}_{c_2}$) and moments ($\mathbf{M}_{c_1}$ and $\mathbf{M}_{c_2}$) supplied by the disc, facets, and ligaments to the vertebrae are conservative:

$$-\dot{U} = \mathbf{F}_{c_1} \cdot \dot{\mathbf{x}}_1 + \mathbf{F}_{c_2} \cdot \dot{\mathbf{x}}_2 + \mathbf{M}_{c_1} \cdot \boldsymbol{\omega}_1 + \mathbf{M}_{c_2} \cdot \boldsymbol{\omega}_2. \tag{C.11}$$

As

$$\dot{U} = \sum_{i=1}^{3} \frac{\partial U}{\partial y_i} \dot{y}_i + \frac{\partial U}{\partial \psi} \dot{\psi} + \frac{\partial U}{\partial \theta} \dot{\theta} + \frac{\partial U}{\partial \phi} \dot{\phi}, \tag{C.12}$$

it can be concluded that

$$\begin{aligned}
\mathbf{F}_{c_1} = -\mathbf{F}_{c_2} &= \sum_{i=1}^{3} \frac{\partial U}{\partial y_i} \mathbf{p}_i, \\
\mathbf{M}_{c_1} = -\mathbf{M}_{c_2} &= \frac{\partial U}{\partial \psi} \mathbf{g}^1 + \frac{\partial U}{\partial \theta} \mathbf{g}^2 + \frac{\partial U}{\partial \phi} \mathbf{g}^3.
\end{aligned} \tag{C.13}$$

These are the conservative forces and moments exerted by the disc on the vertebrae. The simplicity of the representations for the conservative moments $\mathbf{M}_{c_1}$ and $\mathbf{M}_{c_2}$ is directly attributable to the use of the dual Euler basis. In [103], X_1 and X_2 are chosen to be the centers of mass. A comparison of the expressions for the resultant moment relative to a center of mass and an arbitrary material point can be used to show that this restriction can be removed, and it was done in (C.13) without comment.

Assuming that U is a quadratic function of $\mathbf{y}$ and the Euler angles, a Taylor series expansion would show that

$$
\begin{aligned}
U \;=\; & \frac{1}{2}\begin{bmatrix} y_1 & y_2 & y_3 \end{bmatrix}\begin{bmatrix} a_{11} & a_{12} & a_{13} \\ a_{12} & a_{22} & a_{23} \\ a_{13} & a_{23} & a_{33} \end{bmatrix}\begin{bmatrix} y_1 \\ y_2 \\ y_3 \end{bmatrix} \\
& + \begin{bmatrix} y_1 & y_2 & y_3 \end{bmatrix}\begin{bmatrix} b_{11} & b_{12} & b_{13} \\ b_{21} & b_{22} & b_{23} \\ b_{31} & b_{32} & b_{33} \end{bmatrix}\begin{bmatrix} \psi \\ \theta \\ \phi \end{bmatrix} \\
& + \frac{1}{2}\begin{bmatrix} \psi & \theta & \phi \end{bmatrix}\begin{bmatrix} c_{11} & c_{12} & c_{13} \\ c_{12} & c_{22} & c_{23} \\ c_{13} & c_{23} & c_{33} \end{bmatrix}\begin{bmatrix} \psi \\ \theta \\ \phi \end{bmatrix} .
\end{aligned}
\tag{C.14}
$$

This function has 21 unknown coefficients. Examples featuring the identification of these coefficients occupies Section 3.2 of the present paper.

One can view the potential energy function U as a generalization of a potential energy function for a motion segment that was proposed by Panjabi et al. [109]. Their function assumed infinitesimal rotations and was intended for use in the thoracic region of the spine. The value of present formulation is that one no longer needs to impose such kinematic restrictions. The added expense, however, is that one needs to keep track of the Euler angles during measurements of forces and moments. If one restricts attention to infinitesimal rotations, then the expressions for $\mathbf{g}^i$ simplify (cf. Eq. (C.7)). If one then imposes the symmetry restrictions used in [109], then the U presented in Eq. (C.14) would reduce to the function proposed by Panjabi, Brand and White with its 12 coefficients.

To facilitate further comparison to the Panjabi, Brand and White function, one can compute, with the help of Eq. (C.13) and Eq. (C.14), the relationship between the conservative forces and conservative moments and the translational and angular displacements. These results are expressed in the compact form:

$$\mathsf{F}_{\mathrm{c}} = -\mathsf{K}_{\mathrm{u}}\mathsf{d}, \tag{C.15}$$

where the generalized force vector F_{c}, generalized displacement vector d, and stiffness matrix K_{u} are

$$\mathsf{F}_{\mathrm{c}} = \begin{bmatrix} \mathbf{F}_{\mathrm{c}_2} \cdot \mathbf{p}_1 \\ \mathbf{F}_{\mathrm{c}_2} \cdot \mathbf{p}_2 \\ \mathbf{F}_{\mathrm{c}_2} \cdot \mathbf{p}_3 \\ \mathbf{M}_{\mathrm{c}_2} \cdot \mathbf{g}_1 \\ \mathbf{M}_{\mathrm{c}_2} \cdot \mathbf{g}_2 \\ \mathbf{M}_{\mathrm{c}_2} \cdot \mathbf{g}_3 \end{bmatrix}, \quad \mathsf{d} = \begin{bmatrix} y_1 \\ y_2 \\ y_3 \\ \psi \\ \theta \\ \phi \end{bmatrix}, \quad \mathsf{K}_{\mathrm{u}} = \begin{bmatrix} a_{11} & a_{12} & a_{13} & b_{11} & b_{12} & b_{13} \\ a_{12} & a_{22} & a_{23} & b_{21} & b_{22} & b_{23} \\ a_{13} & a_{23} & a_{33} & b_{31} & b_{32} & b_{33} \\ b_{11} & b_{21} & b_{31} & c_{11} & c_{12} & c_{13} \\ b_{12} & b_{22} & b_{32} & c_{12} & c_{22} & c_{23} \\ b_{13} & b_{23} & b_{33} & c_{13} & c_{23} & c_{33} \end{bmatrix}. \tag{C.16}$$

The corresponding forces $\mathbf{F}_{\mathrm{c}_1}$ and moments $\mathbf{M}_{\mathrm{c}_1}$ on $\mathcal{V}_1$ are equal and opposite to $\mathbf{F}_{\mathrm{c}_2}$ and $\mathbf{M}_{\mathrm{c}_2}$, respectively (cf. Eq. (C.13)). It needs to be emphasized that the components of the moments in Eq. (C.15) are taken relative to the Euler basis: $\mathbf{M}_{\mathrm{c}_2} = -\mathbf{M}_{\mathrm{c}_1} = \sum_{k=1}^{3} \left(\mathbf{M}_{\mathrm{c}_2} \cdot \mathbf{g}_k\right) \mathbf{g}^k$.

C.3.2 Viscous Forces and Viscous Moments

It is well-known that the intervertebral disc is a viscoelastic body and consequently any model for the motion segment must accommodate this behavior. Here, the simplest possible viscous terms are considered and it is assumed that the viscoelastic forces ($\mathbf{F}_{\mathrm{v}_1}$ and $\mathbf{F}_{\mathrm{v}_2}$) and moments ($\mathbf{M}_{\mathrm{v}_1}$ and $\mathbf{M}_{\mathrm{v}_2}$) have the representations

$$
\begin{aligned}
\mathbf{F}_{\mathrm{v}_2} = -\mathbf{F}_{\mathrm{v}_1} &= -c_1\dot{y}_1\mathbf{p}_1 - c_2\dot{y}_2\mathbf{p}_2 - c_3\dot{y}_3\mathbf{p}_3, \\
\mathbf{M}_{\mathrm{v}_2} = -\mathbf{M}_{\mathrm{v}_1} &= -d_1\dot{\psi}\mathbf{g}^1 - d_2\dot{\theta}\mathbf{g}^2 - d_3\dot{\phi}\mathbf{g}^3.
\end{aligned} \tag{C.17}
$$

It is easy to motivate the assumption that the constants d_k and c_k are non-negative by examining the combined power $\mathcal{P}$ of these forces and moments:

$$
\begin{aligned}
\mathcal{P} &= \sum_{i=1}^{2}\left(\mathbf{F}_{\mathrm{v}_i}\cdot\dot{\mathbf{x}}_i + \mathbf{M}_{\mathrm{v}_i}\cdot\boldsymbol{\omega}_i\right) \\
&= -\left(\sum_{k=1}^{3} c_k\dot{y}_k\dot{y}_k\right) - d_1\dot{\psi}^2 - d_2\dot{\theta}^2 - d_3\dot{\phi}^2.
\end{aligned} \tag{C.18}
$$

Clearly, $\mathcal{P} \leq 0$ if $d_k \geq 0$ and $c_k \geq 0$. More complex forms of the forces and moments shown in Eq. (C.17) are eminently possible, but these suffice for the present purposes. It is also important to note that even if the d_k's had equal value, neither $\mathbf{M}_{\mathrm{v}_2}$ nor $\mathbf{M}_{\mathrm{v}_1}$ are necessarily parallel to $\boldsymbol{\omega}_2 - \boldsymbol{\omega}_1$. The viscous and conservative components of the forces and moments can be additively combined to obtain the viscoelastic forces due to the vertebral joint: e.g., $\mathbf{F}_1 = \mathbf{F}_{\mathrm{c}_1} + \mathbf{F}_{\mathrm{v}_1}$.

C.3.3 Nonconservative Contributions

In addition to the aforementioned viscoelastic contributions, the resultant forces and moments experienced by the vertebra will also include nonconservative contributions due to the contact forces in the facet joints and activation forces in the ligaments. Labelling these nonconservative contributions with the subscript nc, one has the following expressions for the resultant forces and moments:

$$\mathbf{F}_k = \mathbf{F}_{\mathrm{nc}_k} + \mathbf{F}_{\mathrm{c}_k} + \mathbf{F}_{\mathrm{v}_k}, \quad \mathbf{M}_k = \mathbf{M}_{\mathrm{nc}_k} + \mathbf{M}_{\mathrm{c}_k} + \mathbf{M}_{\mathrm{v}_k}, \tag{C.19}$$

where $k = 1, 2$. As with the previous developments $\mathbf{F}_1 = -\mathbf{F}_2$ and $\mathbf{M}_1 = -\mathbf{M}_2$.

C.3.4 The Stiffness Matrix of the Vertebral Unit

To accommodate these residual forces and moments, one performs a Taylor series expansion of the forces $\mathbf{F}_1$ and $\mathbf{F}_2$ and moments $\mathbf{M}_1$ and $\mathbf{M}_2$. Truncating this expansion at second order, ignoring the viscous contribution, leads to a representation of the form shown in Eq. (4.2) for $\mathbf{F}_2$ and $\mathbf{M}_2$

C.4 Transforming Moments

It is often desired to transform the components of a vector with respect to the basis $\{\mathbf{p}_1, \mathbf{p}_2, \mathbf{p}_3\}$ to the corresponding components with respect to the bases $\{\mathbf{g}^1, \mathbf{g}^2, \mathbf{g}^3\}$ and $\{\mathbf{t}_1, \mathbf{t}_2, \mathbf{t}_3\}$. Denoting this vector by $\mathbf{b}$, the following representations of this vector can be defined:

$$\mathbf{b} = \sum_{k=1}^{3} B_k \mathbf{p}_k = \sum_{k=1}^{3} b_k \mathbf{t}_k = \sum_{k=1}^{3} \beta_k \mathbf{g}^k. \tag{C.20}$$

Then, with the help of Eqs. (4.1), (C.1), and (C.6), one finds that

$$\begin{bmatrix} b_1 \\ b_2 \\ b_3 \end{bmatrix} = \begin{bmatrix} R_{11} & R_{21} & R_{31} \\ R_{12} & R_{22} & R_{32} \\ R_{13} & R_{23} & R_{33} \end{bmatrix} \begin{bmatrix} B_1 \\ B_2 \\ B_3 \end{bmatrix},$$

$$\begin{bmatrix} \beta_1 \\ \beta_2 \\ \beta_3 \end{bmatrix} = \begin{bmatrix} 0 & 0 & 1 \\ -\sin(\psi) & \cos(\psi) & 0 \\ \cos(\theta)\cos(\psi) & \cos(\theta)\sin(\psi) & -\sin(\theta) \end{bmatrix} \begin{bmatrix} B_1 \\ B_2 \\ B_3 \end{bmatrix}. \tag{C.21}$$

In the interests of brevity, the reader is referred to Eq. (C.2) where expressions for the components R_{ik} can be found.

Publishing Agreement

It is the policy of the University to encourage the distribution of all theses, dissertations, and manuscripts. Copies of all UCSF theses, dissertations, and manuscripts will be routed to the library via the Graduate Division. The library will make all theses, dissertations, and manuscripts accessible to the public and will preserve these to the best of their abilities, in perpetuity.

Please sign the following statement: I hereby grant permission to the Graduate Division of the University of California, San Francisco to release copies of my thesis, dissertation,or manuscript to the Campus Library to provide access and preservation, in whole or in part, in perpetuity.

12-15-09

Author Signature　　　　Date